University of Southampton

Faculty of Natural and Environmental Sciences

School of Chemistry

Modelling of electrochemical processes at microelectrodes

by

Kelly Y. S. Leonhardt

Thesis for the degree of Doctor of Philosophy

June 2012

UNIVERSITY OF SOUTHAMPTON

ABSTRACT

FACULTY OF NATURAL AND ENVIRONMENTAL SCIENCES

School of Chemistry

Doctor of Philosophy

MODELLING OF ELECTROCHEMICAL PROCESSES AT MICROELECTRODES

by Kelly Yvette Sheila Leonhardt

In this work, the finite element modelling of 2D and 3D scanning electrochemical microsopy (SECM) systems is presented. The main focus has been on the influence of tip geometry and the presence of defects on the limiting current of the SECM tip. The geometry of the electrode of particular interest is conical with conical insulation, as this is the shape of AFM-SECM probes fabricated by our coworkers. This thesis presents an extensive study of the electrochemical response of conical electrodes both in the bulk solution and close to a surface. Key equations were derived for conical electrodes and a thorough quantitative analysis of the influence of the tip geometry, be it the parameters describing it or the presence of defects, is reported. A novel equation was derived to calculate the current in the bulk at a conical electrode with conical insulation and an extensive study of possible defects was conducted to allow users to adjust the expression and obtain a more accurate estimation of the limiting current. The spatial resolution -defined as the ability of an electroactive probe to detect a conducting region of a given size- and the lateral resolution -the distance necessary to fully resolve a conducting region form an inert region- were both investigated for a range of geometries as well as for a selection of defects. This enables us to draw conclusions on the ideal tip, and how sensitive it would be to features of the substrate. A set of equations was derived to describe positive and negative feedback approach curves for cones, and steps were defined for users to determine the shape of the electrode from experimental approach curves. Simulated curves are also provided to help with the extraction of kinetics at the substrate surface from the experimental approach curves. Finally, the influence of a ring disc tip geometry was evaluated by monitoring the collection efficiency as a function of tip-substrate distance for different disc-ring separations.

Contents

List of Figures

Declaration of Authorship

I, Kelly Yvette Sheila Leonhardt, declare that the thesis entitled MODELLING OF ELECTROCHEMICAL PROCESSES AT MICROELECTRODES and the work presented in the thesis are both my own, and have been generated by me as the result of my own original research. I confirm that:

- this work was done wholly or mainly while in candidature for a research degree at this University;
- where any part of this thesis has previously been submitted for a degree or any other qualification at this University or any other institution, this has been clearly stated;
- where I have consulted the published work of others, this is always clearly attributed;
- where I have quoted from the work of others, the source is always given. With the exception of such quotations, this thesis is entirely my own work;
- I have acknowledged all main sources of help;
- where the thesis is based on work done by myself jointly with others, I have made clear exactly what was done by others and what I have contributed myself;

Signed: .....

Date: .....

List of Publications

Work described in this thesis has been published in the following publications:

Atomic Force Microscopy-Scanning Electrochemical Microscopy: Influence of Tip Geometry and Insulation Defects on Diffusion Controlled Currents at Conical Electrodes by K. Leonhardt, A. Avdic, A. Lugstein, I. Pobelov, T. Wandlowski, M. Wu, B. Gollas, and G. Denuault, Analytical Chemistry 83 (2011)

Fabrication of cone-shaped boron doped diamond and gold nanoelectrodes for AFM-SECM by A. Avdic, A. Lugstein, M.Wu, B. Gollas, I.Pobelov, T.Wandlowski, K. Leonhardt, G. Denuault, E. Bertagnolli, Nanotechnology 22 (2011)

Acknowledgements

I would like to firstly acknowledge Guy Denuault, who has been an important part of my time at university both as an undergraduate and postgraduate student, and thank him for always being approachable, encouraging, and overall a very enthusiastic supervisor. I would also like to thank my advisor Phil Bartlett.

Secondly, I wish to thank Bernhard Gollas and my collaborators on this project in Vienna, Graz and Bern and in particular Amra and Ming for making our meetings so enjoyable.

I am grateful to past and present members of the Denuault group for being very friendly and generous people to work alongside, as well as the Bartlett group for adopting me, eventually dragging me away from my three screens for tea and even a "few" pints out.

I would also like to thank all my friends and my family and in particular my dad, for his support and understanding, and my mum for always being there for me and for our daily chats about everything and nothing!!

Last but by no means least, I have to thank Ed. I simply could not have done it without you. Diolch am bopeth cariad.

Table of Symbols

Symbol	Definition
O	Oxidised species
R	Reduced species
c_i	Concentration of species i
t	Time
J_i	Flux of species i
D_i	Diffusion coefficient of species i
z_i	Charge of species i
F	Faraday's constant (96485 C mol^{-1})
R	Gas constant (8.314 J K^{-1} mol^{-1})
T	Temperature
υ	Velocity of the fluid
R_sol	Solution resistance
δ	Thickness of the diffusion layer
E_e	Potential at the electrode
E_e^0	Standard electrode potential
n	Number of electrons
k, k_f and k_b	Rate of electron transfer, forward and backward
k_0	Standard rate constant
α	Transfer coefficient
κ^{-1}	Debye length
R_g	Radius of insulation
A	Area of the electrode
c^b	Bulk concentration

Symbol	**Definition**
i_{lim}	Current at an electrode
$i_{\mathrm{lim,inf}}$	Current at an electrode in the bulk
t_{ss}	Time necessary to reach the steady state
V	Voltage applied
r_{tip}	Radius of the electrode tip
l	Tip-substrate distance
h_{recess}, h_{defect}	Height of recess, or defect
h_{tip}	Height of the protruding tip such as hemispherical and conical
a, b	Inner and outer ring radius
$H = {}^{h_{\mathrm{tip}}}/_{r_{\mathrm{tip}}}$	Aspect ratio of a protruding electrode
R_{s}	Substrate island radius
a	Blunt tip apex

Abbreviations

SECM	Scanning Electrochemical Microscopy
AFM	Atomic Force Microscopy
STM	Scanning Tunneling Microscopy
SG/TC	Substrate Generation/Tip Collection
SC/TG	Substrate Collection/Tip Generation
SEM	Scanning Electron Microscope
FIB	Focused Ion Beam
RIE	Reactive Ion Etching

General Introduction

Chapter 1

Introduction

In this thesis, electrode reactions are studied using numerical simulations. More precisely, this is done in the context of SECM experiments, where an electroactive probe is used to gather information about a surface of interest. Modelling has, from the first publications,[1;2] been an important part of SECM, necessary to fully understand the processes occurring in the experiment and more importantly extract information from the experimental data obtained. Over the past twenty-three years, simulations have become more extensive and varied, and increasingly accurate equations have been derived, such as to describe approach curves. Modelling is also often used to investigate complex probe geometries as well as complex systems. Here conical microelectrodes, used for SECM combined with atomic force microscopy (AFM), are the main focus. Microelectrodes and electrode reactions will firstly be introduced, followed by a discussion on SECM and AFM-SECM.

1.1 Electrode reactions

The simplest electrode reaction is the one electron reduction of oxidised species at the electrode at which a potential has been applied. A charged species such as $Fe(CN)_6^{3-}$ picks up an electron that has transferred across from the electrode thus forming $Fe(CN)_6^{4-}$. This reaction will occur in three main steps, as depicted in figure 1.1. The oxidised species first travels from the bulk solution towards the electrode, by mass transport. Once the oxidised species is within molecular

distance of the electrode surface, it gains an electrode and forms the reduced species. The species will then be transported away from the electrode by mass transfer.

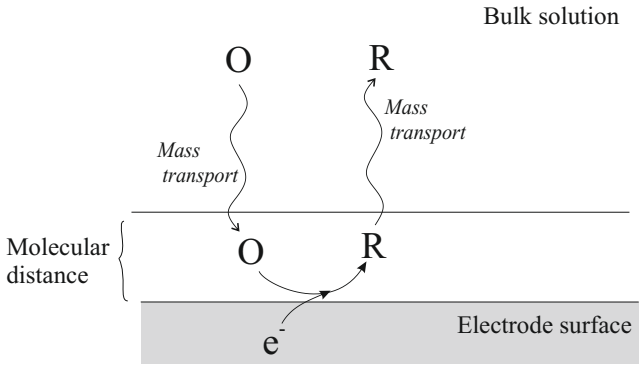

Figure 1.1: Schematic representation of the three steps of a simple one electrode redox reaction at an electrode

Most reactions at the electrode are however more complicated with chemical reactions occurring before or after the electron transfer and possibly involving the forming and breaking of bonds, adsorption, modification of the electrode surface as well as possible further reaction of the reactant.[3] It is via mass transport that the electroactive species reaches the electrode, ready for electron transfer. A very fast electron transfer will make mass transport the rate determining step whereas for slow electron transfer, the rate constant of the reaction at the electrode will be rate determining.

The change in concentration c_i as a function of time t is dictated by the change in concentration due to mass transport, as well as by the processes occurring at the electrode (electron transfer). These two forms of contribution will now be investigated further.

1.1.1 Mass transport

Mass transport -or the motion of species in solution- to an electrode, regardless of the electrodes size, obeys the Nernst-Plank equation:

$$J_{\mathrm{i}} = \underbrace{-D_{\mathrm{i}}\nabla c_{\mathrm{i}}}_{\text{Diffusion}} \underbrace{-\frac{z_{\mathrm{i}}F}{RT}D_{\mathrm{i}}c_{\mathrm{i}}\nabla\phi}_{\text{Migration}} + \underbrace{c_{\mathrm{i}}\vec{v}}_{\text{Convection}} \tag{1.1}$$

where J_{i} is the flux of species i, c_{i} is the concentration in solution of species i, D is the diffusion coefficient, v is the velocity of the fluid, z is the charge of species i and T is the temperature. This expression describes the flux of species in solution as a function of the different modes of mass transport.

1.1.1.1 Migration

Migration is the movement of charged species in solution, which results from the presence of a potential gradient in solution, existing between two electrodes. In most cases, as is assumed throughout the work presented here, a large amount of background electrolyte will be added to avoid migration of electroactive species becoming an issue, as the electrolyte present will carry the electrostatic charge through the solution. The addition of charged species, which will not be involved in the electron transfer reactions at the electrode, will minimize the contribution of migration to the mass transport of the species to react at the electrode. The presence of the supporting electrolyte will also reduce the solution resistance and therefore reduce the iR drop between two electrodes. As a result of the excess electrolyte, the thickness of the double layer will decrease, as it is inversely proportional to square root of the electrolyte concentration. Moreover, the ionic strength remains uniform in solution, regardless of additional production or consumption of charged species at the electrode.[4]

1.1.1.2 Convection

The second form of mass transport is convection, which is the movement of species in solution caused by external applied forces. These forces includes heating or stirring the solution, as well the movement of the electrode, such as when scanning a surface or rotating the electrode. This form of convection has been referred to as forced convection. For some experiments, such as the commonly used rotating disc electrode, well-behaved convection is utilized.[5;6] Forced convection can

therefore be ignored, simply by not applying any mechanical force to the system, thus further simplifying the Nernst-Plank equation.

However, one should be aware that natural convection will take place and unlike forced convection, it cannot be avoided. It may result from external influences such as unavoidable vibrations in the laboratory or from phenomena inside the solution: the reaction at the electrode will result in a change in concentration and maybe temperature near the electrode, which will lead to a density gradient, the driving force of natural convection.

1.1.1.3 Diffusion

Diffusion is the third and most important form of mass transport, not because it is the dominating one as convection can have a lot more influence on transport of species to the electrode, but because it is unavoidable and often, the only kind of mass transport occurring. The Nernst-Plank equation is reduced to a single term. Diffusion results from a concentration gradient in solution: as species are consumed at the electrode, there will be a difference between very low concentrations at the electrode to maximum concentration in the bulk. Diffusion is therefore the movement of species in solution resulting from a difference in concentration, which will lead to a homogeneous solution. On the microscopic level, species are constantly moving in solution, even in the bulk, by a random walk process.

The Nernst-Plank equation will now be reduced to a single component: the contribution of diffusion described by Fick's first law of diffusion. Fick's second law describes the change in concentration as a function of time:

$$\frac{\partial c_{\mathrm{O}}}{\partial t} = D_{\mathrm{O}} \nabla^2 c_{\mathrm{O}} \tag{1.2}$$

where c_{O} is the concentration of species O, D_{O} is the diffusion coefficient of species O and t is time. The concentration as a function of space and time can be determined from solving 1.2 analytically or numerically, with the appropriate initial and boundary conditions.

The thickness of the diffusion layer at an electrode is typically estimated using $\delta = \sqrt{\pi Dt}$, where D is the diffusion coefficient of the species in question. The distance at which the bulk solution is reached is given by $\sqrt{6Dt}$. This was derived using random walk process.[4]

1.1.2 Electron transfer

1.1.2.1 The Nernst equation

For very fast electron transfer rate constant, the reaction occurring at the electrode is controlled by the potential at the electroactive surface, described by the Nernst equation:

$$E_{\mathrm{e}} = E_{\mathrm{e}}^{0} + \frac{RT}{nF} ln \left(\frac{c_{\mathrm{O}}^{\mathrm{ede}}}{c_{\mathrm{R}}^{\mathrm{ede}}} \right) \tag{1.3}$$

E_{e} is the potential at the electrode, E_{e}^{0} is the standard redox couple potential, R is the gas constant, T is the temperature, n is the number of electrons transferred, F is Faraday's constant. Finally, $c_{\mathrm{O}}^{\mathrm{ede}}$ and $c_{\mathrm{R}}^{\mathrm{ede}}$ are the surface concentrations of species O and R respectively. Changing the potential will require an adjustment of the concentration ratio for the Nernst equation to hold. In cyclic voltammetry, the potential is cycled between two values and the current is recorded as a function of the potential. In a potential step experiment, the potential will be stepped from a value at which no reaction occurs to a potential at which the desired reaction occurs.

1.1.2.2 Kinetics of electron transfer

The potential applied to an electroactive surface will dictate the kinetics of the electron transfer at this surface. Consider a one electron redox reaction at a surface, where k_b is the rate of oxidation and k_f is the rate of reduction:

$$O + e \underset{k_{\mathrm{b}}}{\overset{k_{\mathrm{f}}}{\rightleftharpoons}} R$$

E^0 is the potential at which the reaction is at equilibrium and k_0 is the standard rate constant. The relationship between the transfer rate constants and the potential is as follows:

$$k_{\mathrm{f}} = k_0 exp\left[-\alpha \frac{F(E-E_0)}{RT}\right] \tag{1.4a}$$

$$k_{\mathrm{b}} = k_0 exp\left[(1-\alpha) \frac{F(E-E_0)}{RT}\right] \tag{1.4b}$$

The standard rate constant k_0 (in m/s) describes the kinetics of the electron transfer process at a surface: the larger the k_0 value, the more likely the process will be mass transfer limited, whereas a small k_0 indicates slow kinetics. When in equilibrium, at E_0, the forward and reverse reaction rate constants are the same and equal to the standard rate constant as described by equation 1.4. α is the transfer coefficient, which ranges from 0 to 1; this value describes the dependence of the Gibbs energy of the transition state on the electrode potential.[4] The reaction rate at the electrode can therefore be controlled by the potential applied.

The different forms of mass transfer have now been presented. Once the species of interest has reached the electrode surface, different phenomena can occur such as adsorption, e.g. a covalent bond may be formed. The product of the electron transfer at the electrode may not be stable and as such may undergo further chemical reactions before travelling away from the surface. Phase formation can occur; a phenomenon relied on to grow films on top of electrodes. Finally, more than one electron can be transferred and multiple processes can be sequential.[3]

1.2 Microelectrodes

Microelectrodes were first introduced around 1940 as electrodes used to make measurements, as opposed to inducing actual chemical changes,[7] with application such as amperometric and potentiometric sensors. It was however only in the 1980s that the use of microelectrodes really appeared and has steadily grown since then.

1.2.1 Principles of microelectrodes

1.2.1.1 Definition

There is no uniform definition of what constitutes a microelectrode, however a possible definition is:[8]

> Microelectrode is any electrode whose characteristic dimension is, under the given experimental conditions, comparable to or smaller than the diffusion layer thickness, δ.

Generally, microelectrodes are described as electrodes possessing at least one dimension small enough that its properties are a function of its size; this dimension will sometimes be referred to as the critical dimension and will typically be below 50 μm.[3]

Initially, microelectrodes were in the micrometre range. However, with the aim always to reduce the size of electrodes, in order to, for example, increase the sensitivity when scanning a surface, the dimensions of microelectrodes have now reached the nanometer scale. Concerns have been raised that the theoretical and experimental behaviour of electrodes with critical dimensions close to the double layer size would differ from the known behaviour of microelectrodes. With this in mind, Morris *et al.*[9] studied this issue by looking at cylindrical and band electrodes. The advantage of these electrodes is that the critical dimension (i.e. width or radius) could be made very small whilst keeping other dimensions, such as length, large enough not to have a current too small to measure accurately. This study confirmed previous reports of lower than expected currents for electrodes in the nm scale. These findings by Morris were also supported by later research.[10] Norton *et al.*[11] used experiments and simulations at a spherical electrode to investigate the effect of a diffusion layer in the same region as the double layer. It was revealed that the electric field affected mass transport to the electrode as well as kinetics at the electrode surface; the behaviour of the microelectrode differed from theory for $r_{\text{tip}}\kappa < 100$, where r_{tip} is the radius of the spherical electrode and κ^{-1} the Debye length, characterising the thickness of the double layer. Chen and Kucernak[12] investigated voltammetry at microelec-

trodes with and without excess electrolyte. It was found that with electrolyte, electrodes with dimensions such as effective radii as small as 1 nm behaved as expected. However without electrolyte, deviations occur for radii smaller than 20 nm. As a result of these concerns, microelectrodes are considered to have a critical dimension lower limit of 10 nm.[4]

1.2.1.2 Types of microelectrodes

There have been different microelectrode geometries and materials investigated in the last thirty years. The electroactive material -including gold, platinum, palladium, tungsten and boron doped diamond among many others- will be surrounded by an insulation sheath of radius R_g, with the exposed area acting as the electrode. Typically, the insulator is made of glass, hence the subscript 'g'. Electrode geometries range from disc electrodes, the most common, to cones, rings, hemispheres and arrays, which will be discussed in more detail in the following section. The critical dimension is dependent on the geometry of the electrode: it could be the radius or the width for example.

1.2.1.3 Characterisation of microelectrodes

Scanning electron microscope (SEM) This extremely powerful microscope will enable users to verify the shape and dimension of the electrode as well as the quality of the insulation sheath and seal.

Voltammetry In cyclic voltammetry, a potential is swept at the electrode, from a value at which no reaction occurs to one at which diffusion controlled conditions are obtained, to determine the steady state limiting current at the electrode. This is used for a simple one electron redox reaction and will enable users to verify that the current at the electrode is in the right order of magnitude or if theory exists, compare the experimental results to the theoretical expression. Features of the cyclic voltamogram would reveal information about the tip. However one must note that defects may affect the information extracted from the voltamogram, such as the radius of the electrode. A combination of methods such as using both

voltammetry and SEM would therefore be favourable for an accurate estimation of the electrode's geometrical parameters.

Scanning electrochemical microscopy (SECM) This is a method of scanning a surface using an electroactive probe. Extensive theoretical study on the subject has enabled users to be able to use experimental scans over entirely insulating and conducting surfaces to extract information about the tip geometry. This will be discussed in depth in the following section.

1.2.2 From transient to steady state

1.2.2.1 Potential step experiment

In a potential step experiment, there is initially a single oxidised species in solution. The electrode in solution will be biased at a potential for which no reaction occurs, for $t < 0$. The concentration profile is flat, as the concentration of oxidised species is uniform in solution. At $t = 0$, the potential is stepped from a value at which no reaction occurs to one where the oxidised species is reduced. The concentration of species O at the electrode will drop to 0, thus creating a concentration gradient. Diffusion will keep then a constant supply of species available to react at the electrode. If the diffusion coefficients of the oxidised and reduced species are the same, the concentration profiles will be symmetrical. Moreover, if there are no coefficients in the electrode reaction, i.e. if for every oxidised species that is reduced one reduced species is formed, the sum of the concentration of each species will be equal to the initial and bulk concentration. Different stages of diffusion can be identified from the current transient generated by the potential step experiment.

1.2.2.2 Diffusion regime of the microdisc

The diffusion regime of a microdisc electrode is divided into three parts, as depicted in figure 1.2. At short times, planar diffusion towards the electrode is observed. Edge effects have not yet gained importance and the microelectrode behaves as though it is a macroelectrode. Plotting the current against $t^{-1/2}$

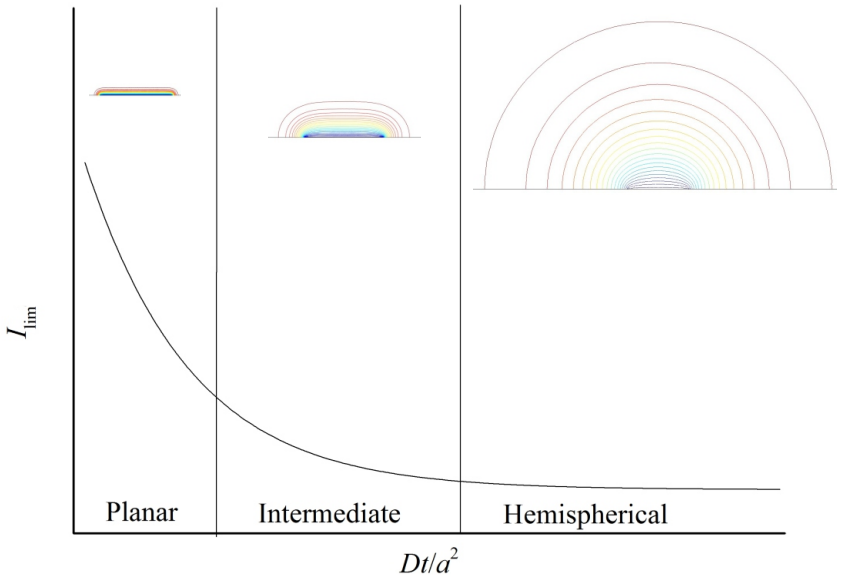

Figure 1.2: The dimensionless current I_{lim} at the electrode as a function of dimensionless time (where t is time, D is the diffusion coefficient and a is the electrode radius) with the three stages of the diffusion regime indicated and illustrated with concentration profiles at a disc electrode. In blue is zero concentration, at the electrode whereas the red represents the bulk concentration.

would confirm planar diffusion with a slope of $-1/2$ being observed, as given by the Cottrell equation, see equation 1.5:

$$i = \frac{nFAD^{1/2}c^{\text{b}}}{\pi^{1/2}t^{1/2}} \tag{1.5}$$

for n the number of electrons, F Faraday's constant, A the area of the electrode, D the diffusion coefficient, c^{b} the bulk concentration and t time. The microdisc electrode behaves as though it is a large macroelectrode for very short times.

For intermediate times, edge effects start to become significant and diffusion will no longer be planar. The diffusion layer is quasi hemispherical.

For long times, a steady state is reached and diffusion becomes hemispherical. With microelectrodes, the steady state is reached very fast, more specifically in a time given by equation 1.6.[13]

$$t_{\text{SS}} \simeq \frac{r_{\text{s}}^2}{\pi D} \tag{1.6}$$

This is expression is a function of the square of the electrode radius, meaning the smaller the size of the electrode, the faster the steady state is reached. Mathematically, the current is the integral of the flux of species to the electrode, over the electrode area. When the current becomes constant at long times, it is due to the flux of species to the electrode no longer changing. The size of the diffusion layer is often then considered constant. It will only be affected in situations such as close to a surface, where the surface perturbs the diffusion layer and affects the current, a principle relied on in scanning electrochemical microscopy, or if convection is caused by applied mechanical forces.

The Cottrell equation presented is only valid at very short times (when t tends to $t = 0$ s); the microelectrode then behaves as though a large planar electrode. At the other extreme, for long times, the steady state is reached, for which an analytical solution is also known ($i_{\text{inf,lim}} = 4nFDcr_{\text{tip}}$). The issue here is therefore to bridge the gap between the two cases. In 1982, Shoup and Szabo derived an expression accurate within 0.6% to describe the transient response of a microdisc electrode at all times.[14] A more accurate expression was presented by Mahon and Oldham;[15;16] however this expression is in two parts, making it somewhat less convenient.

1.2.3 From microelectrodes to SECM

Microelectrodes make very good probes for scanning electrochemical microscopy (SECM), due to their inherent properties: low charging currents, reduced ohmic drop, good signal-to-noise ratio and fast attainment of the steady state.

As a direct result of their size, microelectrodes can be used to make measurements in very small domains. However other properties make them interesting for a wide range of experiments.

The charging current, resulting from the current flowing to and from the electrode when the potential is changed, is inversely proportional to the electrode size. As a results, using microelectrodes will reduce the magnitude of distortion due to the charging current.

When a potential difference is applied between two electrodes and a current flows between them, there will always be a resulting ohmic drop:[3]

$$\Delta E = \Delta V - iR \tag{1.7}$$

where ΔE is the potential difference, ΔV is the applied voltage difference between the two electrodes, i is the current and R the resistance. The ohmic drop depends on both the solution resistance and the current: a small current will lead to a decrease in iR drop and of course, the current is proportional to the electrode radius. The resistance is itself inversely proportional to the radius of the electrode and overall, the iR drop at a microelectrode will be constant and more importantly, negligible compared to that at a macroelectrode.

1.3 Scanning electrochemical microscopy: an electrochemical radar

1.3.1 Measurements within the electrochemical layer

In 1986, Engstrom *et al.*[17] introduced the idea of using a microelectrode to make measurements within the diffusion layer of a biased macroelectrode, in order to study the concentration profile of the macroelectrode. The set up was then used to map the activity of a substrate over which the microelectrode was scanned. This is the first example in the literature of a microelectrode being used in the amperometric mode to gather information about a surface by scanning the electrode over this surface of interest. It was however only in 1989 that the term scanning electrochemical microscopy or 'SECM' was coined.[1;2]

1.3.2 Theory of the method

1.3.2.1 The basic principle

Scanning electrochemical microscopy is used to gather information about a surface, called the substrate, by holding or moving an electrochemical probe above

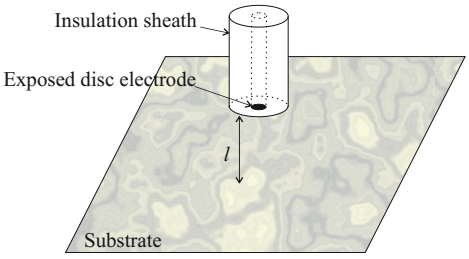

Figure 1.3: Schematic representation of the principle of SECM: a probe made of a conducting core surrounded by insulation is scanned at tip-substrate distance l above a surface of interest to map its reactivity

this surface of interest, as depicted in figure 1.3. The SECM probe typically consists of a microelectrode, with a surrounding insulation sheath. The current is recorded at the electrode in the presence of a redox mediator, as the electroactive probe is scanned in the x-, y- and/or z-direction. The perturbation of the diffusion layer by the substrate is reflected in the current measured and will thus reveal information about the surface scanned. The substrate can be solid (e.g. glass, metal or polymer), liquid (e.g. mercury) and even gas.[4;18]

1.3.2.2 Feedback mode

The feedback mode, depicted in figure 1.4, is the most popular mode of operation in SECM. The tip is immersed and the presence of a redox mediator in solution results in an electron transfer at the electrode tip when a potential is applied: a redox reaction then occurs at the electrode surface. In the bulk, diffusion to

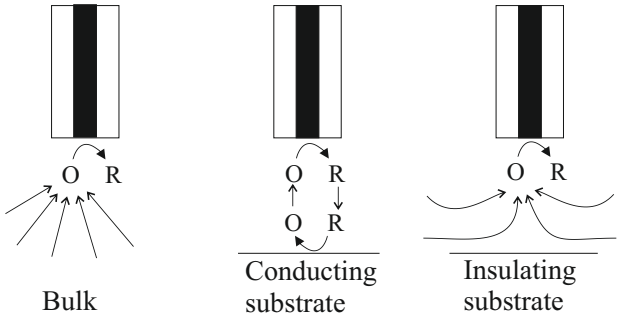

Figure 1.4: Diffusion to the electrode in the feedback mode: in the bulk, hemispherical diffusion. At a conducting substrate, the opposite reaction occurs whereas an insulating substrate blocks diffusion with species needing to come from further away

the electrode will be unperturbed and hemispherical. The probe is then brought

closer to the substrate, which can be inert, conducting or a combination of both such as a conducting island in an insulating substrate. The perturbation of the diffusion layer by the substrate will be reflected in the current. At a conducting substrate, the reaction taking place will be the opposite of the one occurring at the electroactive probe. As such, the species depleted at the electrode will be regenerated at the substrate. However at an inert surface, no reaction will take place.

The traditional method of conducting an SECM experiment is to create an approach curve. The experiment will begin with the tip positioned in the bulk. The tip-substrate distance is then iteratively decreased until in close proximity of the substrate. The tip is first moved closer to the surface, the steady state is reached and measurements are made. The tip can then be moved again. Initially, these steps are large, however closer to the electrode, they will be much smaller for two reasons: firstly, tip crashes must be avoided. Secondly, the aim of the experiment is to study the processes occurring at the surface of interest, once the tip is close to this surface. Decreasing the distance steps will results in a larger amount of data, and thus more information about the activity close to the substrate. The measured current, normalised by the current in the bulk, can then be plotted as a function of the tip-substrate distance to create an approach curve. These approach curves are independent of the solution used for a well behaving redox couple, and only reflect the electrode geometry and tip-substrate distance and can thus be used to gather a lot of information about not only the reactivity and topography of the surface scanned, but also the geometry of the electroactive probe.

Approach curves over conducting and insulating surfaces are shown in figure 1.5. Far away from the substrate, diffusion is unperturbed. As the current for any tip-substrate distance is normalised by the current in the bulk, until the substrate perturbs the diffusion to the electrode, the normalised current recorded will be 1. The current only begins to change when the diffusion layer reaches the surface.

Positive feedback Positive feedback occurs when the electrode approaches a conducting surface. The species that is consumed at the electrode is regenerated

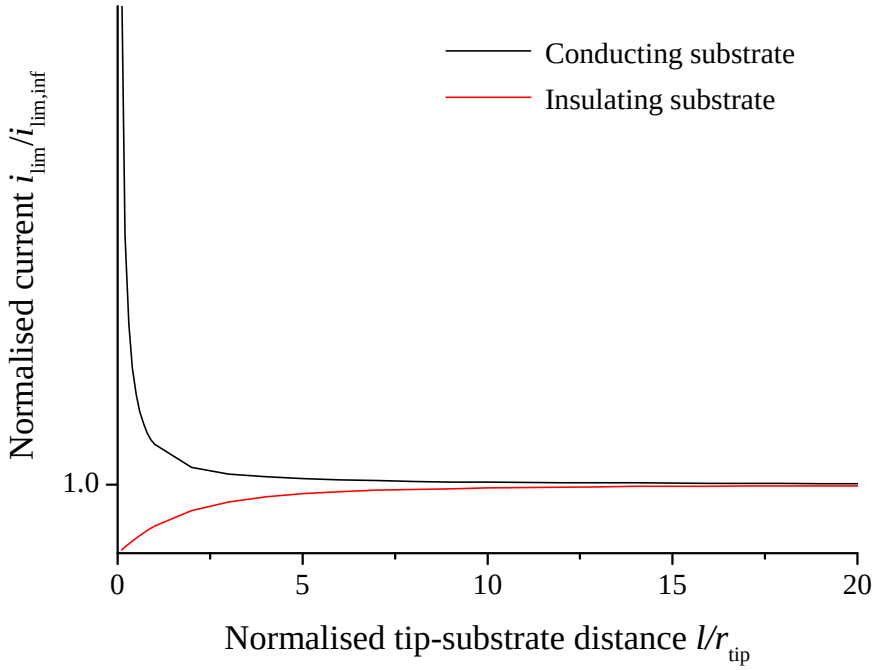

Figure 1.5: Typical approach curves over conducting and insulating: the normalised current is plotted as a function of the normalised tip-substrate distance

at the substrate, where the opposite reaction occurs to the one at the electrode. As the tip-substrate distance decreases, and the tip is in proximity of the substrate, the current will begin to increase, as observed in figure 1.5. This is due to the regeneration of species at the substrate affecting the diffusion to the electrode and can easily be explained by thinking of the change in diffusion layer as it approaches the substrate. In the case of positive feedback, the substrate will be a source of oxidised species ready to diffuse towards the electrode and be reduced. The diffusion layer size will therefore be reduced with decreasing tip-substrate distance, as species will not have to come from far to react at the electrode. As a result of the substrate perturbation, the current will increase. This increase in current will be geometry dependant. With disc electrode and low aspect ratio cones, the current can be as much a eight times larger than in the bulk, whereas with very protruding tips, the current for $l/r_{tip} = 0.1$ can sometimes be only 50% bigger than in the bulk. The contrast is defined as the magnitude of the response in approach curves. Very protruding tips will exhibit very little contrast whereas high contrast will be observed for disc electrodes.

Negative feedback If the surface of interest is inert, diffusion towards the electrode will be hindered, with negative feedback also being known as hindered diffusion. The species to be oxidised at the electrode must come from further away as the probe approaches the substrate, see figure 1.4, as a result of the substrate blocking diffusion to the electrode. The diffusion layer will therefore be spread out due to the shielding by the insulating substrate and the current at the electrode will decrease with decreasing tip-substrate distance, as observed with the red curve in figure 1.5. Previous studies showed the current to be highly dependent on the radius of the insulating sheath.[2]

1.3.2.3 Other modes of operation

Substrate generation/Tip collection The first measurements within the diffusion layer of a macroelectrode using an electrochemical probe were performed in the SG/TC mode.[17] In this mode, the substrate generates a species that is then collected at the tip, whilst simultaneous measurements of the tip and the substrate currents are performed. The electrode probes the reactions occurring at the substrate. With a sufficiently small electrode, the diffusion layer of the substrate is not affected allowing measurements at the microelectrode to reflect local concentration changes.[19] This mode has been used in a range of examples such as looking at mass transport of species through pores of the skin[20] by imaging the concentration profile using a $z-$direction scan, studying oxygen reduction[21] or determining the kinetics of substrate reactions.[22–24] Simulations have increased the understanding of processes in this mode: Martin and Unwin derived a method of calculating the ratio of diffusion coefficients of the redox mediator couple without information on the two electrodes or their separation, while Sklyar *et al.* determined the resolution of tips in the SG/TC mode and the dependence of resolution on the different factors of the experiment.[25] However, a theoretical study of an amperometric SG/TC mode is complicated due to several factors: the substrate diffusion layer will be perturbed by convection created by the moving of the electroactive probe, which moreover blocks diffusion to the substrate.[4]

Tip Generation/Substrate Collection In the TG/SC mode, a redox reaction occurs at the tip upon application of a potential, and a species is generated which will be detected at the substrate, at which the opposite reaction occurs. This is similar to the feedback mode, although in this mode, unlike the feedback mode, the current at both the substrate and the tip is monitored. High collection efficiency is characteristic of this mode, making it useful for many problems such as determining the kinetics of chemical reactions.[24;26;27] This mode is also advantageous as not all reactions can be studied in the feedback mode. Moreover, the TG/SC mode is less sensitive to the tip to substrate distance making it more adequate to study uneven surfaces.

Competition mode In the competition mode, the same reaction occurs at both the electrode and the substrate. This has been used for example with ring disc electrodes where species will be reduced at the disc but oxidised at both the ring and the substrate.[28;29]

1.3.3 The influence of the probe geometry in SECM

A range of fabrication methods have resulted in various geometries including (and not limited to) the following: sphere cap,[30] hemispherical,[31] ring,[32] conical,[33–35] and of course, the most popular, disc. Simulations have, from the first SECM publication,[1;2] been an important part of literature on the method. Users have relied on modelling to understand the processes occurring in solution and to validate experimental results. More importantly, simulations in SECM have been extensively used to enable users to extract information about the geometry of the probe, as well as the kinetics of the system.

1.3.3.1 Disc electrodes

Disc electrodes, see figure 1.6a, are the most popular microelectrode geometry for a range of reasons. They are easy to fabricate and easily polishable. One possible fabrication process is covering a wire of the desired width with glass, silica or another insulating material, then polishing the electrode to form the disc. The

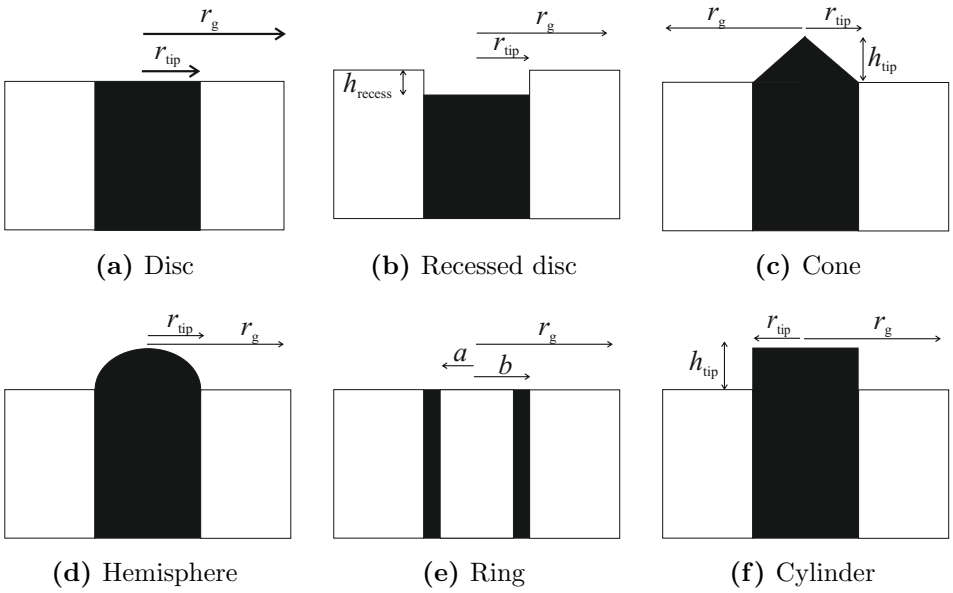

(a) Disc **(b)** Recessed disc **(c)** Cone

(d) Hemisphere **(e)** Ring **(f)** Cylinder

Figure 1.6: (a) Disc electrode, described by its radius r_{tip} and the insulation sheath thickness r_{g}; (b) Recessed disc electrode, described by its radius r_{tip} and the insulation sheath thickness r_{g}, as well as the depth of the recess h_{recess}; (c)Conical electrode, described by its radius r_{tip}, its height h_{tip} and the insulation sheath thickness r_{g}; (d) Hemispherical electrode, described by its radius r_{tip} and the insulation sheath thickness r_{g}; (e) Ring electrode, described by the inner ring radius a, outer ring radius b and the insulation sheath thickness r_{g}; (f) Cylindrical electrode, described by its radius r_{tip} and height h_{tip} and the insulation sheath thickness r_{g}

disc electrode is described by the radius of the electroactive region r_{tip} and the radius of the surrounding insulation sheath r_{g}. Typically the insulation sheath radius will be normalised and referred to as $R_{\mathrm{g}} = {}^{r_{\mathrm{g}}}/_{r_{\mathrm{tip}}}$. Diffusion to this type of microelectrode is hemispherical, as illustrated in figure 1.2 for long times and the steady state current is given by the following equation:

$$i_{\mathrm{lim,inf}} = 4nFDc^{\mathrm{b}}r_{\mathrm{tip}} \tag{1.8}$$

The subscript used in $i_{\mathrm{lim,inf}}$ refers to the **lim**iting current i at an electrode for '**inf**inite' tip-substrate distance, i.e. in the bulk. This is however only valid for a very large insulation sheath thickness. In practice, the R_{g} of electroactive probes fabricated will typically be anything from $R_{\mathrm{g}} = 1.1$ to $R_{\mathrm{g}} = 60$, which will result in diffusion around the corners of the insulation sheath for the smaller radii. Equation 1.9 has been derived to take back diffusion into account when

calculating the limiting current at an electrode in the bulk.[36]

$$i_{\mathrm{lim,inf}}^{\mathrm{disc}} = 4nFDc^{\mathrm{b}}r_{\mathrm{tip}}\left[1 + \frac{0.23}{\left(R_{\mathrm{g}}^{3} - 0.81\right)^{0.36}}\right] \tag{1.9}$$

Expression 1.9 will give the current at the microdisc electrode for any insulation sheath thickness to within 0.3% accuracy.

An important contribution to the SECM community was made by Amphlett.[37] The importance of the insulation sheath thickness on the bulk limiting current at microdisc probes had by then been established, as discussed in the previous section, however its effect had not been measured when close to a surface. Approach curves for a range of R_{g} were generated and revealed the extent of this influence, which is particularly pronounced over an insulating surface. The insulation sheath thickness affects the tip-substrate distance at which the current begins to differ from the bulk current. Theoretical expressions were also fitted to the data, although more accurate expressions have since been developed, for both positive and negative feedback.[38;39]

A common problem with SECM is the probe approaching the surface at an angle. Simulations have been key in investigating the influence of this defect with Fulian *et al.*[40] modelling approach curves for different angles. This was also investigated by Cornut *et al.*[41]

An aspect of scanning electrochemical microscopy that has not often been considered is the influence of the convection effect created with the motion of the probe. This can be ignored if the velocity of the probe is small, as determined Cornut *et al.* who modelled forced convection caused by large scan speeds and derived an equation to estimate the maximum approach velocity υ:[42]

$$\upsilon = \frac{DR_{\mathrm{g}}}{r_{\mathrm{tip}}(115 + 22.R_{\mathrm{g}}^{1.9})} \tag{1.10}$$

This equation provides users with guidelines as to what speeds can be used: velocities faster than the one calculated above would result in a breakdown of the steady state behaviour, for which theory is known.

Typical defects of the microdisc probe include imperfect seal between the insulation and the electroactive material, off centred tip, slight recess of the disc electrode and elliptical shape of the electroactive region. These have been investigated by Aoki *et al.*[43] and Cornut *et al.*[41] who, for each defect, derived equations for users to determine the actual dimensions of the geometry. A selection of tips presenting a combination of defects were also presented in the publication by Cornut.

1.3.3.2 Recessed disc electrodes

There are two main types of recessed disc electrodes: the ones intended to be recessed and the ones that are not. Recessed electrodes are, as with the disc electrodes, described by the radius of the electrode and the radius of the insulation sheath, as well as the height of the recess as shown in figure 1.6b.

Recessed electrodes were also used in SECM, with the influence of the recess magnitude on the current when approaching entirely insulating and conducting surfaces investigated using experiment and simulations.[44] In this publication, it was shown that voltammetry would lead to an accurate estimation of the tip parameters. The larger the recess, the smaller the contrast over a conducting substrate. Over an inert surface, larger recesses would lead to minimized contrast for larger tip-substrate distance, compared to small recesses. However, when very close to the surface, currents for all recesses would tend towards the same value.

Mostly, the recess of an electrode is due to a defect, which is why its influence has been investigated using simulations, both in the bulk solution[45;46] as well as in SECM experiments.[41]

Applications include the use of recessed electrode as oxygen sensors for oceanographic study, which was investigated as the effects of convection on the diffusion layer as well as horizontal diffusion of species were found to be minimized due to the recess.[47] A "micro cavity" was introduced, enabling the study of the interface between an organic phase and an aqueous phase.[48] This shape electrode was however shown to be ambiguous when attempting to extract kinetic information from a surface.[45]

1.3.3.3 Conical electrodes

Conical electrodes can be made with cylindrical insulation, as well as conical insulation. The diffusion limited current to a finite conical electrode with cylindrical insulation can be determined using an expression reported by Zoski and Mirkin.[35] Conical electrodes are described by three parameters at least, see figure 1.6c: the radius and height of the electroactive cone and the radius of the insulation. The critical dimension will typically be the radius. The aspect ratio is generally used to describe the cone sharpness, which is the ratio of the cone height over the cone radius. This shape electrode, shown in figure 1.6c will be discussed in detail in chapters 3 and 6. SECM experiments with rounded conical electrodes with a range of aspect ratio were modelled, and compared against a disc electrode, which revealed that the best contrast is observed for disc electrodes.[49]

1.3.3.4 Hemispherical electrodes

The theory of the current response at a hemispherical electrode, such as the one shown in figure 1.6d, is well known,[50;51] with the expression to calculate the limiting current, for r_{tip} the radius of the hemispherical electrode:

$$i_{\text{lim,inf}}^{\text{hemisphere}} = 2\pi nFDc^{\text{b}}r_{\text{tip}} \tag{1.11}$$

These are not very commonly used microelectrodes although protruding tips are often approximated as being hemispherical, for simplicity. SECM experiments have been performed with hemispherical electrodes. Positive and negative feedback currents were generated using the boundary element method. The geometry of the hemisphere was varied and it was determined that the difference between the cases over an inert substrate were less pronounced.[40] Further research revealed reduced feedback currents compared with disc electrodes: under positive feedback, a current three times the bulk current is reached with the hemispherical electrode, compared to eight times the bulk current recorded with a disc electrode of the same radius. This loss in contrast is due to the protrusion of the electrode.[31] This publication also presented expressions to plot the theoretical

positive and negative feedback current. This expression is however only valid for dimensionless tip-substrate distances between 0.1 and 2 and does not take into account the insulation sheath thickness, being only valid for $R_g = 10$. Expressions were fitted to simulated approach curves for sphere cap electrodes of varying degrees of protrusion over conducting and insulating substrates.[30]

1.3.3.5 Ring and ring disc electrodes

Ring, see figure 1.6e, and ring disc electrodes are fabricated by depositing successive layers of insulating and conducting layers. Ring disc electrodes have been mostly used in the rotating ring disc set-up, using well defined convection to bring species vertically towards the disc where the species can be reduced, then transported horizontally towards the ring where the reduced species can be detected. This geometry will be described in more detail in chapter 7. Ring and square frame electrodes have also been seen in AFM-SECM probes, with the sharp AFM tip protruding from the ring or frame shaped electrode.[52–54] Disc and ring radii will be used to describe the geometry, although using the ratio is a popular method of comparing the geometries with a uniform parameter. The most accurate ring expression found takes into account both the insulation sheath thickness and the ratio of the outer ring radius over the inner ring radius:[55]

$$i_{\mathrm{lim,inf}}^{\mathrm{ring}} = i_{lim,inf}^{\mathrm{disc}} \left[1 - 0.3 \left(\frac{a}{b}\right)^{4.4}\right] \tag{1.12}$$

$i_{lim,inf}^{\mathrm{disc}}$ is the expression for the limiting current at a disc electrode, see equation 1.9, giving an accuracy for equation 1.12 of within 1.2%. The influence of the insulation sheath thickness is therefore taken into account in the 'disc-part' of the equation. Cornut *et al.*[55] used the finite element method to fit expressions to theoretical approach curves for ring electrodes. The influence of geometrical parameters were investigated: insulation sheath thickness and the ratio of ring radii.

1.3.3.6 Band and cylindrical electrodes

As mentioned above, both band and cylindrical electrode present the advantage of being able to keep the critical dimension very small whilst keeping the current high, thus making it easier to measure. The critical dimension of bands will be their width, and the radius for the cylinder, as shown in figure 1.6f.

The steady state is however never reached with these electrodes.[4] The transient response has however been determined.[56] In the same publication, an equation was derived to calculate the steady state current at a capped cylindrical electrode:

$$i_{\text{lim,inf}}^{\text{cylinder}} = 4 + 0.1506H^{1.152} + 3.397H^{0.7220} \tag{1.13}$$

Scanning electrochemical microscopy experiments have successfully been performed and modelled with a band electrode.[57] As mentioned previously, a steady state current is not expected with band electrodes, thus making diffusion difficult to model. However this publication proposes that the presence of natural convection during the scan would create a quasi steady state mode, thus enabling an accurate prediction of the tip behaviour.

1.3.3.7 Arrays of electrodes

Arrays of lines, discs and cones have been fabricated.[58;59] An important parameter of arrays fabricated is the separation between the electrodes. If very far apart, diffusion will be independent of the surrounding electrodes and the current measured will be the sum of the current at each individual electrode. However as this separation decreases, the diffusion layers begin to overlap. Eventually for small enough separation, or long enough time, the array behaves as though it is a single electrode of larger size.

An array of cones, fabricated by covering an etched optical fibre bundle with thousands of nanotips, has been used to pattern a surface.[59] It was determined using simulations that the array, depending on the overall aspect ratio, exhibited a behaviour closer to a single hemispherical electrode. However by pulsing the potential, the size of the diffusion layer was controlled so that each tip behaved

as though independent of the surrounding electrodes, thus enabling an array to be electrochemically printed on a surface of interest.

1.3.4 Applications of SECM

The applications of scanning electrochemical microscopy are wide and varied. A selection of these are mentioned below. For many of these, it will be necessary to resolve very small regions such as skin pores and corrosion pits. Others will need a good response to kinetics at the substrate scanned. A high level of sensitivity is required from the SECM probes.

- Corrosion on metal coated surfaces[60;61]
- Transport of species through pores, such as through skin pores[20;62] or membranes[63]
- Study of oxide film growth[64] and active sites on oxide films[65]
- Studying DNA strands to identify mismatches[66]
- Imaging enzyme active sites, which has also been modelled.[25]
- Study of polymer samples[67]
- Measurement of electron transfer kinetics[68–70]
- Mapping of catalytic activity[71;72]
- Study of oxygen reduction[73]
- Surface modification[59;74;75]

1.3.5 Future of SECM

A major drawback of scanning electrochemical microscopy is the impossibility of separating the influence of topography on the current measurement from the influence of the substrate reactivity, thus reducing the electrode sensitivity to the

chemistry at the surface scanned. Tip crashes have also been an issue with very small microelectrodes and rough surfaces.

Several methods have therefore been investigated to allow for more accurate measurement.

1.3.5.1 Shear force SECM

The combination of shear force with SECM was introduce to enable constant distance mapping of a substrate.[76] In this mode, sharp 'needle'-like SECM probes have been reported to increase the lateral resolution by minimizing the influence of the topography on the measurement.[77]

1.3.5.2 Soft stylus probes

A possible solution to the constant distance scanning issue was introduced by Cortés-Salazar *et al.* who fabricated soft probes that would be used to scan both in non-contact and in contact mode.[78] The scan can be performed with the probe bending as it contacts with the surface of interest, thus enabling the scan of rough surfaces without the risk of damaging them, as well as ensuring control of the tip-substrate distance.

1.3.5.3 AFM-SECM

The need to study and image surfaces to a submicron resolution led to the combination of scanning electrochemical microscopy and atomic force microscopy. In SECM, a microelectrode is scanned over a surface to map its reactivity, whereas in AFM a sharp tip at the end of a cantilever is used to determine the topography of a surface on the atomic scale.[79] This method is being developed in this project and will thus be discussed in greater detail in the following section.

1.4 Atomic force microscopy-scanning electrochemical microscopy

1.4.1 The emergence of the method

1.4.1.1 From scanning tunnelling microscopy to atomic force microscopy

The scanning tunnelling microscope (STM) - precursor to the atomic force microscope - is a method of imaging a surface by applying a voltage to a metal wire tip held a few nm above a surface that was developed by Binnig and Rohrer in the 1980s.[80] Scanning tunnelling microscopy allows for forces as small as 10^{-18} N to be measured thus making it a very high resolution scanning method with measurable distances of 10^{-1}Å. Surfaces can be scanned by keeping the tunnelling current between the sharp tip and the surface constant, with the sharp tip never coming in contact with the surface. There is however a major disadvantage with STM, as only conducting and semi-conducting surfaces can be imaged. Atomic force microscopy was later introduced by Binnig *et al.*[81] as a solution to this problem, with a probe that could be used to image a surface of any material (e.g. glass, polymers,biological sample ...).

1.4.1.2 The theory of atomic force microscopy

The basic principle of the atomic force microscope is the same as the principle of the scanning tunnelling microscope: the surface topography will be measured by holding the atomic force between the probe tip and the surface to a constant value using a feedback system and measuring the deflection of the cantilever as it is scanned above the surface of interest. The sharp tip is found at the end of a cantilever, which is described by its spring constant k. This is the most important parameter of the atomic force microscope. The magnitude of the force between the sharp tip and the surface is given by equation 1.14, where k is the spring constant of the cantilever and x is the cantilever deflection.

$$F = -kx \tag{1.14}$$

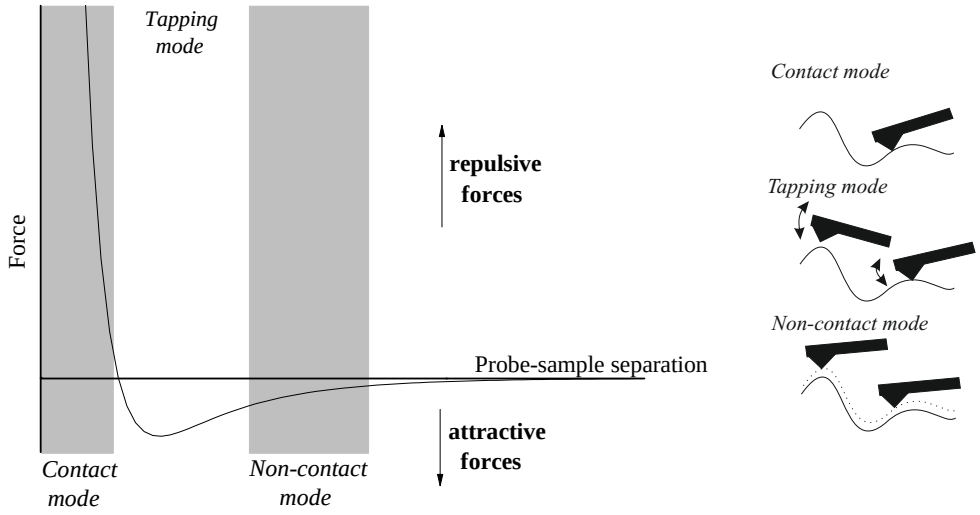

(a) Plot of the force as a function of the tip-substrate distance **(b)** AFM modes

Figure 1.7: Plot of the force between the AFM tip and the surface as a function of the tip-substrate separation

The probes are typically made of silicon or silicon nitride. Parameters such as length and material can be varied to obtain different spring constants. When considering what type of spring to use in the AFM-SECM cantilever, it was important to take into account that a soft spring would be necessary to ensure the largest response to the applied force, to increase sensitivity; however, a high resonant frequency is also needed to minimize the influence of surrounding noise. The resonant frequency f is proportional to the square root of the ratio of the spring constant k over the effective mass m_0.[81] Thus k must be small to ensure the spring is soft, and m_0 of the spring must consequentially be decreased to keep the resonant frequency large.

Three modes of scanning can be used in atomic force microscopy and these depend on the force between the tip and the surface scanned, and thus on the tip-substrate distance. The plot of the force as a function of the separation can be seen in figure 1.7.

- Close to the surface, within half a nanometre, the forces become repulsive and the contact mode can be used. This mode relies on maintaining the cantilever deflection to stabilise the force between the tip and the sample

and thus image the surface. This is advantageous for rough samples however there is a possibility that softer samples can be deformed by the forces.

- Far away from the surface, the dominant forces are attractive Van der Waals. This is considered to be for distances larger than 0.1 nm, region in which non-contact AFM is applicable. Due to the large distance between the sample and the tip, the forces applied are low, thus avoiding any damage to the sample and the probe. However the resulting resolution is lower than with other modes.

- In between the two, the tapping mode can be applied. The tapping mode is applied by oscillating the cantilever as a constant frequency. The cantilever will contact the surface of interest. The surface is imaged thanks to the constant tip interaction that can thus be kept. This mode will require slower scanning speeds in liquids and may damage the sample.

As mentioned previously, the advantage of the atomic force microscope is that, unlike with STM, surfaces that are not conducting can also be imaged. However for high resolution mapping, a sharp tip is required. A low aspect ratio tip will result in a loss in resolution, as depicted in figure 1.8.

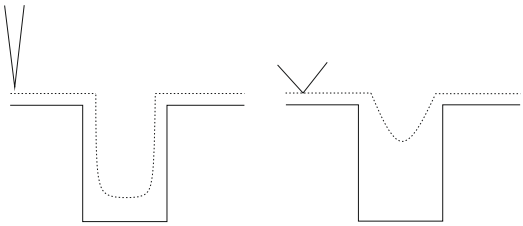

Figure 1.8: Influence of the aspect ratio on the scan path of an AFM tip

Since its appearance in 1986, atomic force microscopy has rapidly grown, with the original paper by Binnig *et al.*[79] quoted almost in over 7000 other publications. Tips are now readily available to purchase which has helped with the increase in use, as the difficult fabrication process could often deter users from using atomic force microscopy.

1.4.1.3 Appearance of the combination of electrochemical and high-resolution topographical measurements

In 1996, Macpherson *et al.*[82] introduced the concept of combining atomic force microscopy with electrochemical measurements. An entirely coated AFM cantilever was used to scan a potassium bromide face, electrochemically inducing dissolution of the surface, whilst continuously monitoring the change in topography using AFM imaging. This is the first example of the combination of an atomic force microscope with an electrochemical probe.

1.4.2 The development of the hybrid method

In 2000, Macpherson and Unwin[83] highlighted problems faced in SECM: the influence of the tip-substrate distance is reflected in the current measurement thus reducing the resolution of the electrochemical measurement; moreover there is a possibility of damage to the conducting probe and the substrate due to tip crashes. Both of these issues are a result of constant height scanning. Atomic force microscopy is a method of scanning at constant distance. By integrating a microelectrode in the AFM probe, the tip-substrate distance can be controlled. The first publication by this group combining the two methods used an entirely coated cantilever which had too big an exposed electroactive region to have good electrochemical resolution. The area of electrode was thus required to be much smaller, although another option was investigated which involved using a pulse to apply the potential thus limiting the spread of the diffusion layer and improving resolution.[84] The cantilevers presented in this publication were fabricated by etching a microwire to form a sharp conducting tip and coating it with glass to form the surrounding insulation, resulting in conical electrodes with effective radii ranging from 50 nm to 2.5 μm. Theoretical approach curves were used to fit the experimental data and thus deduce the dimensions of the exposed area. Different applications were then investigated such as the imaging of a porous membrane, where pores of 1.5 μm to 0.7 μm diameter were individually resolved. The dissolution of a crystal surface was also studied, driven by the electroactive

area during the scan and monitored by the AFM part of the probe.

A popular mode of imaging, used in this project, is electrochemical imaging using the lift mode. The AFM probe is first used to scan the topography in the contact mode. The surface can then be scanned once again, this time applying a potential to the electrode to perform electrochemical measurements at constant distance. This method was successfully used to image a conducting island embedded in an insulating matrix.[85] Later on, systems such as imaging of pores[86;87] and dissolution of calcite[88] were studied using AFM-SECM with a small exposed region.

A pioneering method of fabricating AFM-SECM probes was introduced by Kranz *et al.*[52] A commercially available cantilever was sputtered with gold coating, with the thickness ranging from 100 nm to 300 nm controlled by the sputter time. The coated cantilever was then insulated by coating it with a layer of silicon nitride. Focused Ion Beam (FIB) was used to shape the probe apex so that a square frame shaped electrode is exposed with an insulating tip protruding to act as the AFM tip. A model substrate was successfully imaged, thus confirming the suitability of the probes for combined AFM-SECM measurements. A similar fabrication method was used to produce ring shaped electrodes.[89] The frame shaped electrode as well as an integrated disc electrode were used to map enzyme activity[90] using the tapping mode, where the cantilever is oscillated at a given frequency. This mode was also applied to study conducting rings embedded in an insulating matrix.[91] The same group later developed a new batch fabrication process to make recessed ring electrodes.[92]

The potential of AFM-SECM was obvious very early into its discovery and several groups began working on developing the method. Abbou *at al.*[93] fabricated probes with conical and spherical tips by applying a voltage to a insulation-coated microwire, thus revealing the electroactive region. The probes were characterized by cyclic voltammetry and revealed effective disc radii ranging from 550 nm to 150 nm were obtained. These electroactive probes were later on functionalised,[94] using redox labelled linear polymer chains. When the probe is close to the substrate, the oxidised species at the head of the chain is driven to the substrate,

where it is reduced. The polymer chain head will go back and forth between the tip and the substrate, transferring electrons, which is reflected in the current measured: positive feedback is observed. A similar study was performed with DNA chains attached to the substrate.[95]

Other shapes have been investigated: triangular shaped electrodes, resulting from batch fabrication process, were introduced in 2005.[96] AFM-SECM probes were fabricated with disc electrodes at the apex, with either a protruding cone or the tilted edge acting as the AFM tip.[97] Hybrid probes with conical tips were also fabricated by Gullo *et al.*[98] and used to image biological membranes. Wain *et al.*[99] presented the fabrication of sharp needle like probe, in which a disc electrode of 140 nm radius is used as an AFM-SECM probe. The blunt tip of a needle meant with respect to AFM, the resolution was lower than for sharper conical tips. However with respect to electrochemical resolution, a disc electrode will have better resolution than a recessed square electrode or sharp conical electrode.

AFM-SECM has also been combined with a third method: alternating current, which enabled impedance mapping as well as electrochemical and topography mapping.[100]

1.4.2.1 Simulations in AFM-SECM

With such tips being difficult and expensive to make, numerical simulations have become an integral part of AFM-SECM studies. Sklyar *et al.* modelled diffusion towards frame shaped electrodes in 3D using the boundary element method.[49] These probes have a frame shaped electrode, from which a conical tip protrudes. Thanks to modelling of approach curves over substrates of different kinetics with and without the protruding tip, it was established that the inert AFM tip did not significantly perturb diffusion to the electrode. The influence of the geometry on the sensitivity, determined from the contrast observed in the approach curves, was also investigated. Simulations of entirely insulating cantilevers of different shapes have been performed to determine their effect when approaching conducting islands.[84] Diffusion towards entirely conducting cantilevers has been modelled in transient 3D simulations, when the probes were held above insulating surfaces

and above conducting islands within insulating surfaces; the aim of this was to investigate the influence on the concentration profile of the application of short potential pulses.[84] Simulations of AFM-SECM probes with disc electrode have looked into the influence of flow on the concentration profiles at the electrode. Imaging of neighbouring active sites was also modelled to study the influence of geometry and tip-substrate distance on imaging capabilities of the probes.[97] Conical electrodes with conical insulation as seen in AFM-SECM have been simulated, both in 2D and 3D, to compare the effect of the surrounding insulation on the diffusion to the cone. The modelling in this publication was also used to verify the experimental current calculated and investigate the influence of a simple defect on the limiting current.[98]

1.4.3 Fabrication method of our AFM-SECM probes

AFM-SECM is therefore a very promising and exciting combination of methods, which leads to a very high resolution way of mapping the reactivity of a surface of interest, thanks to a nano- or microelectrode integrated into an AFM probe and the possibility to reduce the influence of tip-substrate distance on the current measurement. The experimental aim of this project was to produce a probe, with the electrode at the apex of the conical tip, to ensure the best resolution was obtained. The electrode tip will be acting as the AFM tip, compared to having a recessed electrode with a protruding AFM tip.[52] A fabrication process was developed by Amra Avdic[101] at the Technical University of Vienna, summarised in figure 1.9.

The fabrication process begins with a commercially available AFM cantilever, represented in figure 1.9(a). This can be either a standard inert silicon cantilever or purchased already layered with a conducting layer such as boron doped diamond. The silicon cantilever has to be firstly covered with an adhesion Ti layer, followed by an Au layer or another electroactive material. The next step is the coating with a further Ti adhesion layer. Both types of probes can then be sputtered with Si_3N_4 to form the surrounding insulation sheath by plasma enhanced chemical vapour deposition; it will take 50 minutes to coat the probe with a layer

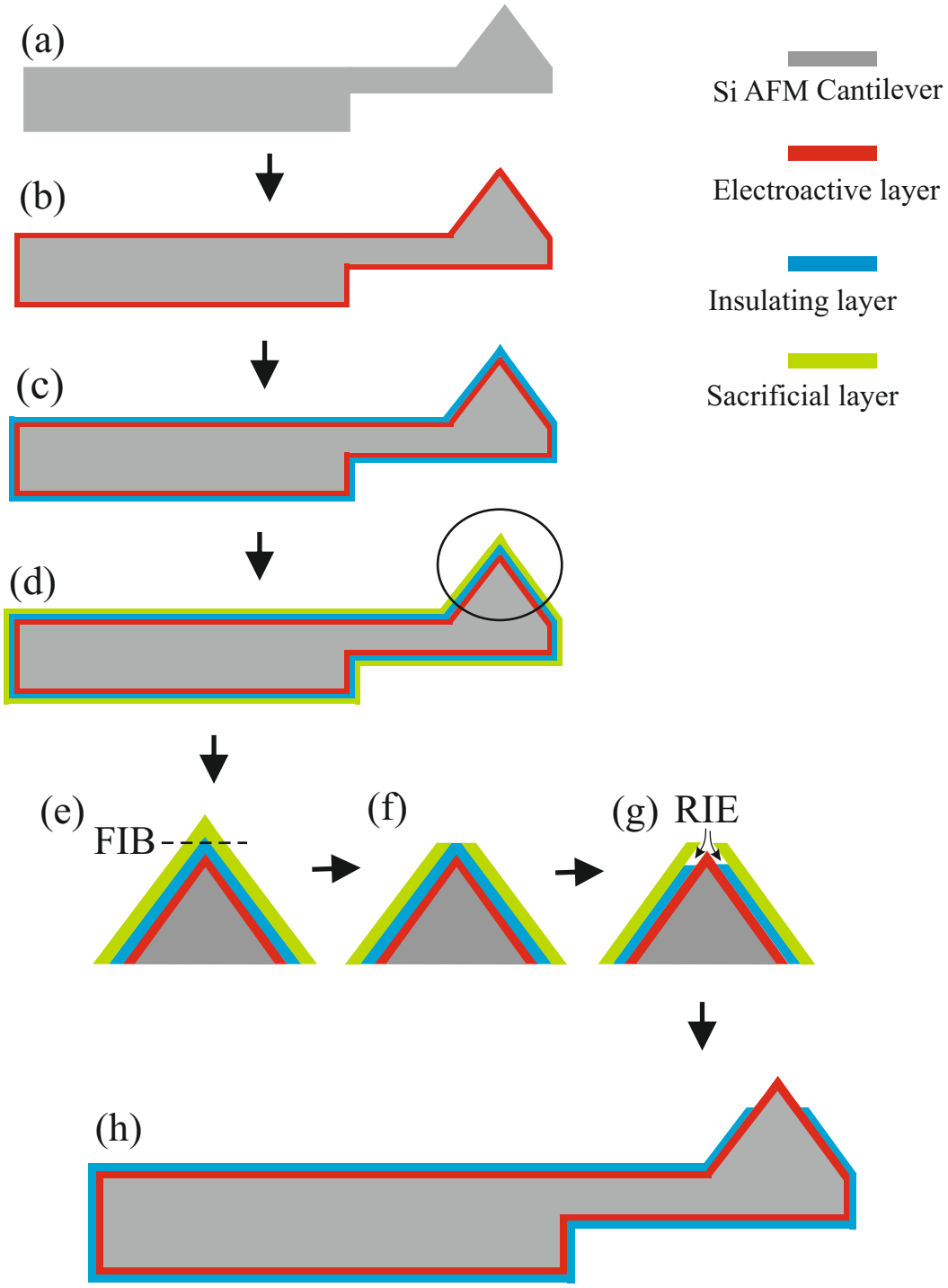

Figure 1.9: The steps of fabrication of the AFM-SECM cantilever: (a) The commercially available Si cantilever; (b) Cantilever is coated with a layer of conducting material such as BDD or Au; (c) Electroactive probe is insulated with SiN; (d) A sacrifical layer of Cr is used to protect the insulation layer; (e) Focused Ion Beam (FIB) is used to remove part of the sacrifical layer as well as some of the insulation, as seen in (f); (g) Reactive Ion Etching (RIE) removes the insulation through the gap left in the Cr layer; (h) The sacrificial Cr layer is removed and the probe is ready.

of 600 nm thickness, see figure 1.9(c). A 50 nm thick sacrificial layer of Cr layer is then deposited on the electroactive probes. The insulation and sacrificial layer covering the apex are then removed using Focused Ion Beam (FIB) to expose a gap in the chromium protection layer. Reactive Ion Etching (RIE) was then used to remove the insulation isotropically from the tip apex to expose the electroactive layer, with the Cr layer protecting the remainder of the tip. This is possible as the etching rate of chromium is much lower than the etching rate of Silicon Nitride. The area of exposed conducting material is controlled by the duration of the etching. The chromium layer could then be removed by wet etching.

This fabrication process results in conical electrodes with conical insulation. The height-to-radius ratio of the electrode will depend on the original probe purchased, as well as the conducting layer. The BDD layer tends to form clusters at the end of the tip, whereas an Au layer would be more likely to have a conical tip with a small radius of curvature. The insulation angle is assumed to have the same angle as the half angle of the conical electrode as a uniform layer thickness is added. However the aspect ratio is not always constant throughout the electrode: it is common and in fact sometimes intentional for the tip to become sharper at the apex. This is advantageous in AFM, as a sharper tip leads to better resolution.

The aim of the simulations performed in this work, in context with the AFM-SECM probes fabricated, is to study in depth the electrochemical behaviour of the conical electrodes with conical insulation as found at the apex of the probe to determine the influence of the tip geometry on the current both in the bulk and close to the substrate.

1.5 Numerical methods in electrochemistry

With analytical solutions to electrochemistry problems difficult to obtain due to complex geometries and conditions, simulations were resorted to, in order to solve the equations describing a system. The numerical simulation of electrochemical systems first appeared in the late 1960s in electrochemistry and in particular, a significant contribution was made in 1969 by Feldberg who introduced the box

method, a finite difference method of solving differential equations.[102] Joslin and Pletcher enabled great progress in terms of computation efficiency, by developing an expanding grid approach to solve electrochemical systems.[103] In 1981, an introduction to digital simulations was written by Britz,[104] aiming to give the basics of finite difference and numerical simulations in general in electrochemistry, with mathematical references at the time unable to cater for the electrochemistry community. Significant progress was then made in the following decade. An extended copy of the digital simulation book was published in 1988, to reflect the large developments made since the publication of the first edition.[105]

Initially, numerical solutions were computed by hand with reports of solutions taking up to 36 hours to reach.[104] Modelling languages for use on computers were created such as Fortran in the mid 1950s. By the mid 1960s, computers were much more developed and simulations grew. However it was only in the 1980s after the publication of the book by Britz and the commercial availability of powerful computers that the use of modelling really took off. Simulations that would have previously taken over a day to solve by hand could be computed in seconds. The last ten years in particular have seen a huge step forward with respect to the complexity of models solvable as well as to the accessibility of modelling to researchers.

Commercially available software such as DigiSim then started to become available.[106] Modelling was until the appearance of such software reserved for the specialist: solvers had to be written by the user, although literature on the matter was, by then, more extensive. 2D models could easily be solved[37;107] and some of the first 3D simulations were seen only ten years ago[108] and were rare as computationally complex and intensive.[109] Now, solvers such as COMSOL Multiphysics are commercially available, resulting in simulations being very accessible to a greater number of scientists. Simulations are no longer restricted to the strong mathematician and experienced programmers. It is however necessary to understand the numerical method as this will help use commercially available software appropriately. Software such as COMSOL should not be treated as black box: buying a camera doesn't make you a photographer...

1.5.1 The finite element method

1.5.1.1 History of the method

The finite element method is a numerical method used to determine an approximate solution to the system of equations describing a scientific problem. This method appeared in the 1940s and grew with the commercial introduction of computers in the 1950s. This was the method most often applied in engineering problems and Bard[1] was one of the first to recognise its suitability for electrochemistry problems. The finite difference method was however favoured for a long time due to its simplicity.

1.5.1.2 Theory of the method

Consider a problem such as diffusion to a large disc electrode. This is described by Fick's second law of diffusion, also known as the governing equation of the problem. The system is a macroelectrode of radius a at which a potential E is applied causing a concentration gradient, which will be the driving force of diffusion. The domain of the model is the volume of the solution, in which the electrode is placed. Finally, the loading conditions are the forces which cause the system to change, such as boundary condition $C = 0$ at the electrode boundary, in our case.

The domain described above is divided into smaller subdomains of simpler geometry, typically triangles and rectangles in 2D and pyramids in 3D, which forms the mesh, see figure 1.10. Each subdomain is known as a mesh element. The mesh of a finite element model will, as mentioned above, be divided into triangles and quadrilaterals, with the nodes acting as boundary elements. The size, shape and position of these do not affect the equations applied, which provide users with a flexible mesh. The simulation domain can have any shape, which is extremely useful in electrochemistry with different and complex electrode geometries.

Once the mesh has been generated, approximations can be made for the unknown variables using a finite number of equations. The system of equations describing the system are approximated by algebraic equations, for each mesh element. These are shown in matrix form. The number of linear equations (i.e.

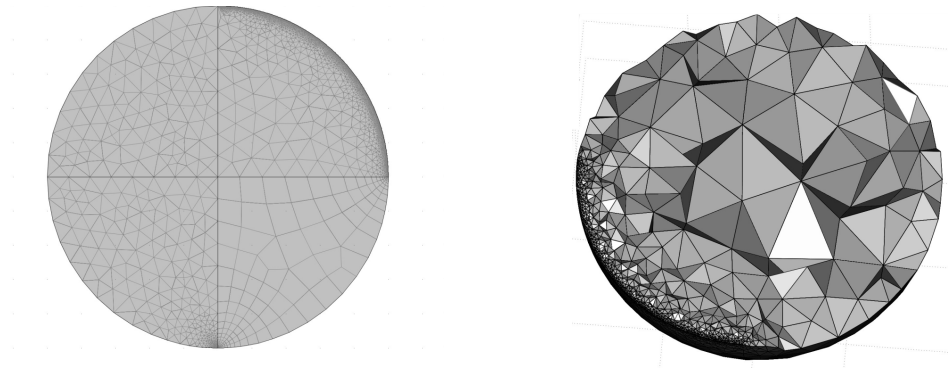

(a) A 2D mesh **(b)** A 3D mesh

Figure 1.10: Example of mesh in 2D in (a) and 3D in (b) showing the flexibility of the mesh in the finite element method. In (a), the top left hand corner is the automatically generated mesh; the top right hand mesh has a single boundary refined, and the size of the elements grow slowly; the bottom left hand side is refined at a single point only at (-1,0) and the bottom right hand section show quadrilateral elements as opposed to triangular like the others. In (b) the mesh is simply refined along one boundary and only element for which $y > 0$ are shown to display the 3D elements inside the domain.

m) is also known as degrees of freedom (DOF) of the model, which is related to the number of nodes of the mesh.

$$\begin{pmatrix} K_{1,1} & K_{1,2} & \cdots & K_{1,\mathrm{n}} \\ K_{2,1} & K_{2,2} & \cdots & K_{2,\mathrm{n}} \\ \vdots & \vdots & \ddots & \vdots \\ K_{\mathrm{m},1} & K_{\mathrm{m},2} & \cdots & K_{\mathrm{m,n}} \end{pmatrix} \begin{pmatrix} c_1 \\ c_2 \\ \vdots \\ c_{\mathrm{m}} \end{pmatrix} = \begin{pmatrix} F_1 \\ F_2 \\ \vdots \\ F_{\mathrm{m}} \end{pmatrix} \tag{1.15}$$

The matrix $K_{\mathrm{m,n}}$ is defined by the equation to solve and $F_{(\mathrm{m})}$ is related to the loading terms or the boundary conditions in our case. The c matrix is the unknown, which represents the concentration at each node.

The algebraic equations are identical for same shaped elements and are called element equations. The method relies on the fact that the mesh elements have simple shapes, making the algebraic equations easier to solve, and that the mesh elements are small, making a good approximation easier to reach with 20 or less equations. The element equations built can then be used not only for other electrochemistry models but any other problem described by finite element. This is relied on by software such a COMSOL which has built a library of element

equations to apply to all modules of the software, from the chemical engineering module to the acoustic module.

The algebraic equations for each element can then be combined into system equations, which are then modified by taking into account the boundary conditions. The problem may be referred to as weak if only first derivative is used to get to the solution. An advantage of the method is that the properties of the domain can vary throughout, even between adjacent boundaries and subdomains. The approximation made over each element will induce error; the method of weighted residuals will often be applied to compensate for this, by distributing the error over each element. The weighted residual form of the equation to solve can then be integrated by parts. A matrix of the numerically computed integrals will be assembled, such as for equation 1.15, to which the boundary conditions can be added. The matrix can then be solved.

This final stage of the modelling process is displaying the results of the system of equations solved. This might be a plot of the concentration profile or further computation can be performed to calculate variables such as the current at the electrode.

1.5.2 Other modelling methods

1.5.2.1 The finite difference method

The finite difference method was for a very long time the preferred numerical simulation method. Its main advantage was that it was extremely simple to implement. In this method, the domain is discretised into regularly spaced points of separation ΔX, called the mesh. It is possible to also have different length spacing of the mesh points. The concentration is then calculated for each of the

discrete points of the mesh by approximating derivatives with algebraic equations:

$$\text{Forward difference: } \frac{\partial C(i,j)}{\partial x} = \frac{C(i+1,j)-C_(i,j)}{\Delta X}$$

$$\text{Backward difference: } \frac{\partial C(i,j)}{\partial x} = \frac{C(i,j)-C(i-1,j)}{\Delta X} \tag{1.16}$$

$$\text{Central difference: } \frac{\partial C(i,j)}{\partial x} = \frac{C(i+1,j)-C(i-1)}{2\Delta X}$$

where C is the concentration of species, ΔX the distance step. Ficks 2$^{\text{nd}}$ law of diffusion, in the steady state, will be:

$$\frac{d^2c}{dx^2} = \left(\frac{C(i+1,j) - 2C(i,j) + C(i-1,j)}{\Delta X^2}\right) = 0 \tag{1.17}$$

The boundary conditions can then be used to calculate the values of C. More complex algorithms have been developed to improve on the explicit and implicit finite difference method, such as alternating direction implicit (ADI).

The main problem with the finite difference method is the lack of flexibility of the mesh used, thus making it difficult to apply for complex geometries. Moreover, to reach the desired accuracy, a very refined mesh has to be used thus increasing the computational time and effort.[109] The domain will be divided in mesh points, with the more points used, the better the accuracy. The limitations of the system means that 2D simulations with complex geometries and 3D simulations are difficult using this method. This was however still the preferred numerical method for a long time.[110]

1.5.2.2 The boundary element method

Fulian *et al.* proposed using this numerical method, thus far more reserved for engineering problems, to resolve the issues encountered with the finite difference method.[40] The boundary element method simply requires the discretization of the the boundaries of the domain, which is advantageous as fewer unknowns will require solving. The system of differential equations describing a problem will be simplified by expressing them as boundary equations. With the boundary element method, the dimensionality of the problem is reduced, thus turning a 3D

problem to a 2D problem. By only taking into account the boundaries, there is a saving in computational effort, which enables a 3D SECM scan to be simulated.

The main advantages are the simplicity of the meshing, as only the boundaries require meshing. Secondly, the boundary singularities can be addressed, thus offering an advantage over the finite difference method. Limitations of the boundary element method include the modelling of several species in solution. Moreover, in some cases, points are still required inside the domain.[109] This method has since been used several times.[25;28;49;108;111]

1.5.2.3 The random walk algorithm

The random walk algorithm works by simulating the possible paths that a species may take, in particular when boundaries are reached. Solving the diffusion equation with this algorithm was described by Nagy *et al.*[50;51] which starts by considering the domain as filled with randomly positioned particles. For each time step, each particle is randomly moved in a random direction. With appropriate boundary condition, such as bulk solution, the problem can be solved. When the particle reaches the electrode boundary or is within the radius of the electrode, it reacts with the electrode and is removed from the domain. With every time step, the charge can be calculated by measuring the particles that have reacted. Each simulation will be run several times to limit statistical variance. This method has a poor rate of convergence, requiring a large computation effort, and thus a long simulation time.

1.5.3 Summary and progress

The first publication in SECM already presented comparison between an experimental approach curve and a simulated approach curve, which was generated using the finite element method.[2] A 2D axisymmetric simulation was run, with a more refined mesh at the electrode edge. Although this initial publication revealed the capability of the finite element method for electrochemistry problems, the simplicity of finite difference method meant this was still the preferred solver.[68] The alternating direction implicit finite difference method proved to be

a good method for transient simulations due to its lack of restriction on time step which resulted in other methods such as explicit finite difference becoming unstable.[31;37;110]

The use of the finite element later on reappeared in SECM literature, with self developed programs[32;112–119] as well as commercially available software.[120] Adaptive finite element used in some of these cases, such as SAFE,[107] is a method of refining the mesh until a certain accuracy is reached. The use of COMSOL (and its predecessor FEMLAB) has been a very popular choice recently, enabling the generation of results for a wide range of cases, to ensure equations derived are as accurate as possible.[38;39;121–125] A wide range of cases can also be considered when studying defects[41] or when wanting to investigate the influence of the electrode shape in comparison with others.[59]

1.6 Structure of the thesis

Chapter 1 has presented a complete introduction from electrode reactions and the theory of SECM to literature on AFM-SECM and a description of numerical methods, in particular in the context of electrochemical systems.

Chapter 2 details the simulation procedure used throughout this project.

Part 1 concentrates on the modelling of conical electrodes with conical insulation:

Chapter 3 will detail the study in the bulk of the conical electrode, with the derivation of a fitting expression to enable users to calculate the limiting current at conical electrodes with conical insulation.

Chapter 4 will focus on the modelling of approach curves using conical electrodes and the influence of tip geometry on the imaging sensitivity of the probe, when using the feedback mode of SECM.

Chapter 5 will concentrate on the simulation of SECM line scans with the conical tips to determine the lateral resolution. Once again, defects modelled will be presented.

Chapter 6 will present the study of kinetics at the substrate; in particular, the influence of kinetics on current measurement at the electrode whilst scanning the surface of interest will be used to extract kinetic information from experimental data.

Part 2 will focus on other electrode reactions modelled:

Chapter 7 will present ring-disc electrodes and the investigation into the influence of geometry on measurements.

Chapter 2

Simulation details

2.1 Introduction to the modelling package

Scientific and engineering problems are described by systems of partial different equations, and often cannot be solved analytically. However, by applying the correct equations, boundary conditions and initial conditions, numerical methods such as the finite element method or the finite difference method, presented in the previous chapter, can be used to solve the set of differential equations.

COMSOL Multiphysics is a commercially available modelling package, which relies on the finite element method. Although COMSOL offers an interface to build and solve models, MATLAB was used in this project. A code is written, defining each step of the modelling process, an example of which is shown in appendix A. COMSOL is called to draw, mesh and solve the problem according to the instructions given in the MATLAB code.

2.2 Details of the finite element solver

The geometry of the simulation domain is made of a single domain which can be split into subdomains, boundary, edges and points. In COMSOL, these are drawn by using basic 2D and 3D geometry objects such as disc and lines in 2D and cylinder in 3D. Geometries can also be created by extrusion of 2D shapes into 3D.

The overall geometry can be designed by assembling different basic geometries together.

Once the geometry has been generated, the domain needs to be meshed. The theory behind meshing was presented in the previous chapter and methodology is presented later on. The basic principle is that the simulation domain and subdomain will be divided into smaller subdomains called mesh elements. Boundaries will also be divided into elements. The COMSOL function *'meshinit'* will provide users with the possibility of refining aspects of the mesh such as maximum element size and growth rate, see appendix B. Once again, 2D meshes can be extruded into 3D.

Once the equations describing the model have been defined, a solver needs to be chosen. Generally, selecting an analysis type, such as stationary or time dependent, is first required. The solver will then be automatically chosen, after an initial test to establish the linearity of the system. It is of course possible to override the solver choice and select another solver, however this was not found to be necessary. Different solvers were investigated and were found to either not return an answer, or not offer a gain in accuracy or computational time and effort. The favoured solver is therefore UMFPACK.[126]

The postprocessing possibilities of COMSOL Multiphysics are extremely powerful: expressions can be integrated over boundaries and subdomains. Variables can be plotted as contour plots, isosurface, or arrows thus allowing users to map the solution of the problem.

2.3 Accuracy of the commercially available solver

As this simulation project relies entirely on using a commercially available package, it was important to determine how to use the software to accurately model problems faced in electrochemistry such as multiscale modelling and difficult boundary conditions. Indeed, without knowing how to use the software, there is a risk of generating inaccurate results.[127] However by starting with the simplest models (linear diffusion, microdisc) to which the solution is known, and working from those models to more complex ones, it is possible to mesh even the

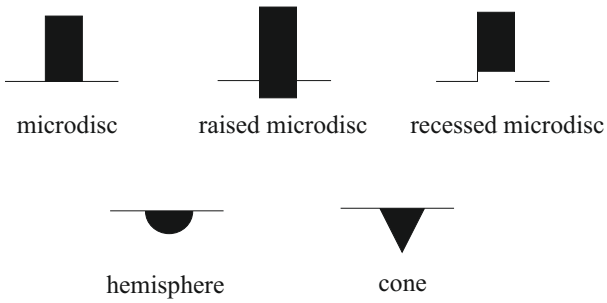

Figure 2.1: Schematic representation of the five tip geometries investigated during the accuracy check of COMSOL Multiphysics

most complicated models accurately, using the method described in the following section. Five geometries were chosen to investigate the suitability of COMSOL to solve electrochemistry problems: a disc, a raised microdisc (or capped cylinder), a recessed electrode, a conical and a hemispherical electrode, represented in figure 2.1, all with infinite insulation. For each case, the limiting current at an electrode was computed in COMSOL and compared to simulations performed in SAFE, an adaptive finite element solver developed by Abercrombie *et al.* which refines the mesh until a specified accuracy is reached.[107] Secondly, simulations are compared to previously reported results in the literature. The results are presented in table 2.1.

Table 2.1: Comparisons undertaken to validate the simulations conditions using typical electrode geometries embedded in infinite insulation sheaths. In each case the absolute relative difference Δ between the simulated value and the reference value is given in %. aFEM is the adaptive finite element solver reported in the publication by Abercrombie and Denuault.[107;128] Raised discs are quantified by the normalised height by which the electrode protrudes ($h_{\text{disc}}/r_{\text{tip}}$). The recessed disc is characterised by the depth of the recess h_{recess} and the cone is characterised by the aspect ratio $h_{\text{tip}}/r_{\text{tip}}$.

Geometry		**2D axisymmetric**		**3D**	
		vs ref.	vs aFEM	vs ref.	vs aFEM
Inlaid disc[129]		$\Delta < 0.03$	$\Delta < 0.1$	$\Delta < 0.4$	$\Delta < 0.4$
Raised disc[110]	$h_{\text{disc}}/r_{\text{tip}} = 1$	$\Delta < 0.8$	$\Delta < 0.1$	$\Delta < 0.4$	$\Delta < 0.3$
	$h_{\text{disc}}/r_{\text{tip}} = 0.1$	$\Delta < 0.9$	$\Delta < 0.1$	$\Delta < 0.4$	$\Delta < 0.3$
	$h_{\text{disc}}/r_{\text{tip}} = 0.01$	$\Delta < 0.8$	$\Delta < 0.1$	$\Delta < 0.3$	$\Delta < 0.5$
Recessed disc[46]	$h_{\text{recess}}/r_{\text{tip}} = 1$	$\Delta < 0.1$	$\Delta < 0.1$	$\Delta < 0.1$	$\Delta < 0.2$
	$h_{\text{recess}}/r_{\text{tip}} = 0.5$	$\Delta < 0.1$	$\Delta < 0.1$	$\Delta < 0.1$	$\Delta < 0.2$
	$h_{\text{recess}}/r_{\text{tip}} = 0.1$	$\Delta < 0.2$	$\Delta < 0.2$	$\Delta < 0.4$	$\Delta < 0.4$
Hemisphere[130]		$\Delta < 0.2$	N/A	$\Delta < 0.5$	N/A
Inlaid cone[35]	$h_{\text{tip}}/r_{\text{tip}} = 5$	$\Delta < 1.2$	$\Delta < 0.2$	$\Delta < 1.4$	$\Delta < 0.1$
	$h_{\text{tip}}/r_{\text{tip}} = 1$	$\Delta < 0.9$	$\Delta < 0.1$	$\Delta < 0.6$	$\Delta < 0.2$

This study of different simple electrodes in the bulk solution revealed that modelling in COMSOL Multiphysics was very accurate, subject to correct definition of the model to solve and a well chosen mesh. The models here were chosen as they had analytical solution or previously reported and verified simulated results and act simply as a way of learning to use the software as well as checking its suitability and capabilities for electrochemical models. The examples investigated as part of the work will be more complex to mesh, as smaller (and more experimentally relevant) insulation sheath thicknesses will be investigated, as well as more complicated electrode geometries and electrodes close to other surfaces. Every model created was carefully meshed using the lessons learnt by meshing the examples mentioned in this section, and for each case, a representative selection was also modelled in SAFE to check for good agreement.

2.4 Meshing in COMSOL

Meshing of the domain has shown to be very important to reach good accuracy when modelling. In electrochemistry models, care must be taken to ensure that bulk conditions are reached. As a result, the boundaries of the domain are required to be far from the electrode boundaries. This makes meshing complicated as elements will need to be extremely refined at the electrode for the simulation to be accurate, but very coarse in the bulk as refined elements would be a waste of computational time and effort in the bulk, where no chemistry occurs. The mesh was therefore built by defining the maximum element size at each point, boundary and subdomain. The element growth rate was also specified for each subdomain, from the boundary with the most refined elements to the boundary with the coarsest mesh. The rate specified is the maximum area ratio between one element and its neighbouring elements. A growth rate of 1.5 means any element could only be up to 50% bigger than the element next to it.

An important trick used in 3D was the creation of so called meshing cylinders, surrounding the electrode tip, see figure 2.3. These are cylindrical objects, with continuous boundary conditions, that enable the mesh elements to be further

refined at the electrode by reducing the element size ratio of the domain, which is the ratio of the area of the smallest element over the area of the largest element. The meshing cylinder also enabled the definition of smaller growth rate for the cylinder and a much faster growth rate for the remainder of the domain.

Typical 2D simulations containing 10000 to 35000 elements would take 1-2 seconds to solve. 3D simulations, containing between 100 000 mesh elements for the simplest models to over 300 000 elements for the more complex models, would take between a couple of minutes and a couple of hours to solve. The simulations were run on a Windows 64 bit, Intel Xeon CPU with 2.66 GHz and 11.9 GB of RAM.

Two types of triangular meshes could be generated in COMSOL, one based on the Delaunay method, the other on the advancing front method. The latter method meshes the domain by starting at the boundaries and progressively adding elements from there. The point that is added will depend on the quality of the resulting element (if the ratio of the sides is close to 1, the element is of good quality), the constraints of the domain, such as other boundaries, and the constraint of the mesh, such a specified maximum element size or element growth rate. This will typically result in higher quality meshes but in this work, was found to be highly unreliable. It was thus specified in all models that the Delaunay mesh should be used. The Delaunay method relies on placing a point within a domain and avoiding placing other surrounding mesh points within its circumscribed circle. Poor quality meshes (i.e. triangles for which the ratio of the sides is far from 1 thus creating 'skinny' triangles) will be avoided by maximising the minimum angles in the triangle.

2.4.1 Example of the meshing of a typical system: the microdisc in 2D axisymmetric

When a model is created and solved using the finite element method, meshing the domain appropriately is one of the most important steps. In particular in electrochemistry, when studying microelectrodes in a large volume of solution, this becomes very difficult. Elements have to be extremely refined at the electrode

and very coarse in the bulk solution. Poor meshing will result in poor accuracy in the result. It is therefore important to understand the solver and know how to use it to achieve the required accuracy. Here, we present the example of the microdisc electrode, for which the theoretical steady state current is known. The steps of creating the model and meshing are presented to give guidelines for users to follow when meshing their own models. This same method is used for all four other geometries and all agree within 1% of another finite element solver and 1% of previously published results.

Consider a microdisc electrode of radius r_{tip} placed in a solution containing a good redox mediator. The microdisc electrode is built in a cylinder of radius 1000 times the radius of the electrode and of height 1000 times the radius of the electrode. This will ensure that the correct bulk conditions are reached. At the microdisc electrode, which is embedded in an insulating matrix, fast electron transfer occurs. The potential applied to the electrode is sufficient to drive the concentration of the mediator to zero. This translates in mathematical terms to $C = 0$ at the electrode: all the species reaching the electrode are consumed instantly. At the bulk boundaries, the concentration will be equal to the bulk concentration, and a no flux condition will be applied to all insulating boundaries. The aim of this section is simply to show the steps of the meshing procedure and chapters 3 to 7 will describe the model in more detail.

With the domain drawn and the correct subdomain and boundary conditions assigned, the domain can be meshed. In this experiment, the current at the microdisc electrode is being monitored. The mesh elements do not need to be refined in the bulk as no chemistry occurs in the bulk therefore the mesh can be set to very coarse in this region. The first step is therefore to refine the mesh at the electrode boundary. In order to do this, the number of elements at this boundary is constrained. For an automatically generated mesh, there will only be one element along this boundary. The accuracy -or the relative difference between the simulated current and the theory -as a function of increasing number of constrained elements is shown in figure 2.2.

The accuracy increases rapidly as the number of constrained elements along the boundary increases. However, eventually, a plateau is reached around 3%.

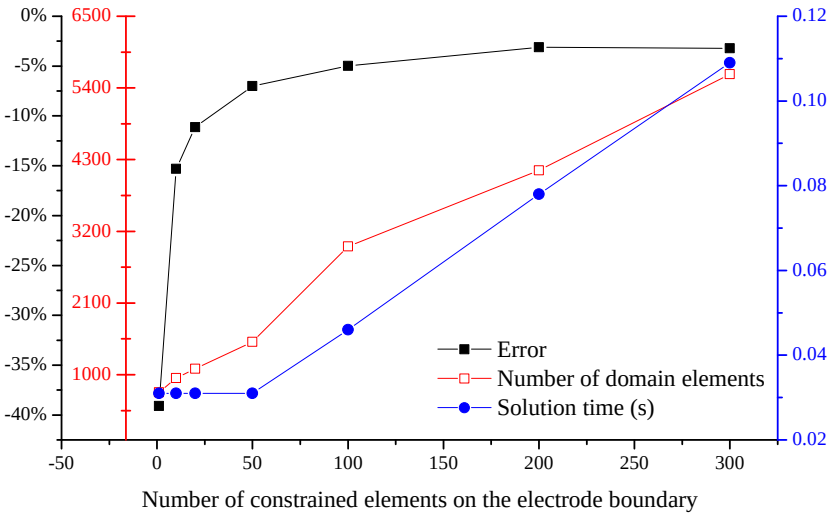

Figure 2.2: Accuracy, number of elements in the domain and solution time as a function of the number of constrained elements

When this occurs, further refinement of the mesh would not make the model any more accurate. The number of constrained elements on the electrode boundary is therefore fixed at 200.

It is common knowledge that edge effects are important with microdisc electrodes and therefore the next parameter to refine is the maximum element size at the electrode edge. With this step, an issue with meshing arose. As mentioned previously, this is a multiscale model with the radius of the electrode one thousand times smaller than the simulation domain. As a result, there is a very large increase in element size from the elements around the electrode to the elements in the bulk. This is represented in the element area ratio, which decreases with increasing number of constrained elements. This can be monitored when meshing a domain, as it appears that for element area ratios smaller than approximately 10^{-9}, the multiscale mesh begins to break down and the necessary refinement for a good accurate simulation cannot be performed. As a result, two subdomains were created in the existing domain using a meshing cylinder, as depicted in figure 2.3. This is essentially a method of dividing the overall domain into smaller sections to ensure the element area ratio is kept low, thus enabling a further refinement the mesh. The boundary condition applied to the meshing cylinder

boundaries is that the flux on one side of the boundary is equal to the flux on the other side.

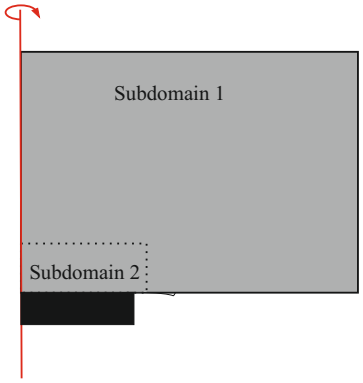

Figure 2.3: Schematic representation of the meshing cylinder used, in dotted lines, which divides the simulation domain (in grey) into two subdomains

Generally, only one meshing cylinder was used, although with some of the more complex 3D models, a second one was required. The exact size of this subdomain makes negligible difference. The advantage of dividing a domain is that different conditions such as growth rate can be assigned to the different subdomains and therefore a small growth rate near the electrode may be useful, whereas a bigger growth rate outside the reach of the diffusion layer would be acceptable, to ensure large elements are used, thus saving on computational effort. Figure 2.4 shows the change in accuracy as a function of the decreasing maximum element size.

Two meshing cylinders are compared: the first has a height of 0.5 and a radius 1.5, whereas the second is smaller with a height of 0.1 and radius 1.1; these are dimensionless quantities. Once again with this parameter, a plateau is reached and this the point where the mesh has been sufficiently refined. Note that there is negligible difference between the two meshing cylinder sizes. Refining these two parameters has given an accuracy within 0.1%, with a solution time still within 0.1 s.

The element growth rate in the meshing cylinder was investigated and shown to have no influence in this case. Secondly the exact size of the meshing cylinder was shown not to impact on the accuracy of the model.

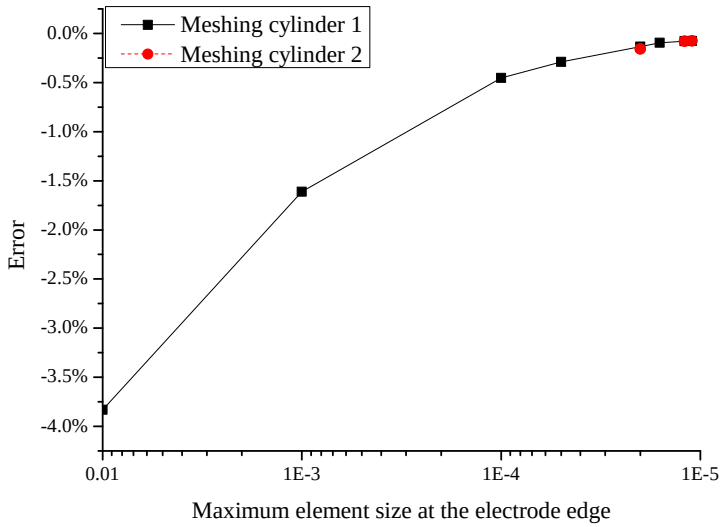

Figure 2.4: Accuracy of the simulation as a function of the maximum element size at the edge effect

2.4.2 Meshing procedure

The steps for meshing are therefore as follows:

- The simulation should be drawn and meshed using the automatic mesh generator. This may be refined once or twice depending on the size of the domain. A parameter should then be investigated, post processing, such as the concentration profile in the simulation domain, in the case of an electrode reaction as the ones studied in this project. This will reveal areas of change, and thus where the mesh will be required to be refined. In particular, the user should look out for boundary singularities such as edges of electrodes, and corners such as around the insulation sheath in SECM experiments. This step is particularly important if the user has no knowledge of the problem.

- Once the refinement requirements of the model have been established, the parameters of the mesh (maximum element size, minimum element size, element growth rate, number of constrained elements) for each part of the model (from subdomains to individual points) can be varied iteratively.

- The progress in the mesh should be studied by monitoring a value such as the current at the electrode. Even if there is no analytical solution to compare this with, the mesh can be refined by varying a specific item until a plateau is reached. The user may find that the monitored value does not vary when certain parameters are refined, which will happen if there is no chemistry occurring in that region.

- It may be necessary to split the simulation domain into smaller subdomains to enable the accuracy required to be reached. Generally, it was found that the size of the subdomain used did not influence the accuracy and that it simply was useful as a way of reducing the element area ratio thus enabling a further reduction of element size.

There are simple ways of knowing whether the mesh defined gives accurate result. The first is to slightly increase the size of the simulation domain. For example in our models, to ensure bulk conditions are reached, the radius of the domain will be a dimensionless value of 1000. Increasing this value to 1000.1 or reducing it to 999.9 and recalculating the current at the electrode to determine the relative difference is a method of testing the accuracy of the mesh. The values should be within 0.1% of each other. For the model presented above, these were within 0.01%.

Using the postprocessing abilities of the software would also be useful. Figure 2.5 shows concentration contour plots for the unrefined mesh on the left and a refined mesh on the right. What is instantly observable is the difference in the concentration layers between the two cases. Whilst this is noticeable here, without an accurate map to compare it with, it would be impossible to determine whether a contour map was correct or not. However the contour plot for the unrefined mesh is uneven, whereas the lines for the refined mesh are smooth. This is a clear indicator of a mesh which will not give accurate results. This is therefore a possible test.

When modelling several points of a similar model, such as with an approach curve or line scan, there is an easy way of spotting a inaccurate mesh: two cases are compared in figure 2.6, with a good mesh in (a), by which is meant an ac-

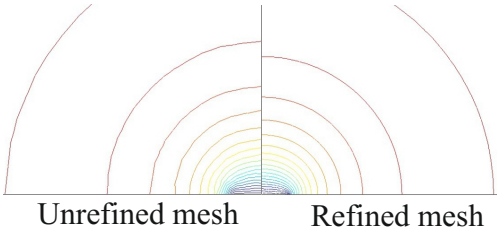

Figure 2.5: Concentration contour plot at a microdisc electrode for a unrefined mesh on the left, compared to a mesh that has been refined at the electrode boundary

curate mesh. Figure 2.6(b) shows the case where the mesh created is not refined enough. It can be observed that the line through the data points is not smooth: this is indicative of a mesh which will not give accurate results.

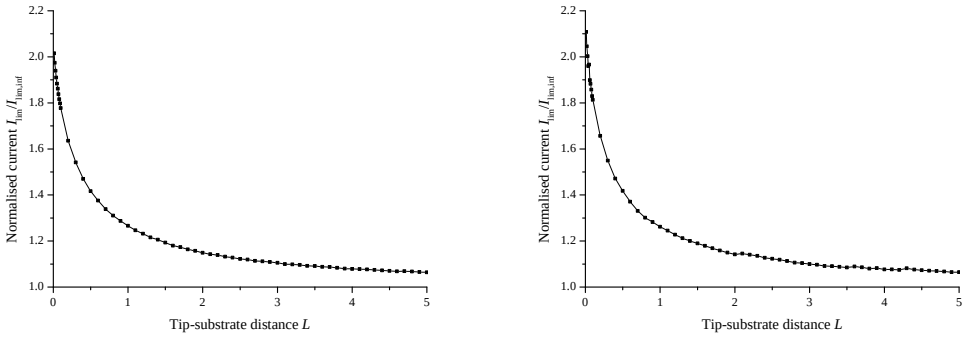

(a) Good mesh **(b)** Bad mesh

Figure 2.6: Comparison of the same positive feedback approach curve, for a cone with aspect ratio $H = 1$ and insulation sheath thickness $R_g = 1.1$ approaching a conducting island with radius $R_s = 100$, embedded in an insulating matrix for sufficiently refined

In this section, simple tools have been provided for users to refer to when meshing their own domain. Firstly, a procedure has been outlined. Moreover, easy tests are given to check the accuracy of the solution will be good.

Study of the electrochemical response of AFM-SECM probes with conical electrodes at the apex

Chapter 3

Bulk diffusion limiting currents at conical electrodes

3.1 Previous literature on cone-shaped electrodes

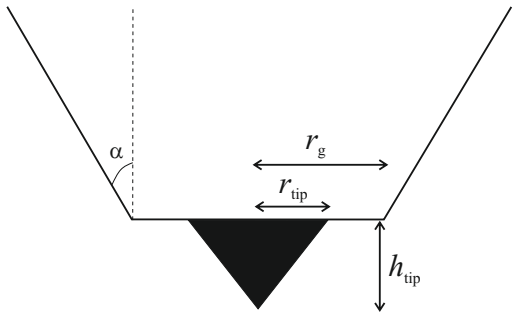

Figure 3.1: Schematic representation of the perfect tip with its describing parameters: r_{tip} the radius, h_{tip} the height, α the half angle and r_g the insulation sheath

The existing literature on conical electrodes is not extensive, as other geometries such as discs offer better SECM resolution as well as easier fabrication methods and have thus been more commonly used. In 1989, Penner *et al.*[131] described the fabrication and characterisation of conical microelectrodes: the etching of microwires, which are then coated to form the insulation sheath, surrounding the electrode. This produced conical tips with aspect ratios ranging from 0.5 to 10, which were shown to exhibit hemispherical diffusion. An early study of the conical shape was presented by Sokirko and Oldham in 1997:[132] a potential step experiment was investigated and the concentration profile was determined as a function of time. Diffusion to conical electrodes was also studied by Zoski and Mirkin,[35] who derived an expression to calculate the limiting current at a conical electrode with cylindrical insulation. Initially, transient simulations were performed for differ-

ent geometrical parameters. The influence of the insulation sheath thickness was evaluated, which revealed that, as with disc electrodes, current decreased with increasing R_g. Equation 3.1 was then fitted to the simulated normalised current $I_{lim,inf}$, which was accurate within 0.2%. This expression is a function of the normalised radius of insulation R_g as well as of four functions of the aspect ratio of the cone - or the ratio of the height of the cone over the radius of the cone which describes the sharpness of the electrode. A table of the values of the constants for the relevant aspect ratios is presented for users to refer to. Constants for intermediate aspect ratio values could then be interpolated. This will therefore take into account the geometry of the electrode. The dimensional current $i_{lim,inf}$ can then be determined by multiplying the calculated value $I_{lim,inf}$ by the number of transferred electrons n, Faraday's constant F, the diffusion coefficient D, the bulk concentration C^b and the radius of the electroactive cone r_{tip}, see equation 3.2.

$$I_{lim,inf} = A + B\,(R_g - C)^D \tag{3.1}$$

$$i_{lim,inf} = 4nFDc^b r_{tip} I_{lim,inf} \tag{3.2}$$

Later on, Shao and Mirkin[133] presented the fabrication of nanometer sized etched conical electrodes. Dickinson *et al.*[110] studied chronoamperometry and voltammetry at conical electrodes, using the finite difference method. The investigation focussed on the influence of the angle of the cone - or the aspect ratio - however did not take into consideration the influence of the insulation surrounding the conical electrode. The conclusion of the study was that 'tall' cones - or high aspect ratio conical electrodes - behave more like cylindrical electrodes, whereas low aspect ratio cones will be closer to disc electrodes. More recently a study of chronoamperometry at conical electrodes with conical insulation was presented[56] but with $r_g = r_{tip}$, i.e. there is no insulation plane surrounding the electroactive cone. Similar findings to Dickinson were presented: for aspect ratio H approaching 0, the behaviour is disk like, whereas higher aspect ratio larger than $H = 20$ will approach cylindrical electrode behaviour. An investigation into short times chronoamperometry revealed that dimensions of the cones could be extracted

from the exposed area, itself estimated using the current vs. time curve, although knowledge of the angle of the cone is required.

The first experiment performed with a newly fabricated tip is to generate a cyclic voltamogram for a well behaving redox couple such as ruthenium hexaamine (III/II), in order to determine the limiting current of the electrode in bulk solution. With this in mind, it was deemed to be interesting to begin the study with the derivation of an expression that would allow the user of such a tip to determine the theoretical value of the current, knowing its geometry. In the work presented here, bulk limiting currents are generated in order to determine the limiting current of conical electrodes with conical insulation.

3.2 Aim and details of the simulations

The aim of the work performed here is to use the modelling of diffusion to an electrode to determine the theoretical bulk limiting current at a conical electrode with conical insulation, as depicted in figure 3.1. By repeating this for several different geometries, we aim to fit an expression to the data to provide users of such conical electrodes with the tools to estimate the bulk limiting current. Secondly, the fabrication of these electrodes - described in the introduction - is not only a difficult process but also an expensive one. Defects will occur and it is important to know how these defects will affect the resolution of the electrode so that users can decide whether the tip must be discarded or not. The second aim of the work will therefore focus on the simulation of these defects and the quantification of their influence on the bulk limiting current.

The modelling presented here is used to derive an expression capable of calculating the limiting current of a conical electrode in the bulk, as a function of its geometry as shown in figure 3.1: the radius r_{tip} and height h_{tip} of the electroactive cone and the radius r_{g} of the insulation. This expression will be equivalent to $i_{\mathrm{lim,inf}} = 4nFDCa$, used to calculate the theoretical current of a disc electrode of radius a and infinite R_{g}.

The problem was cast into dimensionless form for the modelling, as shown in table 3.1. The three distances describing the tip geometry are now reduced to only two dimensionless parameters: $H = {}^{h_{\text{tip}}}/_{r_{\text{tip}}}$, the aspect ratio of the electrode, which describes how sharp the tip is, and $R_{\text{g}} = {}^{r_{\text{g}}}/_{r_{\text{tip}}}$, the dimensionless radius of insulation.

Table 3.1: Table of the parameters of the domain, along with the corresponding dimensionless quantity

Dimensionless parameter	**Dimensionless parameter**	**Description**
r	$R = {}^{r}/_{r_{\text{tip}}}$	Polar coordinate
z	$Z = {}^{z}/_{z_{\text{tip}}}$	Polar coordinate
r_{tip}	$R_{\text{tip}} = {}^{r_{\text{tip}}}/_{r_{\text{tip}}} = 1$	Radius of the electroactive cone
h_{tip}	$H = {}^{h_{\text{tip}}}/_{r_{\text{tip}}}$	Height of the electroactive cone with the dimensionless height also known as the aspect ratio, describing the sharpness of the cone
r_{g}	$R_{\text{g}} = {}^{r_{\text{g}}}/_{r_{\text{tip}}}$	Radius of the surrounding insulation sheath
l	$L = {}^{l}/_{r_{\text{tip}}}$	Tip-substrate distance
$c(r,z)$	$C(R,Z) = {}^{c(r,z)}/_{c^{\text{b}}}$	Concentration
i_{lim}	$I_{\text{lim}} = {}^{i_{\text{lim}}}/_{nFDc^{\text{b}}r_{\text{tip}}}$	Limiting current at the electrode
$i_{\text{lim,inf}}$	$I_{\text{lim,inf}} = {}^{i_{\text{lim,inf}}}/_{nFDc^{\text{b}}r_{\text{tip}}}$	Limiting current at the electrode in the bulk

The geometry of the cone is perfectly symmetrical (as we are considering the idealised case); moreover there is a need for a large number of simulations in order for the expression to be accurate: the modelling was therefore performed in the 2D axisymmetric mode. The schematic representation of the simulation domain is shown in figure 3.2.

The assumption is made that for a perfect tip, the angle α formed by the insulation sheath with the vertical is the same as the half angle of the electroactive cone, i.e. $\alpha = \tan({}^{1}/_{H})$, as the successive conducting and insulating layers deposited would be of the same thickness everywhere.

Diffusion controlled conditions are applied: convection is ignored and the assumption is made that an excess of background electrolyte is used, thus making

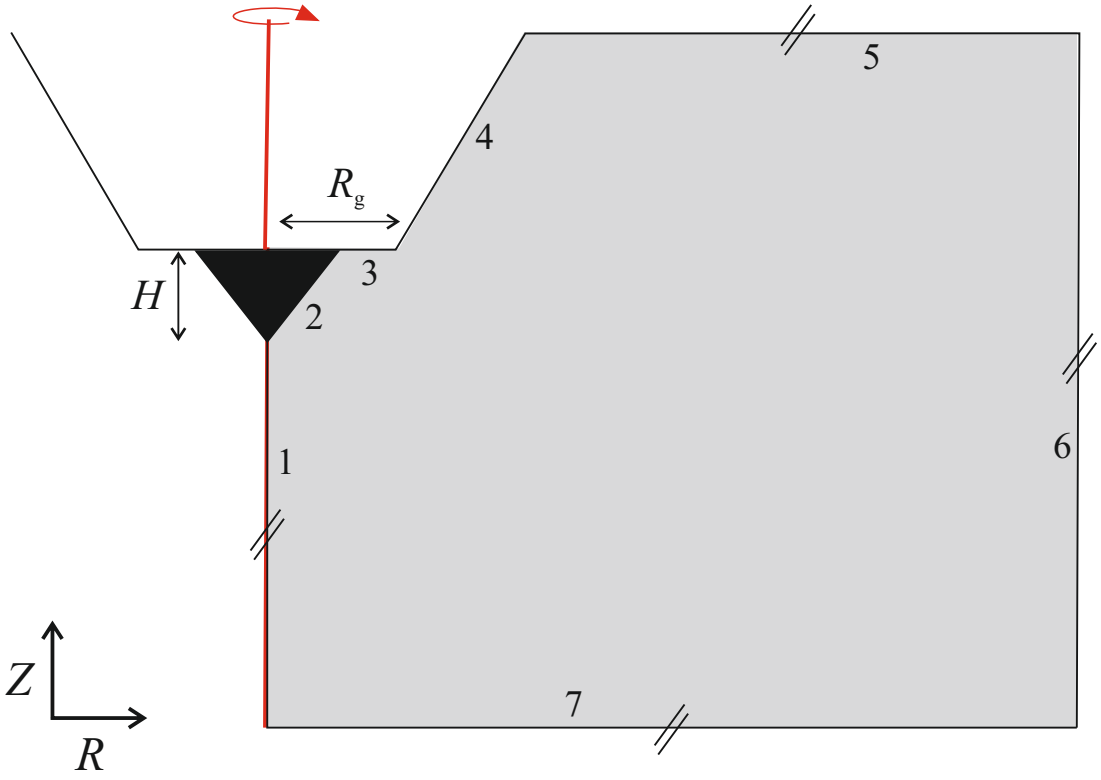

Figure 3.2: Simulation domain (in grey) for modelling of the conical electrodes in the bulk, in dimensionless units, with boundary numbering and the meshing cylinder in dashed lines. In red is the axis of symmetry. See table 3.2

migration of electroactive species negligible. The model is solved in the steady state; the equation to solve is therefore:

$$\frac{\partial^2 c}{\partial r^2} + \frac{1}{r}\frac{\partial c}{\partial r} + \frac{\partial^2 c}{\partial z^2} = 0 \tag{3.3}$$

The initial condition of the domain is dimensionless concentration C^{b} in the entire domain, to recreate the condition of a solution containing one species only, before potential is applied to the electrode. The assumption is made that the diffusion coefficients of both the oxidised and reduced species are equal, resulting in only one species needing to be considered in the simulations. This is a common assumption for redox couple with similar diffusion coefficients. In 1997, Martin *et al.*[134] set out to determine whether this was valid, by monitoring experimentally and theoretically the influence of the diffusion coefficient ratio $\gamma = {}^{D_{\mathrm{O}}}/_{D_{\mathrm{R}}}$ on the current transient at different tip-substrate distances, for a conducting substrate. These were shown to be sensitive to γ at short times but converge at steady state.

Table 3.2: Boundary conditions corresponding to the simulation model shown in figure 3.2 of the conical electrode with conical insulation in the bulk solution

Boundary number	Boundary description	Boundary condition
1	Axis of symmetry	$r = 0$
2	Electrode	$C = 0$
3,4	Insulation	No Flux
5,6,7	Bulk boundaries	$C = 1$

As the modelling done here is in the steady state, this is a safe assumption to make. This was confirmed more recently by Cornut, who showed that only one species had to be taken into account, as the concentration of the other could then easily be determined from the modelled species concentration.[135] The boundary conditions corresponding to the simulation domain shown in figure 3.2 are detailed in table 3.2. This model was meshed using the method described previously, in chapter 2. The mesh giving the best accuracy has a fixed number of elements constrained along the boundary of the electrode. The number of constrained elements was varied as a function of the aspect ratio: Element Number $= 100\sqrt{1+H^2}$, calculated for each separate model. The growth rate was set to 1.1, and the overall mesh to very coarse to ensure elements in the bulk are not unnecessarily small, which would be a waste of computational time and effort.

The dimensionless current was then calculated by integrating the flux over the area of the electrode:

$$I_{\text{lim,inf}} = 2\pi \int S \frac{\partial C}{\partial n} dS \tag{3.4}$$

where n is normal to the boundary and S the integration variable.

The accuracy of these simulations was tested by comparing a representative selection of cases to simulations with models solved using SAFE, see chapter 2. The cases chosen ranged in aspect ratio and insulation sheath thickness. This showed agreement within 1% and thus enabled simulations to be run with confidence in the validity of the results.

3.3 Influence of the geometrical parameters of the perfect tip on the bulk limiting current

Typical aspect ratios encountered experimentally with the type of commercially available tips and the fabrication method used will be in the range of $H = 1$ to $H = 5$. The radius of insulation will depend on the thickness of the insulation applied and the area revealed by the etching. To ensure the completeness of the study, a wide range of insulation sheath thicknesses was modelled: $R_g = 1.1$ to $R_g = 100$.

3.3.1 The insulation sheath thickness

The first geometrical parameter investigated was the insulation sheath thickness. The plot of the current as a function of the R_g is shown in figure 3.3, for varying electrode sharpness.

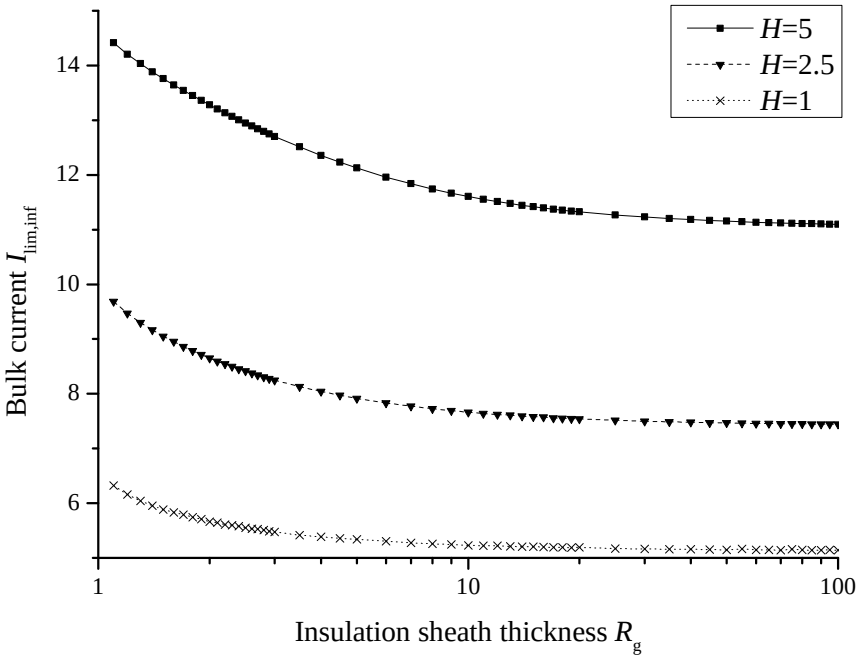

Figure 3.3: Dimensionless diffusion limited bulk current at the conical electrode plotted for three different aspect ratios H as a function of the insulation sheath thickness R_g

For very small R_g, there is a large amount of back diffusion, which results in a larger current. With increasing insulation sheath thickness, the current decreases

as there is increased hindrance which results in a spread of the diffusion layer. At small insulation sheath thickness, the drop is very fast; it then slows down with increasing R_g until eventually a plateau is reached. The insulation layer is then so thick that no back diffusion occurs around the edges of the surrounding sheath; an additional increase in thickness would make no difference to diffusion to the electrode. The current at such an electrode will approximate the current at an electrode with cylindrical insulation as the edges of the insulation sheath do not influence diffusion to the electrode due to the shielding by the insulation plane. The insulation sheath thickness for which the plateau is reached is larger for larger aspect ratio, due to the relative increased size of the diffusion layer compared to less sharp electrode. In fact for a small aspect ratio, such as $H = 1$, the thickness of insulation no longer has an influence from approximately $R_g = 20$, for which the current is within 1% of the plateau current, whereas for $H = 5$, the plateau is reached for $R_g = 30$. The area occupied by the diffusion sphere is much smaller for less protruding electrode and as the current will be unaffected by geometry outside this sphere, the more localised the diffusion layer, the smaller the insulation sheath radius for which the plateau is reached.

3.3.2 The aspect ratio

The effect of the aspect ratio on the limiting current at the electrode was then investigated by varying this for a fixed insulation sheath radius, and can be seen in figure 3.4. As expected, the current increases with increasing aspect ratio as the larger the aspect ratio, the larger the area of the electrode and thus the bigger the current.

There are clear trends in this plot, with an almost linear relationship between the current measured and the aspect ratio. In fact, the relationship is increasingly linear with increasing insulation sheath thickness. This can be explained by considering of the growth of the diffusion layer with increasing H for a large R_g: the shape is perfectly hemispherical and will therefore increase regularly with increasing electroactive area. However with smaller insulation sheath, back

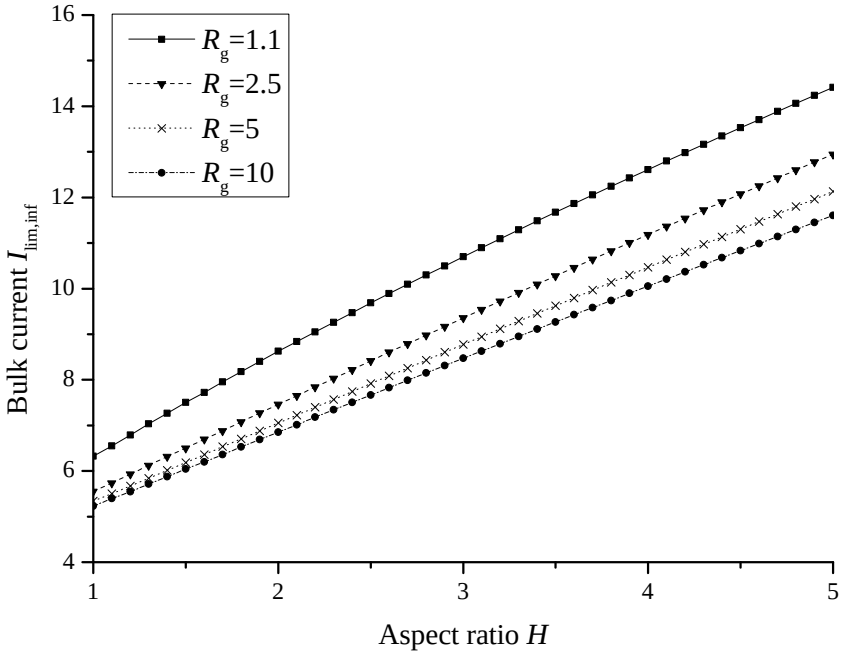

Figure 3.4: Dimensionless diffusion limited bulk current at the conical electrode as a function of the aspect ratio H for different insulation sheath radii R_g

diffusion occurs. This will cause the diffusion growth to not be perfectly regular, which is reflected in the current, although the distortion is very small.

The cases investigated here were intentionally focussed on the most likely geometries encountered for the AFM-SECM probes, i.e. $H = 1$ to $H = 5$. For an aspect ratio smaller than 1, the cone approaches a disc electrode. In fact, $H = 0$ equates to a disc electrode with infinite insulation. The curves for different insulation sheath thickness would therefore reach 4, the dimensionless limiting current at a disc electrode embedded in an infinite insulation plane, if extrapolated to $H = 0$.

3.3.3 Deriving an expression to calculate the bulk limiting current

An expression was fitted to over 2000 individual data points, all corresponding to a simulation for the individual couple (H,R_g). For each fixed aspect ratio H,

an expression was fitted:

$$I = A + B(R_g + C)^{-D} \tag{3.5}$$

This is very similar to the equation derived by Zoski and Mirkin for a conical electrode with cylindrical insulation.[35] Several other expressions were tested, none with as good a fit. The four constants A, B, C and D were then plotted as against the aspect ratio H, for each value of R_g, see figure 3.5. It was found that there was a simple first or second degree polynomial relationship between each constant and the aspect ratio, as seen in figure 3.5. We were thus able to derive expression 3.6, valid for $H = 1$ to $H = 5$ and $R_g = 1.1$ to $R_g = 100$.

$$\begin{aligned} i &= nFDcr_{tip}(A_H + B_H(R_g + C_H)^{-D_H}) \\ \text{with } &\begin{cases} A_H = 1.480H + 3.691 \\ B_H = 0.126H^2 + 0.659H - 0.013 \\ C_H = 0.012H^2 + 0.253H - 0.727 \\ D_H = -0.009H^2 + 0.082H + 0.830 \end{cases} \end{aligned} \tag{3.6}$$

where n is the number of electrons in the reaction, F is Faraday's constant, D is the diffusion coefficient, c^b the bulk concentration and r_{tip} is the radius at the base of the electroactive cone. This expression fits the simulated results within 0.93%, the maximum relative difference, and on average, the difference between simulation and the expression is 0.29%.

With respect to the disc electrode, inputting parameters $H = 0$ and R_g into equation 3.6 would give a dimensionless current of 3.69, i.e. a relative error of around 8%.

This expression will therfore be valid for H down to $H = 0$ within 8%. Larger values of H were not investigated. However, Zoski and Mirkin reported steady state limiting currents for conical electrodes with cylindrical insulation presenting parameters $H = 10$ and $R_g = 100$.[35] For such a large insulation sheath thickness, the shape of the insulation sheath (cylindrical for Zoski *et al.* and conical for us) is irrelevant as no back diffusion around the edges of the sheath will occur.

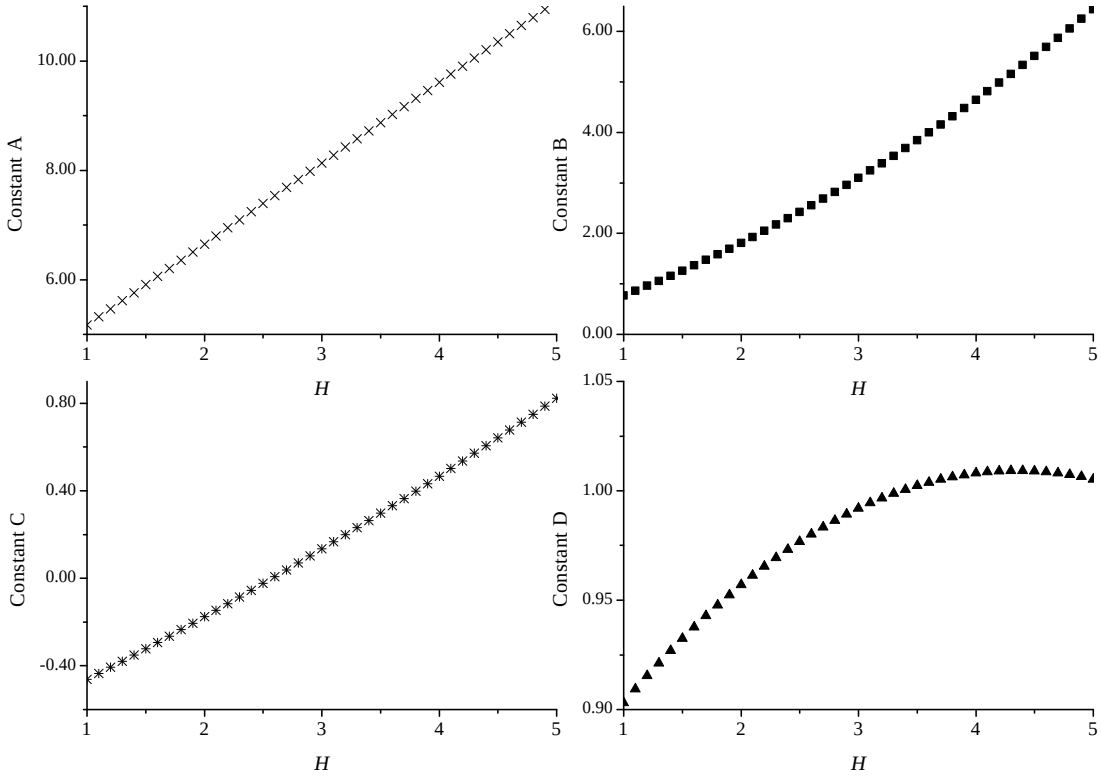

Figure 3.5: The constants of equation 3.6 plotted against the aspect ratios H

The current presented in their publication can therefore be compared to the current calculated using our equation; the relative difference is around 6.5%. The equation presented above can therefore be applied to a wider range of aspect ratios but a larger error will ensue. Note that for small aspect ratios, there is larger difference between our case and the geometry presented by Zoski and Mirkin. This will be discussed further in the next section, which focusses on defects that might occur.

Expression 3.6 is therefore able to determine the diffusion controlled current at a conical electrode with conical insulation, for a range of aspect ratios and insulation sheath thicknesses. The number of decimal points of the expression shown above is necessary to achieve a fitting within 1%, although reducing the number of decimal places to 2 will result to a fitting within 2%. Attempts were made to fit other expressions to this; however none of them were as accurate as the one derived above.

The disadvantage here is that this calculation cannot be reversed. By this we mean that using the experimental current measured will not be sufficient to

determine the geometrical parameters of the cones. It is only possible to use the geometry of the tip measured from an SEM image and then estimate the limiting current from this. This restriction is due to the fact that there are too many factors to take into consideration, as with the disc electrode (radius and insulation sheath radius). With the electrode radius r_{tip} known, it would however be possible to determine if a certain tip had a high aspect ratio: a dimensionless current larger than $I_{\text{lim}}/nFDc^{\text{b}}r_{\text{tip}} = 10$ will result from an aspect ratio larger than $H = 3$. Knowledge of the etching time and resulting exposed region will give an indication of the R_{g}, with the insulation layer thickness known. The SEM step is however part of the fabrication process and will enable for an accurate measurement of the aspect ratio H and insulation sheath R_{g}. However, even with these indications, it is impossible to determine if any defects would have an influence on the calculated current.

This is unfortunately a problem with the difficult fabrication method to make these fragile tips, see chapter 1 for details of the fabrication: defects will occur. The following part of the study concentrates on the influence of these defects, with typical ones being modelled.

3.4 Influence of defects on the bulk limiting current

As mentioned above, the likelihood of a defect occurring during the difficult fabrication process is high and therefore it was an important part of the study to take this into consideration. Typical defects were therefore modelled and their influence determined. As the amperometric response is assumed to have a reproducibility no better than 5%, the change in current will be compared to this threshold.

3.4.1 Tip bluntness

A blunt tip is unavoidable as it is impossible for the conical electrode to be perfectly conical and this defect depends on the bluntness of the commercially

available tip purchased. These probes come with a given range of apex radius, generally guaranteed within a range of 7 to 12 nm, if insulating. However adding a layer of conducting material to this will increase the apex radius. Other problems occur when looking at specific materials: for e.g. eventually the aim is to produce electroactive tips made of boron doped diamond, which has been found to form clusters at the tip apex. The study here was restricted to a general idealised case, simply as there are too many cases to take into consideration and the aim of this research is to gain an insight into the influence of defects, not model every possible case imaginable. The schematic representation of this defect is shown in figure 3.6.

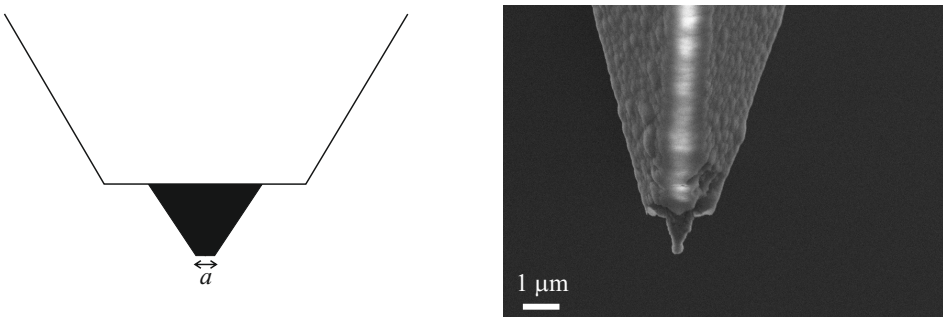

(a) Schematic representation **(b)** Real tip

Figure 3.6: Defective conical tip with blunt apex, represented schematically in (a) with its parameter a, the apex radius, and illustrated with a real example in (b), a boron doped diamond electrode with silicon nitride insulation layer

With this in mind, 2D axi-symmetric simulations were run, once again relying on the symmetry of the domain considered to save on computational time and effort. The apex radius of the tip was fixed at $a = 10$ nm. The radius of the exposed conducting area was then varied from $r_{\text{tip}} = 20$ nm to 1 μm, the highest radius that is considered suitable for the AFM-SECM tips fabricated in this project. The only geometrical factor considered here was the aspect ratio H, for which three representative values were taken: $H = 1$, $H = 2.5$ and $H = 5$. The thickness of the surrounding insulation was not deemed to be a factor that would affect the current largely in this case and was therefore fixed at $R_{\text{g}} = 100$. The table of results is presented in table 3.3.

As expected, the results show that the larger the electroactive area, the smaller the influence of the tip apex. In fact for tips with a radius larger than 600

Table 3.3: Summary of the relative difference between the current at a blunt tip, described by the blunt apex radius a, and that at a perfect tip for different aspect ratio H and electroactive cone radius r_{tip}

r_{tip} **range**	$H = 1$	$H = 2.5$	$H = 5$
600 nm $\leq r_{\text{tip}} \leq$ 1 μm	$< 1\%$	$< 1\%$	$< 1\%$
100 nm $\leq r_{\text{tip}} \leq$ 600 nm	$< 4\%$	$< 5\%$	$< 6\%$
60 nm $\leq r_{\text{tip}} \leq$ 100 nm	$< 8\%$	$< 9\%$	$< 9\%$
20 nm $\leq r_{\text{tip}} \leq$ 1 μm	$< 21\%$	$<25\%$	$< 25\%$

nm, the difference between the perfect tip and the blunt tip is within 1%. The increase is also within experimental error for radii over 100 nm. It is also worth noting that the increase in current due to the tip bluntness is more important for smaller aspect ratios. This is due to the relative decrease in area being larger for larger aspect ratios. Note that there is a decrease in area which seems like a contradiction when the current is observed to increase. However part of the defective tip is a disc, which has higher current density than a conical vertex, hence the overall increase in current calculated. In conclusion, users need to be aware that this defect need only be considered important if using a tip with a radius smaller than 100 nm.

3.4.2 Insulation joining angle

A defect that has been observed with tips fabricated not only by our group but also by other groups[98] is a difference in insulation joining angle, seen in figure 3.7. For a larger than perfect insulation angle, the insulation forms a mound around the exposed tip, thus reducing the area of conducting material. A smaller angle will lead to a crater shaped insulation surrounding the electrode and a subsequent larger than expected electrode area. This is the first defect to be modelled in 3D in order to learn how to model and mesh accurately in 3D with a model that could be compared to 2D axisymmetric simulations in COMSOL and SAFE. The computing time and effort is greatly increased when going from 2D to 3D, due to the mesh being much larger and much more complex. The simulations were once again performed for a typical aspect ratio $H = 1.5$ and the insulation joining angle was varied from $\alpha = 40°$ to $\alpha = 140°$, for $\gamma_{\text{perfect}} = 123.7°$.

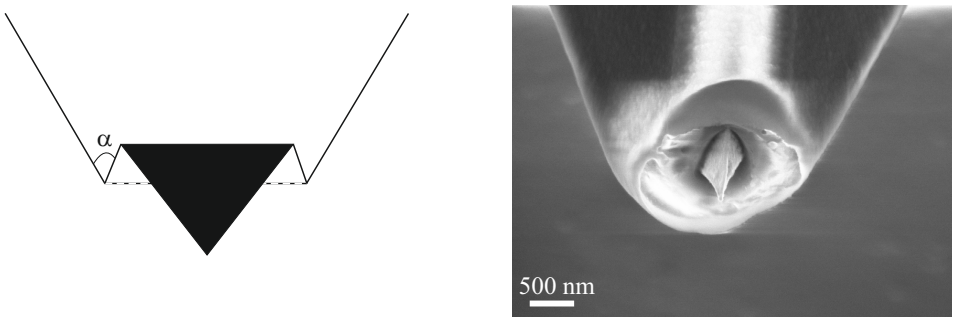

(a) Schematic representation **(b)** Real tip

Figure 3.7: Defective conical tip with imperfect insulation joining angle, represented schematically in (a) with its parameter α, the apex radius, and illustrated with a real gold tip with silicon nitride insulation in (b). The insulation sheath thickness and electrode radius should be determined as if the tip were perfect, i.e. following the dashed lines.

The insulation sheath thickness was varied from a minimum of R_g=1.1 to R_g=10 and the relative difference between the defective case and the perfect case is plotted in figure 3.8. This revealed the considerable influence of the defect on the measured current, due to the large change in exposed area. For a defective angle smaller than the perfect angle, the current will be larger due to the increase in electrode area. However the crater-like insulation will partly hinder diffusion to the electrode, as a function of both the defect angle and the insulation sheath thickness. The current at the defective tip would therefore be smaller than for a perfect tip of the same exposed area size. In contrast, a larger defect angle will lead to a reduced current. In practice, the estimation of the current should be done for a perfect tip, then taking into account the relative difference as defined by the plot in figure 3.8 to correct the calculated value.

However in some cases, such as when there is little difference between the perfect insulation joining angle and the insulation joining angle of the defect, it may be appropriate to use expression 3.6 to calculate the current for the actual level of exposed area, with the assumption that the shape formed by the insulation would not differ much from the perfect tip current, as opposed to assuming the exposed area as if the insulation were perfect. This is because if the insulation joining angle does not differ much from the perfect angle or if the insulation sheath thickness is small, insulation will not hinder diffusion for a crater-like sheath, or increase back diffusion for mound-like insulation, more than within

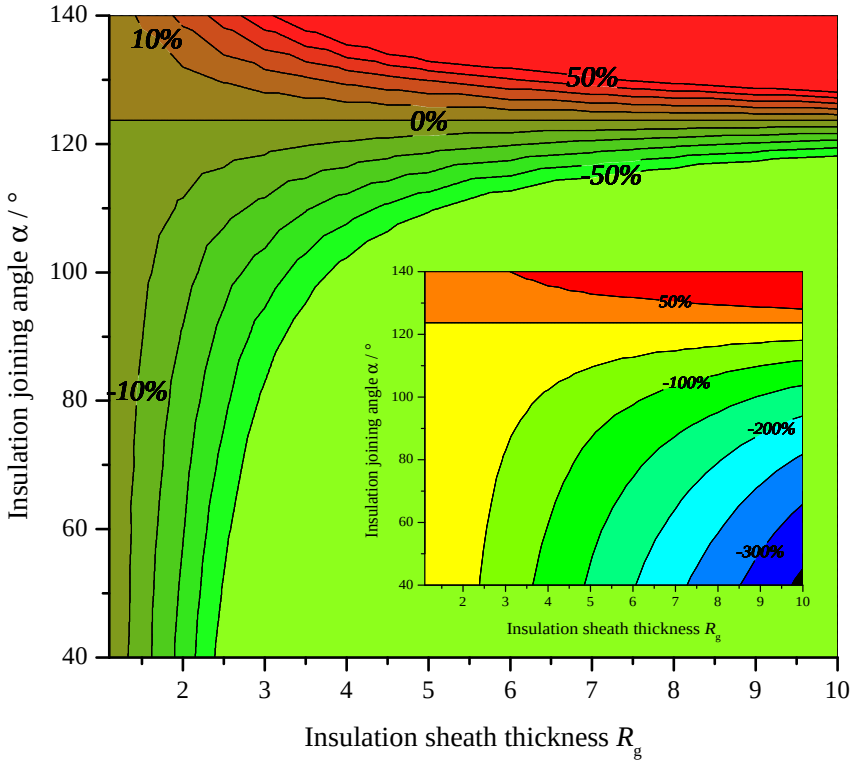

Figure 3.8: Plot of the relative difference between the current at a defective tip with angle α and the perfect tip current for a range of insulation sheath thickness and a fixed aspect ratio $H = 1.5$, with inset the same data with different scale

the experimental error. This study reveals that even the smallest change in insulation joining angle will result in a large change in current and this defect is expected to severely affect the sensitivity of the tip when performing scanning experiments.

3.4.3 Insulation angle

With the perfect case considered above, the half angle of the insulation is the same as the half angle of the conical electrode. However this is not always the case. The half angle of the cone is not the same throughout the probe: in fact, the apex is often slightly sharper than the remainder of the tip. The next defect to be modelled was therefore the case where the insulation angle differed to the cone angle, as depicted in figure 3.9.

The insulation angle, known as β, was varied from 0° to 90° for a tip with aspect ratio $H = 1.5$, which has a perfect insulation angle of $\beta_{\text{perfect}} = atan(1/H) = 33.7°$. For $\beta = 0°$, the insulation sheath is cylindrical, whereas for $\beta = 90°$, the in-

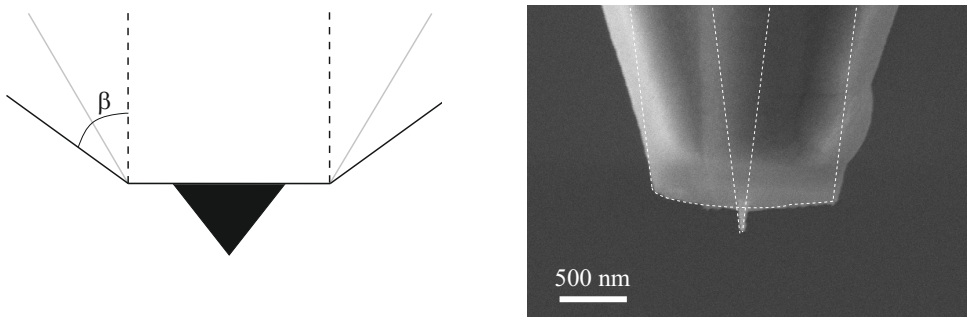

(a) Schematic representation **(b)** Real tip

Figure 3.9: Schematic representation of the defective tip with insulation angle differing from the perfect case in (a) with an example in (b), SEM of a gold tip with silicon nitride insulation, with the dashed white lines representing the perfect case

sulation plane is infinite. The dependence of the limiting current on the insulation angle β and the insulation sheath thickness is shown in figure 3.10.

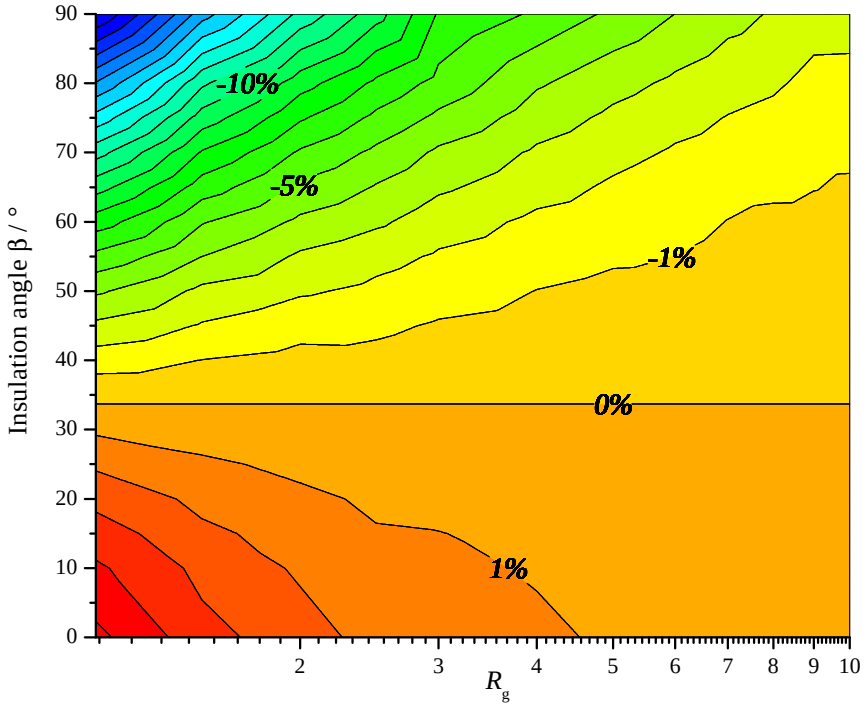

Figure 3.10: Relative difference (%) between the current at the defective electrode with insulation angle β and the current at a perfect electrode (for which $\beta = 33.7°$) as a function of the insulation sheath radius R_g, plotted on a log scale

The relative difference between the current at the defective tip and the current at the perfect tip decreases with increasing the insulation sheath radius R_g. The insulation angle β has very little influence for large insulation planes as there is little to no back diffusion. The plot of the relative difference reveals that a lower

current is to be expected for larger insulation angles. This is due to the diffusion layer being more spread out. However, a smaller insulation angle will lead to a decrease in hindrance and thus a larger current. Although the plot clearly indicates that a relative difference of up to 20% can be expected with defect, this is not likely to occur: in fact, for the angles most likely to be encountered in AFM-SECM, the change will be within 6% of the perfect tip current. This defect can therefore be ignored.

3.4.4 Off-centred tip

A defect, which can result from most fabrication methods, is the displacement of the tip, with the electrode not being perfectly centred within the insulation plane. Simulations were run in 3D as this is an unsymmetrical system. Two aspect ratios were investigated $H = 1.5$ and $H = 2.5$ for which the insulation sheath radius was varied from $R_g = 1.1$ to $R_g = 10$. This problem was modelled by displacing the electrode in one direction by a dimensionless distance ranging from 0.1 to 8. The steady state limiting current was calculated for each case and compared to the perfect case to determine the relative difference. The largest variation was calculated to be 4.2%, which is within typical experimental error. Two phenomena occur at the same time with this defect: as the tip moves away from the edge of the insulation sheath on one side, diffusion to the tip is increasingly spread out thus reducing the current. However, the insulation will the smaller on the other side and back diffusion will increase. The combination of the two opposing

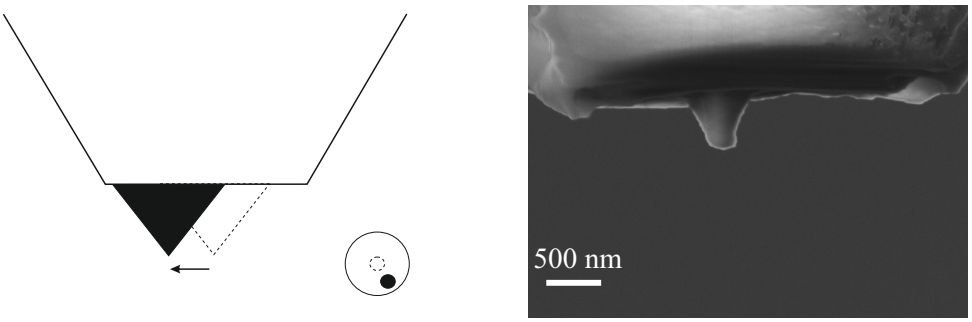

(a) Schematic representation **(b)** Real tip

Figure 3.11: Schematic representation of the defective tip with off centred protruding electroactive cone in (a) with a real example in (b) of a platinum conical electrode with silicon nitride insulation

effects results in an overall loss in current, with the shielding of diffusion dominating increased diffusion to the tip from the other side. A worst-case scenario was modelled to quantify its influence: for this case with the conical electrode was as far from the ideal case as possible for an insulation sheath thickness $R_g = 10$. The current for this probe was calculated to be 7.8% smaller than the perfect case. This defect is therefore not severe and can in fact be ignored as even for the worst case scenario, the difference is barely exceeds the experimental error.

3.4.5 Gap between the insulating and the electrode

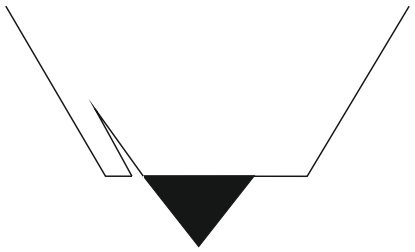

Figure 3.12: Schematic representation of the defective tip with a gap between the electroactive cone and the surrounding insulation

A common defect that can occur with the fabrication method used here is the presence of a small gap between the insulation and the electrode, increasing the exposed area, as depicted in figure 3.12. This may be due to the insulation not adhering to the conducting area, and peeling off. Simulations were run for H=1.5 and R_g=5. The defect was characterised by the width of the gap at the insulation plane and the angle with the vertical formed by the fissure is 5° smaller than the half angle of the cone, resulting in a thin crack along the electroactive cone, an idealised model of the defect as obviously too many cases could be considered and it is impossible to know exactly what is happening inside the gap. The dimensionless defect width initially studied was 0.5, half the radius of the conical electrode r_{tip}. Three different cases were then studied, as depicted in figure 3.13: the insulation gap around the entire electrode, half the electrode and a quarter of the electrode, for completeness of the study. The first case, where the gap is present all around the cone, resulted in an increase in current of 10.2%, whereas for the gap surrounding half the electrode, the current was 5.6% higher than the perfect tip current. Finally the case of the gap around only a quarter of the electrode was shown to result in a current increased by only 3% in comparison with the perfect tip. The small increase in current can be explained by looking at this concentration profile: the increase in

exposed area should result in a large increase in current, as observed with the insulation joining angle. However, as the fissure is small, species do not readily diffuse through it; only towards the mouth of the gap does diffusion occur, with the insulation blocking diffusion from occurring inside the gap.

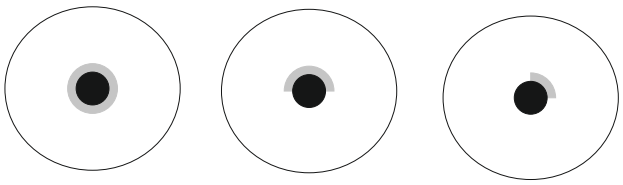

Figure 3.13: Top view of the defective conical tip, with in black the electroactive region and in grey the extent of the defect surround the electrode, as considered in the modelling: from left to right, all around the electrode, half the electrode and a quarter

Smaller sized gaps were then investigated for a gap surrounding the entire electrode: a dimensionless gap width of 0.2 was set, and the current was calculated to be 3.6% larger than the perfect tip current. Finally, the same problem was modelled for a defect width of 0.1, ten times smaller than the electrode radius. For this case, the current calculated was 1.9% higher than the perfect tip current, which is well within experimental error. In conclusion, small gaps in the insulation do not have a large influence: the gaps are too small for diffusion to spread through the fissure and can thus be ignored. For larger gap widths, the tip geometry will get closer to the crater-like insulation studied in a previous section. Fissures smaller than half the radius of the electrode will not affect the current above experimental error and the tip can still be used without fear of the resolution being affected.

3.4.6 Uneven insulation

Another defect than can occur during the fabrication method is uneven insulation around the cone. This defect, represented in figure 3.14, was investigated for $H = 1.5$ and $R_g = 5$, and is characterised by the dimensionless height difference H_{defect} between the two levels of the insulation sheath. As with other examples, this study does not claim to be the most experimentally realistic as the model is obviously idealised. However, the aim is to give users an order of magnitude of the effect of the defect on the limiting current.

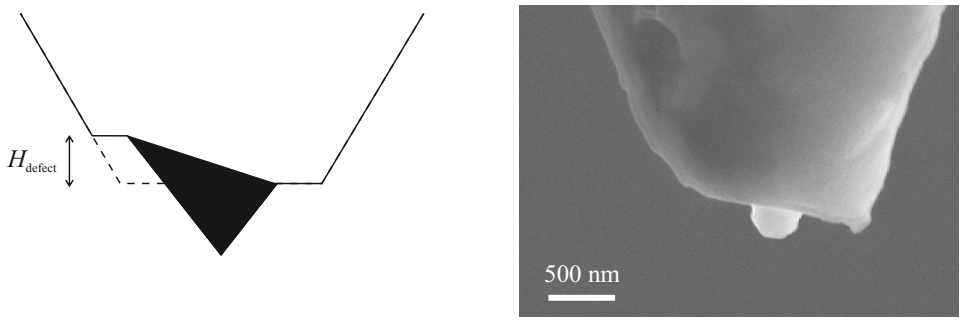

(a) Schematic representation **(b)** Real tip

Figure 3.14: Schematic representation of the defective tip with uneven insulation in (a) with a real tip example in (b), a boron doped diamond tip with surrounding silicon nitride insulation

Due to the complexity of the geometry and the number of mesh elements, approximately 250 000, each individual simulation took between one and two hours to solve. This was done for dimensionless height $H_{\text{defect}} = {}^{h_{\text{defect}}}/_{r_{\text{tip}}}$ ranging from 0.1 to 5 and the results can be seen in figure 3.15.

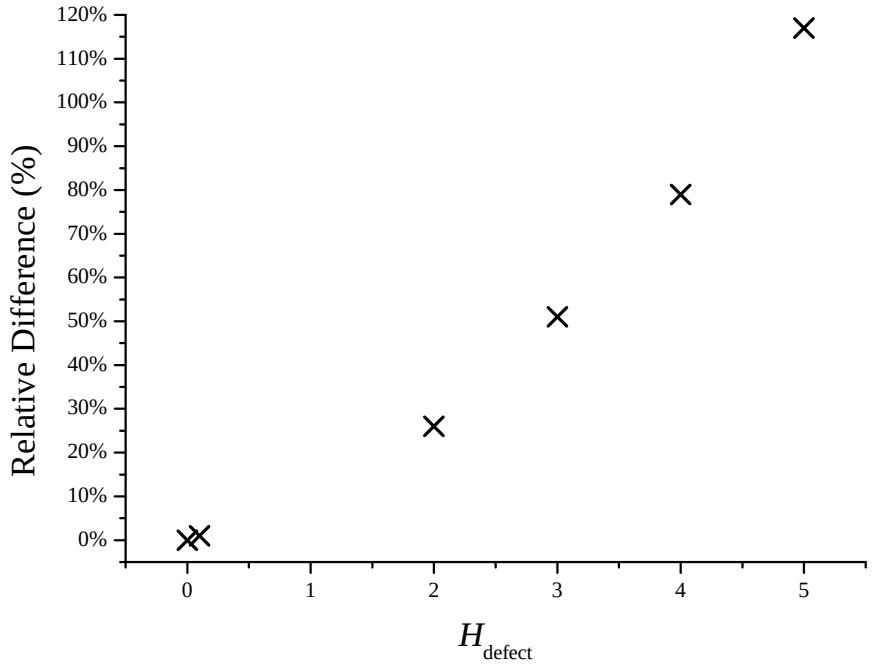

Figure 3.15: Plot of the relative difference between the current at the defective tip and the perfect tip current, as a function of the dimensionless defect height H_{defect}. This value ranges from 0, for which the tip is perfect to 5.

A defect of height $H_{\text{defect}} = 2$, i.e. twice the radius of the electroactive cone, will result in a limiting current 25% bigger than at the perfect tip current. The

maximum defect height modelled was H_{defect}=5, the limiting current of an electrode with this defect was calculated to be twice the limiting current of the perfect tip. As shown by the plot in figure 3.15, the limiting current increases rapidly with increasing H_{defect}, which is due to the change in exposed area. As H_{defect} increases, the base radius of the exposed cone increases; this explain the almost exponential increase in current - if the electrode were cylindrical, the increase in current would be linear. Both typical and extreme cases were modelled here. The defect height would be expected to be smaller than the diameter of the base of the cone, which resulted in an increase of less than 25% compared to the perfect tip current. Any higher defect size would result in a big loss in resolution, and the tip would not be usable.

3.4.7 Crack in insulation

The following part of the investigation into the behaviour of defective tips in the bulk concentrated on the insulation containing a crack in the insulation as observed in figure 3.16(b) and represented in 3.16(a). This defect is characterised by the dimensionless height of the defect H_{defect} and the width of the gap.

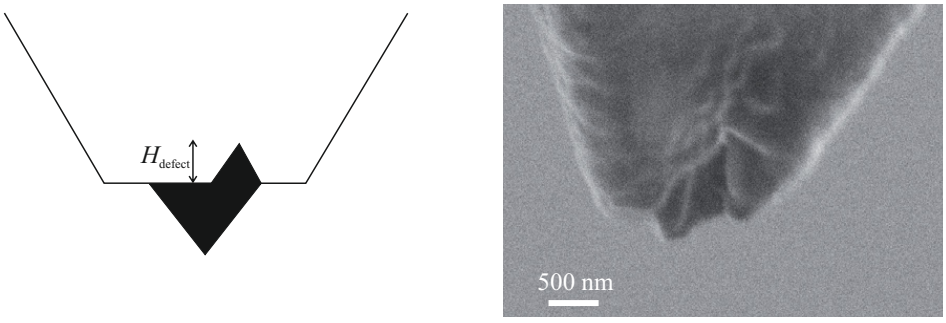

(a) Schematic representation **(b)** Real tip

Figure 3.16: Defective conical tip with cracked insulation sheath in (a) described by the crack height H_{defect}, and illustrated with a real example in (b) a gold electrode with silicon nitride insulation

Three different cases were simulated: $H_{\text{defect}} = 1$, 2 and 5 and the dimensionless current I_{tip} calculated for all three cases. The first case, where the defect height is the same as the radius of the conical electrode, resulted in an increase of current of 12.5%. The maximum defect resulted in an increase in current of 40.5%. There is an increased exposed area and diffusion occurs through the crack,

resulting in an increase of current of 21.3%. Unlike the example with the gap in the insulation, diffusion to the extra exposed area is not blocked; hence the large increase in current. This defect is therefore expected to greatly affect the resolution of the tip.

3.4.8 Insulation side walls

A step of the fabrication method consists of coating the insulation layer with a sacrificial layer of Chromium before etching the insulation. A possible defect resulting from this method is some insulation being unevenly etched and forming side walls surrounding the cone as seen in figure 3.17.

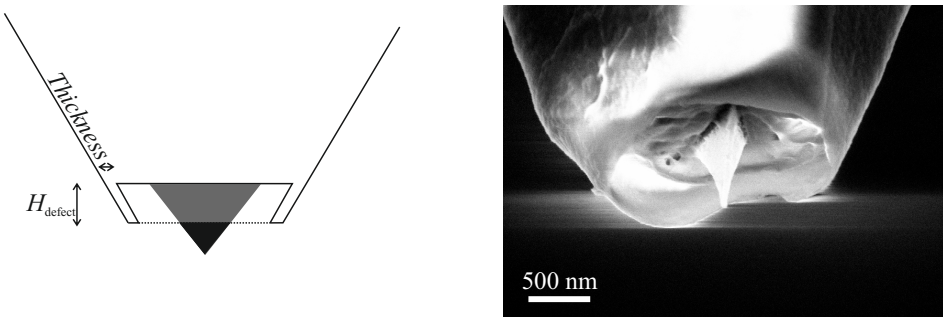

(a) Schematic representation **(b)** Real tip

Figure 3.17: Defective conical tip with side walls , characterised by the dimensionles defect height H_{defect} and the thickness of the wall, represented in (a) and illustrated with a real example in (b), a gold tip with silicon nitride insulation

This will block diffusion towards the electrode and is thus expected to affect the current measured at the probe. The influence of this defect was therefore studied by reproducing the tip for which the defect was observed in exact dimensions. The thickness of the wall was calculated to be $W_{\text{defect}} = 0.16$ and the height $H_{\text{defect}} = 1.09$. For this defect, the current at a defective electrode was found to be less than 1% smaller compared to the perfect tip current. This is well within experimental error and can therefore be ignored. To investigate the influence of this defect further, the same electrode was modelled with a wall thickness and height twice the value previously simulated (i.e. $W_{\text{defect}} = 0.32$ and $H_{\text{defect}} = 2.18$). A relative difference of -3% was calculated this case, which once again was well within experimental error. The concentration profiles for both defective tips cases mentioned are shown in figure 3.18.

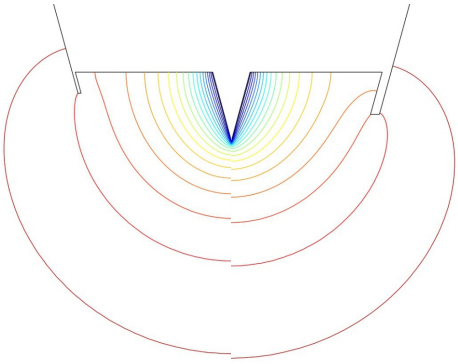

Figure 3.18: Concentration profiles for the each tip replica on the left hand side, compared to the case of an exaggerated defect, with in blue zero concentration of the species reacting at the electrode and in red bulk concentration

It is observed that the concentration profiles do not differ greatly and in fact there is not a large increase in hindrance with the defect being twice as prominent. The conclusion to this study is that users can use tips with existing side walls, safe in the knowledge that the current is only slightly decreased by the defect. The insulation sheath thickness here is $R_g = 8.27$. Users should note that a thick insulation wall for a tip with a small R_g would have a larger influence on the current due to increased hindrance.

3.4.9 The AFM cantilever

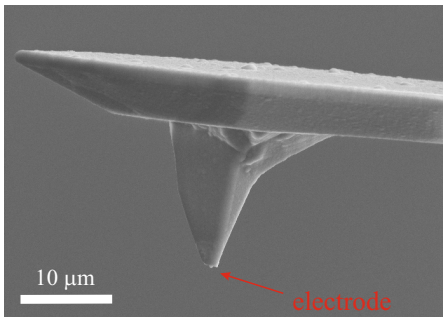

Figure 3.19: SEM of an AFM-SECM cantilever

It is worth pointing out at this point that the modelling performed here is simply for conical electrodes with conical insulation, not taking into consideration that these electrodes are found at the end of a cantilever. This section focusses on the cantilever and determining whether it will affect diffusion to the electroactive cone. The effect of these cantilever therefore had to be taken into consideration in this study. Two types of cantilevers were investigated: the first is the cantilever with a cone height of 12 μm, $H = 1.5$, seen in figure 3.19. The cantilever has a width of 50 μm and a thickness of 2 μm.

Table 3.4: Influence of the cantilever on the limiting current at the electrode, found at the end of the cantilever, compared to the theoretical perfect electrode case

r_{tip} **range**	**Cantilever 1**	**Cantilever 2**
1 μm to 500 nm	-0.7%	-1.1%
500 nm to 10 nm	-0.1%	-0.4%

The second cantilever studied had a pyramidal tip of height 3.3 μm and cantilever thickness 0.7 μm.

The cantilever is expected to spread the diffusion, resulting in a smaller current at the electrode and a loss of electrochemical resolution. As we are working with AFM, the electroactive tip will be very small. To quantify the effect of the cantilever, the smallest insulation thickness is considered ($R_g = 1.1$), as this will have the most back diffusion and will therefore be the most affected. A range of values of r_{tip} were modelled: from 1 μm to 0.05 μm and the maximum relative difference in the current with and without cantilever shown in table 2.

It was shown that there is negligible effect with all these tips and that for the range more likely to be considered in AFM-SECM ($r_{tip} < 1\mu$m), the maximum diffusion perturbation resulted in a 0.7% decrease in current compared to the perfect tip case. For the second cantilever, the maximum difference was calculated to be 1.1%. Users can therefore consider that the cantilever does not affect diffusion to the electroactive tip with r_{tip} smaller than 200 nm, as the relative difference compared to a tip without cantilever is smaller than 0.1%. This study, which reveals that the cantilever has negligible influence for the range of tip sizes considered in AFM-SECM, concentrated on the effect of the cantilever in the bulk; however the influence of this parameter will increase with decreasing tip to substrate distance as the substrate will spread the diffusion layer and increase back diffusion.

3.5 Conclusion

An expression was derived to calculate the current at a conical electrode with conical insulation, from thousands of steady state simulations modelling diffusion to a range of tip geometries. This expression is valid for aspect ratios $H = 1$ to

$H = 5$ and $R_g = 1.1$ to $R_g = 100$ and is accurate within 1%. Previously reported expressions do not cater for the shape of the insulation of our tips. Moreover these expressions are only valid for discrete values of aspect ratio H, whereas the expression developed in this work does.

The study of the influence of aspect ratio on the current revealed that higher aspect ratios result in larger currents, due to the increase in electroactive area. Secondly, large insulation sheath thicknesses were shown to decrease the current. Defects in insulation and changes in tip geometry were then modelled to provide users with a quantitative index of the influence of these defects. This aimed not only to give an indication as to how this would affect the current but also to give users an easy way of calculating the current at the probe taking into account the influence of defects. This can be done by following these steps:

- Determine the tip parameters, namely r_{tip}, h_{tip} and r_g, as if the tip were perfect
- Use expression 3.4 to calculate $I_{lim,inf}^{perfect}$, the perfect tip current in the bulk
- Determine the defect(s) present. Establish whether they are negligible (insulation angle, small gaps in insulation, off centred tip) or important (cracks in insulation, crater like insulation). Quantify the influence Φ_{defect} of the major defects (if any) using the guide presented in this chapter, such as the percentage by which the current is increased.
- Finally calculate the defective current: $I_{lim,inf}^{defect} = \Phi_{defect} I_{lim,inf}^{perfect}$.

This will give a more accurate estimation of the current in the bulk solution. A summary of the defects investigated in this study are shown in figure 3.20, classified in order of importance.

Note that the influence of defects is considered with respect to the bulk limiting current, where diffusion to the electrode is unperturbed. When considering the influence of defects close to a surface, as will occur in SECM, some defects which presented negligible influence in the bulk will have a larger influence at short tip-substrate distance. This has been shown for the off centred tip in the case of disc electrodes.[41]

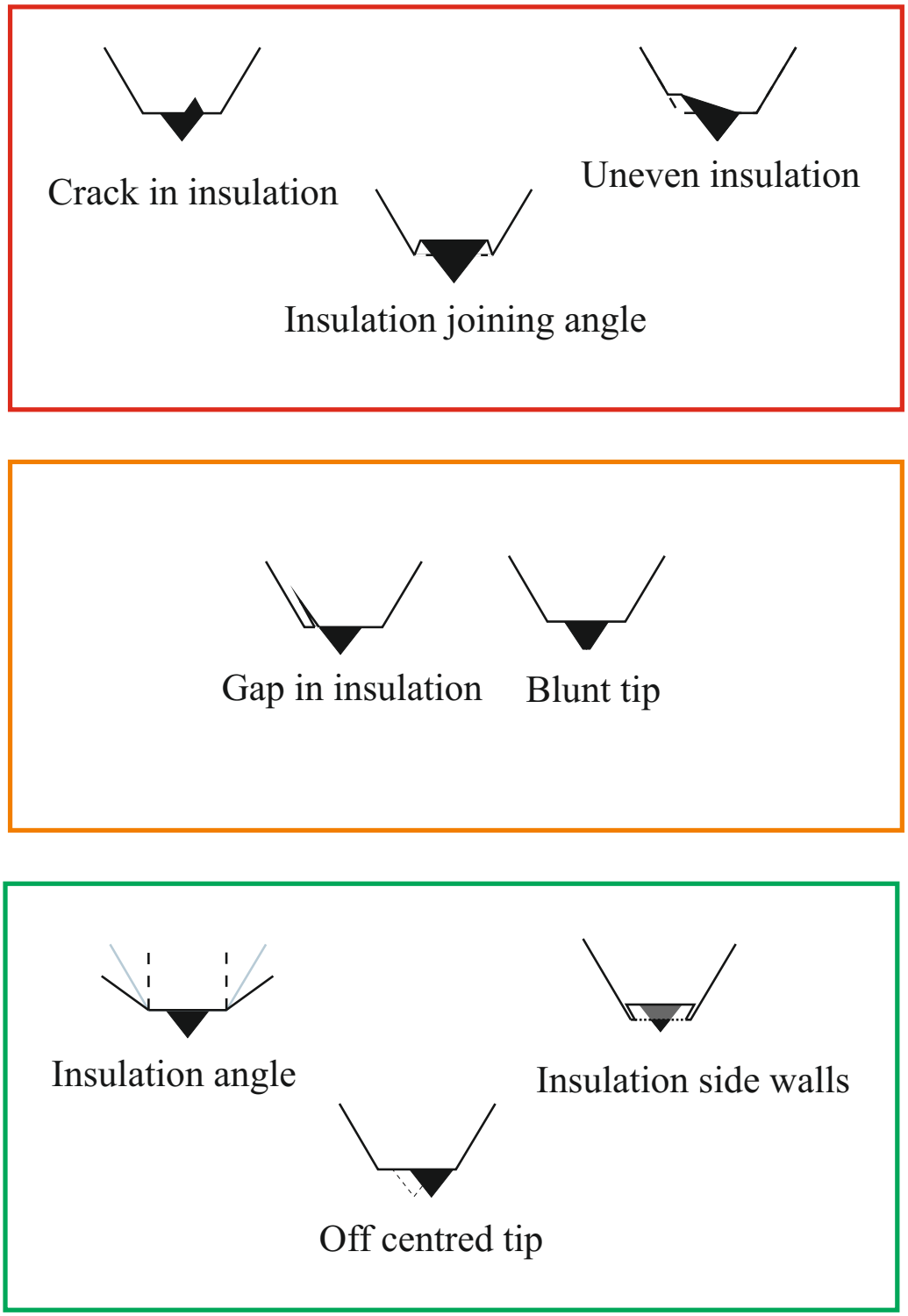

Figure 3.20: Summary of the influence of defects. In green, negligible defects for defective tip currents within the experimental error; in orange, defects that may seriously affect the bulk limiting current, dependent on the extent of the defect. In red, defects which will greatly influence the limiting current.

Chapter 4

Spatial resolution of conical electrodes in SECM: using approach curves to study biased substrates of finite size

4.1 Literature on SECM using conical electrodes

Conical electrodes have been used in scanning electrochemical microscopy, although not commonly. As protruding electrodes, they have reduced sensitivity compared to disc electrodes, which are moreover easier to fabricate and polishable. Zoski *et al.*[120] investigated conical electrodes approaching a surface. Smaller changes in feedback currents were observed compared to disc electrodes, when generating approach curves: far away, diffusion is hemispherical and thus controlled by the radius of the cone. However closer to the surface the perturbation of the diffusion sphere results in the dependence of the current transferring to the aspect ratio of the cone, with larger aspect ratios resulting in less interaction with the substrate and subsequently a decrease in contrast. The investigation of the tips was also extended to the influence of the insulation sheath thickness, and it was shown that the R_g has a larger influence over the insulating region, as with disc electrodes. Fitting of experimental approach curves then enabled the

determination of parameters of the cone such as radius and aspect ratio. Other work includes SECM experiments by Ervin *et al.*[136], who used a sharp conical Pt tip with radius of around 1 μm to image conical membrane pores. When Penner *et al.*[131] described the fabrication of conical electrode, a possible application was mentioned: these tips could be used for Scanning Tunneling Microscopy (STM). Indeed, a sharp tip is required for STM and AFM. This is why several groups, such as ours, have aimed to fabricate conical electrodes with conical insulation.[83;98;101]

4.2 Sensitivity study in SECM using approaching probes

The issue of sensitivity -or spatial resolution- has been raised several times in scanning electrochemical microscopy, mainly: how can the sensitivity be evaluated? The modelling of approach curves has been used to investigate the imaging capabilities of electrodes of different shapes. The sensitivity is defined as the ability of a tip to resolve a specific feature of the substrate. Two main questions need to be answered:

- What is the smallest size that can be distinguished?
- How large does a region have to be before it behaves as though it is an infinite region?

Note that this chapter focusses on *spatial* resolution, whilst the following chapter presents the issue of *lateral* resolution. These two terms must not be confused. Spatial resolution, also called sensitivity, is described as the electroactive probes ability to distinguish the features of the substrate such as a conducting island embedded in an insulating matrix, as used here, or two adjacent regions of interest, using approach curves. The spatial resolution is thus a function of geometry and tip-substrate distance, as well as of the substrate considered. The lateral resolution is more uniformly defined as the distance along the $x-$ or $y-$axis necessary to fully resolve a conducting region at which full positive feedback occurs from an inert region, where full negative feedback takes place. This parameter is

therefore a function of the geometry of the probe and its position. In summary, the spatial resolution characterises how sensitive a probe is to the features of a substrate whereas the lateral resolution quantifies the transition over a boundary from one extreme mode of feedback to another.

Bard *et al.*[68] attempted to answer these questions by modelling approach curves with a microdisc probe centred over a biased disc shaped region of finite size, at which the species reduced at the microdisc probe will be regenerated. From this study, an expression was produced to calculate the size of the area necessary for it to be considered infinite:

$$h^{\infty} = 1 + 1.5L \tag{4.1}$$

This expression is valid for a disc electrode with insulation sheath thickness $R_g = 10$. This means that at $L = 1$, an island of radius 2.5 times the radius of the disc electrode would behave as though infinite. At a much smaller distance, full positive feedback currents will be obtained for conducting islands of radius $R_s = 1.15$, almost the same size as the disc electrode itself. The study of conducting islands using approach curves revealed that a region ten to twenty times smaller than the tip could be detected by the electroactive probe, when scanned at a height of $L = 0.1$ or smaller. Wittstock has discussed the issue of determining sensitivity by considering the smallest island imageable.[137] The criticism of the method was that this would not be reproducible when repeating the experiment experimentally. This is mainly due to the difficulty in finding an adequate sample to compare the theoretical study to. Amphlett and Denuault[37] conducted a qualitative study by simulating approach curves over biased conducting islands, assumed to be connected to a potentiostat. These simulations revealed that large insulation sheath radii lead to greater sensitivity towards the conducting regions.

This bibliographic study reveals that although the use of approach curves over conducting regions will not be reproducible experimentally, it will enable users of such tips to understand the scale of the response for different sized conducting substrates and will give strong indication of the most favourable tip geometry.

4.3 Aims and details of the simulations

The aim in this chapter is to model diffusion to an electroactive probe as the probe is scanned vertically, approaching the substrate perfectly centred over the conducting island studied. These approach curves will be generated for different aspect ratios and different thicknesses of deposited insulation, as well as for different conducting island sizes. There are two possibilities for the island to be conducting: a potential can be applied to the island, making it a biased island, or it can be unbiased. In this case, if a reduction takes place at the electrode, the opposite oxidation will ensue at the substrate. However, for this to happen, the reduction must also occur at the substrate, far away from where the tip position, to ensure balance of electrons transferred. The relative difference between the current over a given island size and the infinite substrate case will then be computed to determine the spatial resolution of the electroactive probe for different tip-substrate distances L. It is common knowledge that conical electrodes have worse resolution than disc electrode. In this chapter, we will quantify this difference by comparing the two geometries. As with the previous chapter, the influence of defects will be investigated to determine their influence on the spatial resolution.

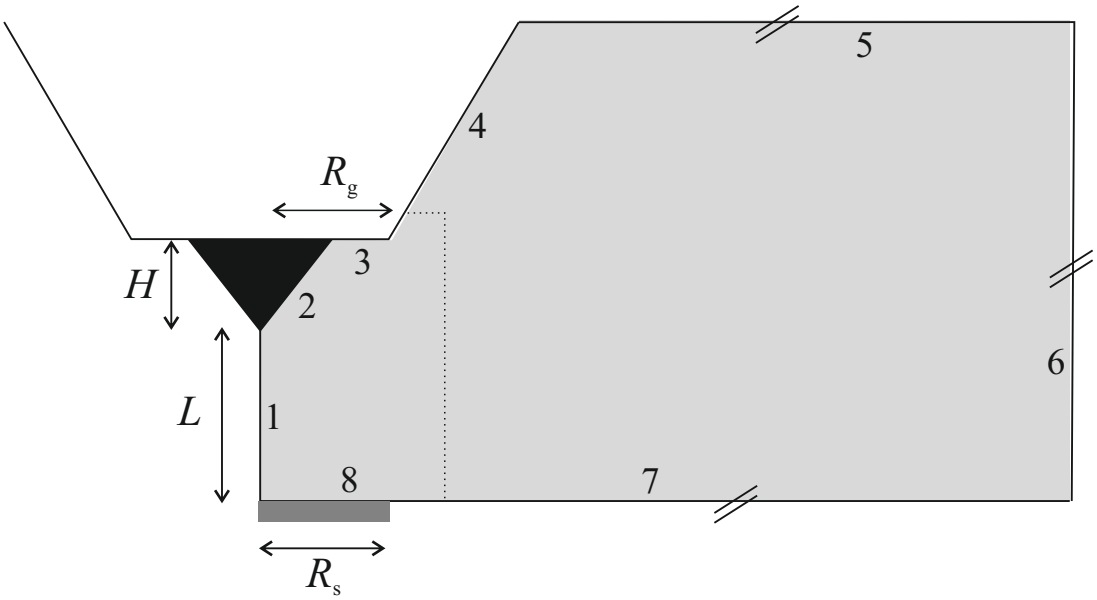

Figure 4.1: Simulation domain (in light grey) for modelling of the conical electrodes in the bulk, in dimensionless units, with boundary numbering and the meshing cylinder in dashed lines. In dark grey is the conducting island. See table 4.1

The modelling presented here is for the diffusion controlled current at conical electrodes with conical insulation at a range of tip-substrate distances L. The perfect tip model considered here is once again symmetrical, and the 'movement' of the electrode is vertical. As a result, it was once again possible to run these simulations in 2D axisymmetric. However the second part of the study, which focussed on a range of defects, was modelled in 3D, due to the break in symmetry of the electrode tip. The schematic representation of the simulation domain is shown in figure 4.1. The problem was cast into dimensionless form for the modelling, by dividing distances such as the insulation sheath thickness or the tip-substrate distance by the radius of the conical electrode, concentrations by the bulk concentration and so on, as in chapter 3.

Diffusion controlled conditions are applied: convection is ignored and the assumption is made that an excess of background electrolyte is used. The model is solved in the steady state; the equation to solve is therefore:

$$\frac{\partial^2 c}{\partial r^2} + \frac{1}{r}\frac{\partial c}{\partial r} + \frac{\partial^2 c}{\partial z^2} = 0 \tag{4.2}$$

The initial conditions of the domain are dimensionless concentration C^{b} in the entire domain, to recreate the condition of a solution containing one species only, before potential is applied to the electrode. The assumption is made that the diffusion coefficients of both the oxidised and reduced species are considered to be equal. The boundary conditions corresponding to the simulation domain shown in figure 4.1 are described in table 4.1. This model was meshed using the method

Table 4.1: Boundary conditions for the simulation model of the conical electrode with conical insulation in bulk solution, for n normal to the boundary

Boundary number	**Boundary description**	**Boundary condition**
1	Axis of symmetry	$R = 0$
2	Electrode	$C = 0$
3,4	Insulation	$^{\partial C}/_{\partial n} = 0$
5,6	Bulk boundaries	$C = 1$
7	Substrate matrix	$^{\partial C}/_{\partial n} = 0$ or $C = 1$
8	Substrate island	$C = 1$ or $^{\partial C}/_{\partial n} = 0$
Dashed lines	Meshing cylinder(Continuity)	$^{\partial C}/_{\partial n}\|_1 = {}^{\partial C}/_{\partial n}\|_2$ [1]

described previously. The mesh was defined by specifying once again a number of restrained elements along the electrode boundary, as well as restrained elements along the substrate. The growth rate was once again set to 1.1 and the overall mesh to very coarse. For smaller aspect ratios, the issue encountered with disc electrode is apparent: a more refined mesh is necessary to get good accuracy and the number of constrained elements at the electrode was increased. In 2D, this sufficed. However in 3D, a meshing cylinder was used to specify different element growth rate of 1.1 inside the cylinder. The approach curves were generated in two steps: first, the bulk diffusion limiting current was calculated at $L = 1000$, in a separate model, similar to the bulk electrode model seen in the simulation domain for chapter 3. The second step was the modelling of the probe at heights $L = 20$ to $L = 0.1$, using a second model, with adapted meshing cylinder. Note that each height is a separate model with its own geometry, its own mesh. However, this process is greatly simplified by using Matlab to define the model, thus using a loop to vary the dimensionless tip-substrate height, see appendix A. The dimensionless current can then be calculated by integrating the flux over the area of the electrode.

The accuracy of these simulations was tested by comparing a representative selection of cases to simulations with models solved using SAFE. The cases chosen ranged in aspect ratio, insulation sheath thickness and tip-substrate distance.

4.4 The influence of perfect tip geometry on the probe sensitivity

A substrate consisting of a conducting island embedded in an insulating matrix was studied. Approach curves were generated to determine the sensitivity of different probes: the current at a given height when approaching a conducting island of radius R_s was compared to the current at the same height when approaching an inert substrate. The relative difference was computed throughout

[1]This translates as the flux on one side of the interior boundary (1) is equal to the flux on the other side (2), thus rendering the interior boundary 'invisible' mathematically

the approach curve and compared to the experimental error threshold, as in the bulk. If the relative difference between the two was larger than 5%, the island was considered distinguishable, i.e. if a surface with an island of that radius was scanned, the increase in current would be larger than the experimental error and the island would therefore be imaged. The sensitivity is defined as the smallest island considered distinguishable at a given tip-substrate distance. This is intended to provide users with a guide as to what sensitivity can be expected when imaging. The sensitivity is also determined to be an index used to characterise electrodes and in particular quantify the influence of defects.

Previous work on disc electrodes by Cornut used different methods to quantify the difference between two cases: the relative difference would be used for positive feedback whereas the absolute difference was applied for negative feedback, as the current would approach very small values, and would therefore result in a large error. However, with conical electrode, contrast is very low and therefore the relative difference was used in both cases.

4.4.1 Approaching conducting discs

The sensitivity of so called 'perfect tips', tips with same half angle in the insulation and the electroactive cone and no defects, was initially evaluated. Three aspect ratios were investigated ($H = 1.5$, $H = 2.5$ and $H = 5$) and the insulation sheath thickness R_g was varied from 1.1 to 10, for each aspect ratio. Approach curves were produced by modelling the probe moving vertically over an island of radius between $R_s = 0.5$ half the radius of the electrode and $R_s = 0.01$, a hundred times smaller than the electrode radius. The approach curves were generated for each case and compared to the negative feedback curve i.e. over an entirely inert substrate. This comparison enables us to determine which islands can be distinguished: if the difference between an approach curve over a given conducting island and the negative feedback approach curve is larger than the experimental error (5%) for a given tip-substrate distance L, the change in current is deemed large enough for the region to be picked up by the probe for that distance. Four representative sets of approach curves are presented in figure 4.2

to evaluate the influence of the aspect ratio and the insulation sheath thickness on the spatial resolution of the conical tips.

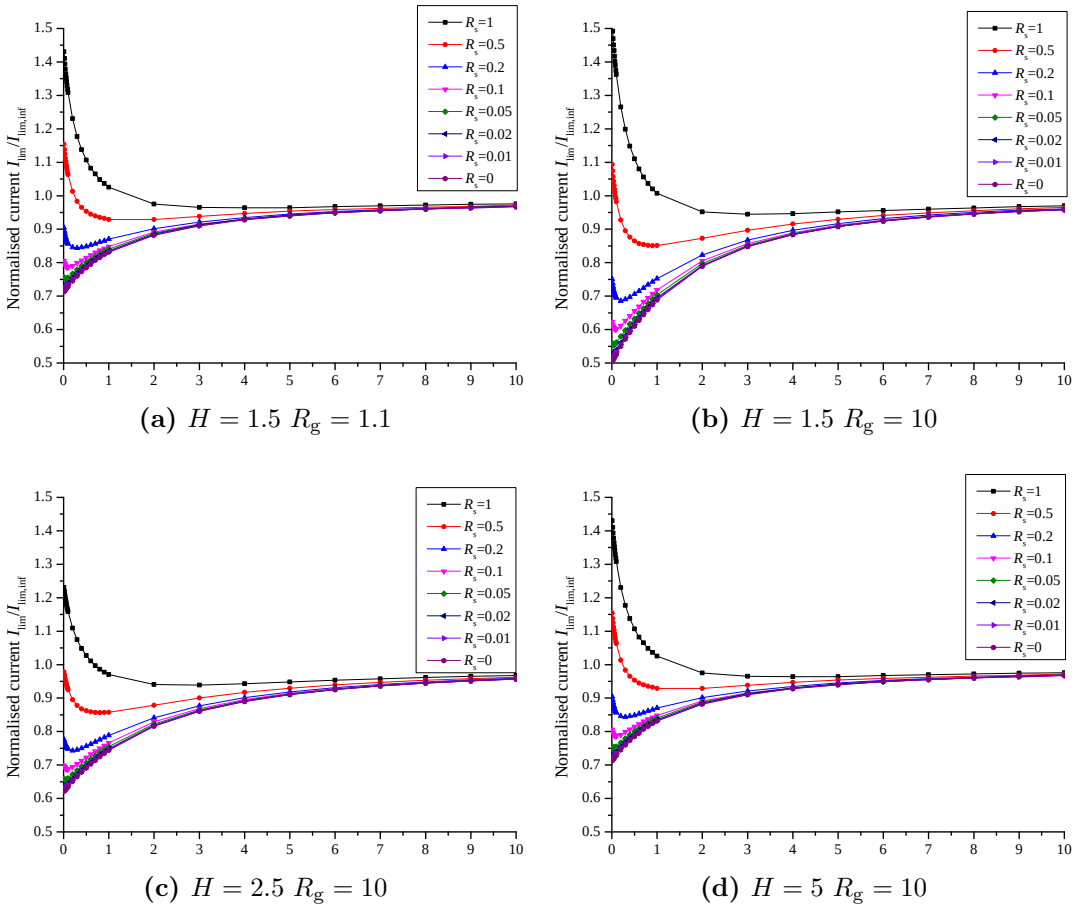

(a) $H = 1.5$ $R_g = 1.1$ **(b)** $H = 1.5$ $R_g = 10$

(c) $H = 2.5$ $R_g = 10$ **(d)** $H = 5$ $R_g = 10$

Figure 4.2: Approach curves for different tip geometry (H and R_g) and a range of conducting island radii R_s. Figures (b), (c) and (d) have different aspect ratios but the same thickness of insulation, to illustrate the influence of the cone angle on the current when the electroactive probe is approaching the substrate. Figures (a) and (b) have the same aspect ratio but a different R_g to show the effect of the insulation sheath thickness on approach curves

The approach curves observed have different shapes depending on the substrate studied. For very large islands, only positive feedback will be observed: the current always increases due to the regeneration of species at the substrate. However, as the island radius approaches the radius of the electrode, the behaviour observed is a hybrid of both positive feedback and negative feedback: the current will initially decrease which indicates that the insulating matrix surrounding the island has a big influence and hinders diffusion to the electrode. However, as the probe gets closer to the island, the efficiency of regeneration of

species increases thus resulting in positive feedback: the current increases. The influence of the conducting island dominates the hindering by the surrounding insulating matrix. The smaller the island, the closer the probe has to be to the substrate before the switch from negative to positive feedback is observed. Eventually, for the smaller sized islands, only negative feedback is observed, when the island is too small for the production of oxidised species to be reduced at the electrode to overcome the hindering of diffusion by the inert substrate.

4.4.2 Influence of the aspect ratio on the sensitivity

The influence of the sharpness of the electrode was firstly evaluated by fixing the insulation sheath thickness to $R_g = 10$ and varying the aspect ratio from $H = 5$ to $H = 1.5$; the approach curves generated can be seen in figure 4.2b, c and d. It was observed that the larger aspect ratios gave the smallest range of normalised current, with both negative and positive feedback curves much less pronounced with sharp tips. This is due to the increased back diffusion with large aspect ratio. As mentioned above, the aim of this study was to determine what size island could be detected by the probe. For a tip with aspect ratio $H = 5$, the smallest island distinguishable for $R_g = 10$ is $R_s = 0.1$, i.e. ten times smaller than the electrode. For $H = 1.5$, an island twenty times smaller than the electrode can be detected. The area of the electroactive region for a tip with $H = 5$ is almost three times the area of a tip with $H = 1.5$. As a result, the influence of the regeneration of species occurring at the conducting region is smaller in proportion to the diffusion layer size, which is why higher aspect ratio tips have smaller sensitivity. The extension of this confirms previous work which mentioned disc electrodes (or $H = 0$) have much better spatial resolution than protruding electrodes such as conical electrodes. In fact, repeating this experiment for a disc electrode of radius $R_g = 10$, revealed that islands as small as a fifty times smaller than the electrode resulted in an increase in current big enough to be considered detectable. To put this into perspective, an electrode of radius $r_{tip} = 500$ nm and $R_g = 10$ would therefore be able to distinguish a conducting island of radius 100

nm for aspect ratio $H = 5$ and 25 nm if $H = 1.5$, compared to 10 nm for a disc electrode of the same electrode radius and R_g.

4.4.3 Influence of the insulation sheath thickness on the sensitivity

The influence of the insulation sheath thickness was then investigated by fixing the aspect ratio to $H = 1.5$, $H = 2.5$ and $H = 5$ and varying the R_g between 10 and 1.1. Two representative curves are shown in figure 4.2c and d. It is observed that the normalised current range is reduced for the smaller insulation sheath compared to the case where $R_g = 10$. The curves corresponding to the smaller values of R_s are more difficult to distinguish. This will result in poorer sensitivity for the tips with smaller insulation. The smallest islands, of radius $R_s = 0.02$ and $R_s = 0.01$, cannot be distinguished at any height considered here. This means that the smallest island that can potentially be distinguished is twenty times smaller than the electrode radius. This also shows that tips with larger R_g have better sensitivity even though the current is reduced by the blockage of the insulation. With small R_g, there is a lot of back diffusion where with thicker insulation, the diffusion is spread toward the substrate and the current reduced. However the diffusion layer is spread over the area close to the substrate, making the tip more sensitive. The back diffusion seen with small insulation sheath results in a smaller diffusion layer, however the sensitivity is lost in the back diffusion. The ideal tip with respect to spatial resolution would therefore have an aspect ratio as small as possible and a large R_g. Take a tip with $H = 1.5$, $R_g = 5$ and a radius $r_{tip} = 100$ nm. This tip would be able to distinguish an island of radius 20 nm from 100 nm, radius 10 nm from a distance of 80 nm and radius 5 nm from 20 nm.

4.4.4 The influence of tip-substrate distance on the sensitivity

The spatial resolution as a function of the tip height is presented using the histograms shown in 4.3 these are used to represent the distance from which a given sized island - defined by its radius R_s - is detected.

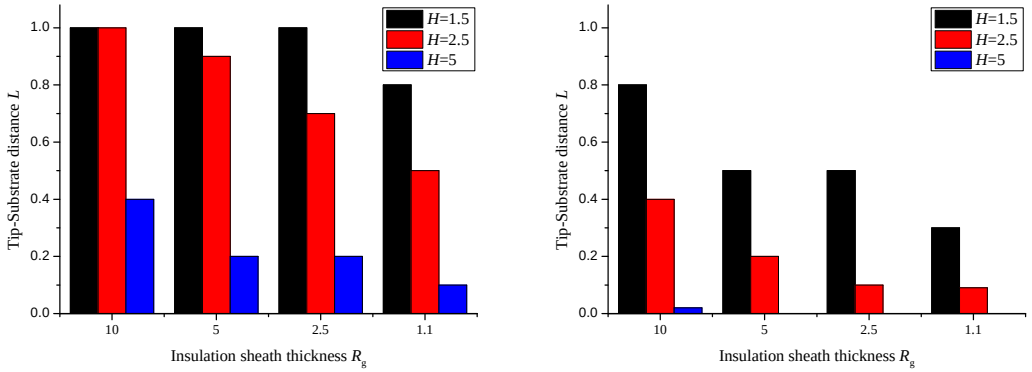

(a) $R_s = 0.2$ **(b)** $R_s = 0.1$

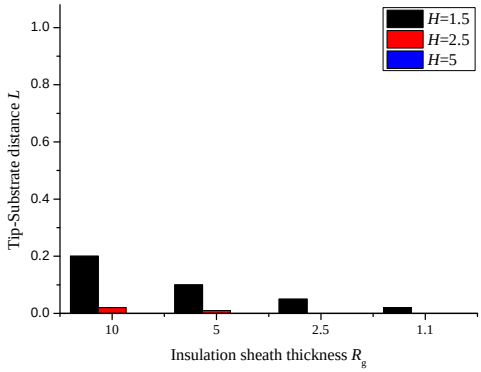

(c) $R_s = 0.05$

Figure 4.3: Histograms showing the dimensionless tip-substrate distance L required to distinguish an island of radius R_s for a given aspect ratio H and insulation sheath thickness R_g

They reveal that all aspect ratios can detect islands of radius five times smaller than the electrode radius from at least $L = 0.1$. Tips with aspect ratios of $H = 2.5$ and smaller will be able to resolve regions of radius twenty times smaller than the electrode radius, with larger insulation sheaths more sensitive; the electrode needs to be very close to the substrate, although as these tips are used in AFM-SECM, it is expected that the tip-substrate distance will be in the nm range.The plot presented highlights the loss in sensitivity between the different geometries:

although all tips with aspect ratio $H = 5$ can distinguish an island of radius $R_s = 0.2$, a large insulation sheath radius will detect this from a large tip-substrate distance and the current increase observed will be larger, thus making the feature easier to distinguish.

4.4.5 Conducting discs exhibiting infinite substrate behaviour

As part of the definition of spatial resolution, it was necessary to determine when a conducting island behaves as though infinite, i.e. for which tip-substrate distance L and tip geometry (H and R_g). Zone diagrams have been generated for six different tips, with varying aspect ratio and insulation sheath thickness, for users to refer to, see figure 4.4. For completeness of the study, zone diagrams have also been generated to show when small conducting islands are too small to differ from the infinite insulating case as well as when they are large enough to behave as though infinitely conducting.

The zone diagrams in figure 4.4 compare the current over biased conducting islands with the current over an infinite conducting substrate. The behaviour of the conical electrodes over large conducting islands is closer to the full positive feedback case. The aim was to determine which size conducting island behaves as though infinite. This study has revealed that it is very much a function of tip-substrate height L. For large islands, the current is within experimental error of the limiting current for all tip-substrate distances. As the conducting island size decreases, the current begins to differ from the infinite substrate case. Initially this is observed at larger tip-substrate distances. This is due to the surrounding insulating sheath having more of an influence than the conducting island, and hindering diffusion. Eventually, the tip is close enough to the substrate that its diffusion layer is sufficiently small, reduced by the availability of oxidised species, that the surrounding insulation no longer influences the current. However, the radius of the conducting region ultimately becomes too small even at short tip-substrate distances for the regeneration of species to outweigh the blockage by

the inert surface, the hindrance of the diffusion layer will thus result in a change in current larger than the experimental error.

As the size of the conducting islands becomes smaller than the electrode, the current as a function of tip-substrate distance approaches the infinite insulating substrate case: the hindering of the surrounding insulating sheath results in an initial decrease in current. The zone diagrams in figure 4.5 represent the difference between the current over a conducting disc with the current over an entirely inert substrate, with the x axis plotted on a log scale. Two regions are distinguished: the first -in green- represents the region where the current is within experimental error of the full negative feedback current. In these regions, the conducting island is too small and cannot provide enough species to react at the electrode to significantly reduce the spread of the diffusion layer and thus increase the current. The blue regions are areas where the relative difference in current between the cases compared is larger than 5% and the conducting island is considered to be detectable. Trends are confirmed: the closer the tip is to the substrate, the smaller the islands it can distinguish from a surrounding inert matrix. The tip with the best sensitivity is confirmed as small H and large R_g simply by looking at this plots, as this tips has the largest blue area, i.e. largest area of 'detectable islands'.

The zone diagrams reveal that the aspect ratio has got a much larger influence than the insulation sheath thickness, in particular over conducting islands. Note that the tip-substrate distance also has a much larger influence over the insulating substrate. Over the conducting substrate, there is a big difference between the three different aspect ratios presented, where as over the insulating region the two largest aspect ratios have very similar sensitivity.

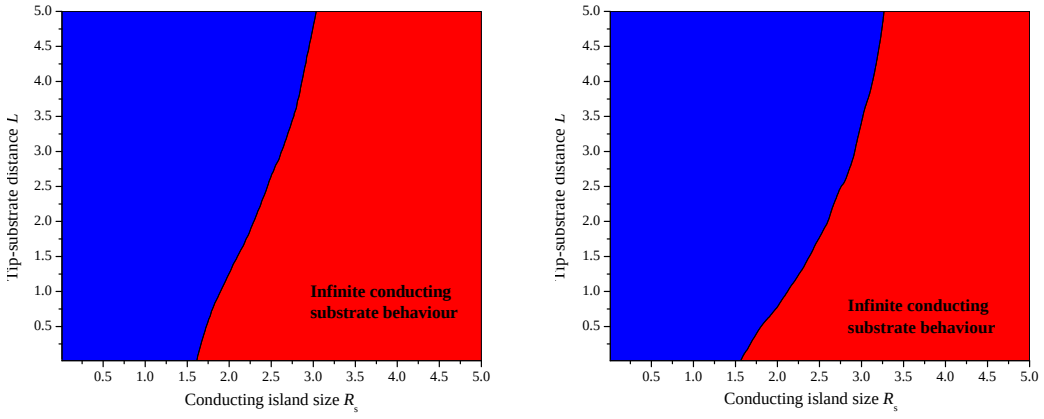

(a) $H = 1$ $R_g = 1.1$

(b) $H = 1$ $R_g = 10$

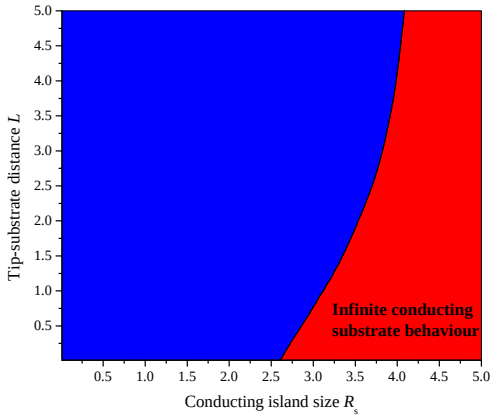

(c) $H = 3$ $R_g = 1.1$

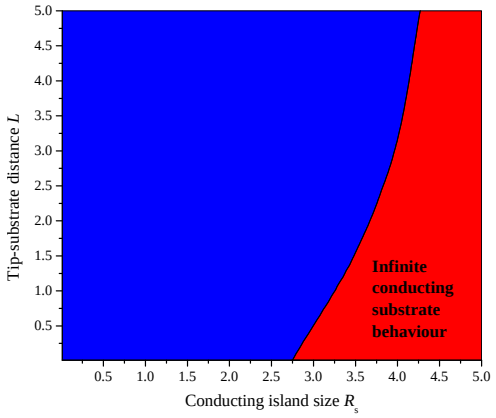

(d) $H = 3$ $R_g = 10$

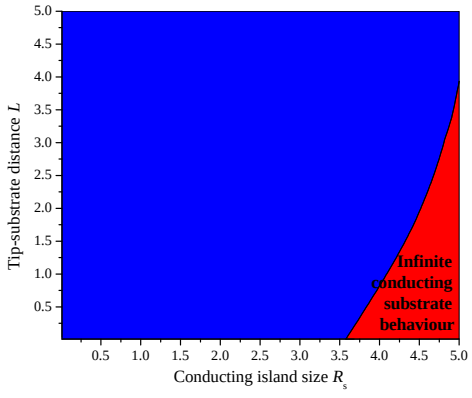

(e) $H = 5$ $R_g = 1.1$

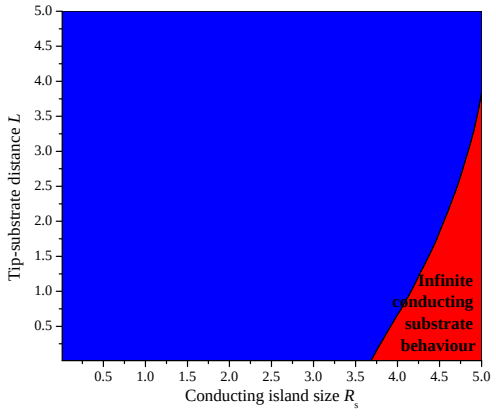

(f) $H = 5$ $R_g = 10$

Figure 4.4: Zone diagrams presenting the behaviour of conical electrodes of different aspect ratios H and insulation sheath thickness R_g in comparison with infinite substrate behaviour. In red, the response of the conducting island is within experimental error of the infinite conducting substrate case; whereas the blue section represents conditions for which the relative difference between the two cases is larger than the experimental error.

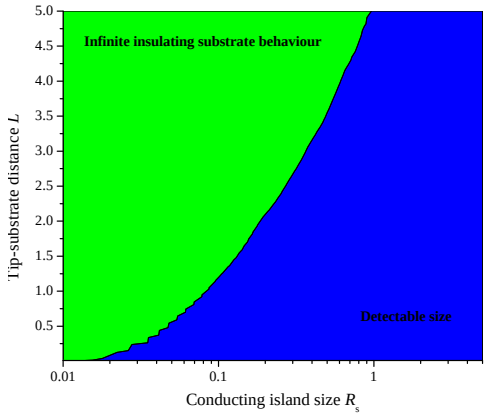

(a) $H = 1$ $R_g = 10$

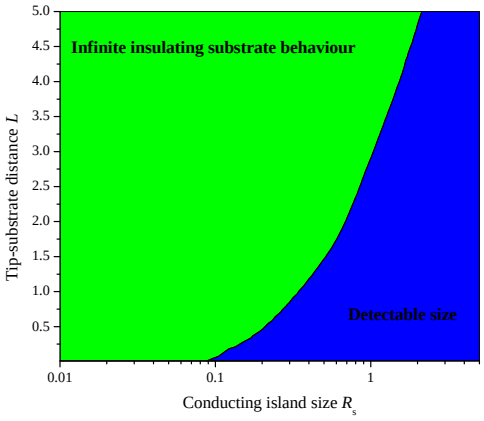

(b) $H = 3$ $R_g = 1.1$

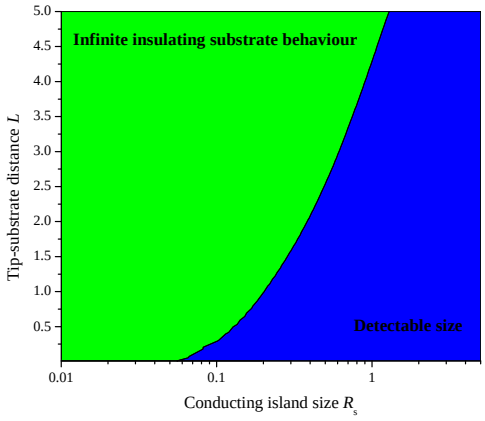

(c) $H = 3$ $R_g = 10$

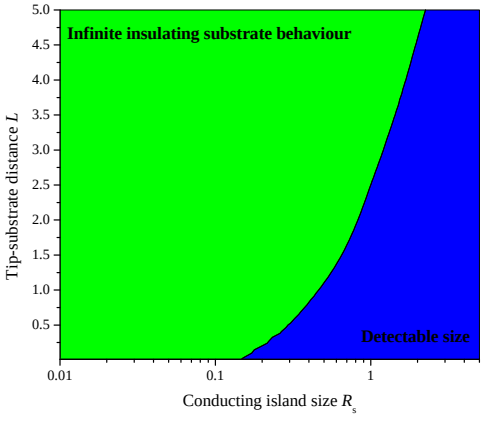

(d) $H = 5$ $R_g = 1.1$

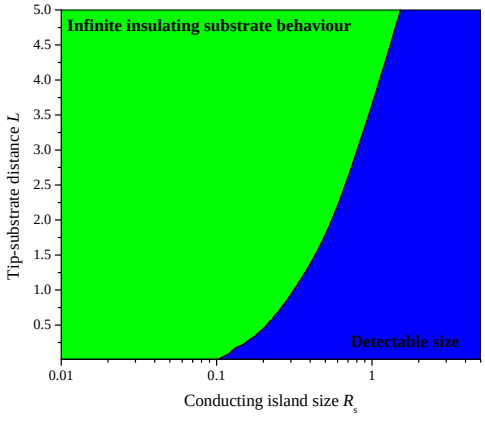

(e) $H = 5$ $R_g = 10$

Figure 4.5: Zone diagrams presenting the behaviour of conical electrodes of different aspect ratios H and insulation sheath thicknesses R_g compared to the current over an entirely inert substrate. In green, the response of the conducting island is within experimental error of the infinite substrate case whereas in blue, the current differs from current over the entirely inert substrate, meaning the islands corresponding to this region are considered detectable.

4.4.6 Summary

An extensive study of substrates containing conducting islands has been performed and the spatial resolution of conical electrodes has been determined. As expected, the spatial resolution was shown to be worse than for disc electrodes. The extension of this fact was that the larger the cones aspect ratio, the worse the sensitivity. The investigation into the influence of the insulation sheath thickness revealed that with regard to the spatial resolution, a larger insulation sheath thickness is favourable as the diffusion layer is spread towards the substrate thus making the 'electrochemical radar' more sensitive to the substrate reactivity. Zone diagrams and histograms are provided for users to extract information from such as comparison to entirely insulating and conducting substrates, as well as the smallest circular region distinguishable. This will be useful to extract information such as what size inclusion would be detected when studying corrosion.

4.5 The spatial resolution of defective conical tips

The sensitivity of tips presenting a range of insulation defects was considered. The aspect ratio was set to $H = 1.5$ and the insulation radius was varied between $R_g = 5$ and $R_g = 2.5$. Three typical defects were considered: the insulation joining angle -the insulation forms a crater around the electrode as depicted in figure 4.6(a), the insulation angle -the insulation half angle is not equal to the electroactive cone half angle, see Figure 4.6(b), and the off centred tip, see figure 4.6(c). As with the perfect tip case, approach curves were generated by recording the current I_{lim} at decreasing tip-substrate distances L and normalising by the limiting current in the bulk $I_{\text{lim,inf}}$. The current was normalised for the perfect tip with the perfect tip bulk current and with the defective tip bulk current for the defective tip. This was done with for a substrate consisting a conducting island of varying radius R_s, embedded in an insulating matrix, and compared to

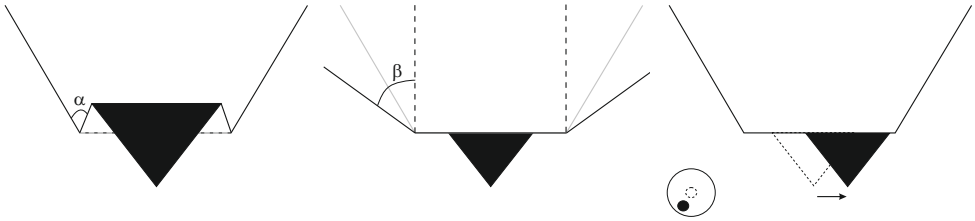

(a) Insulation joining angle **(b)** Insulation angle **(c)** Off centred tip

Figure 4.6: Schematic representations of the defects for which the sensitivity is evaluated

the case of an entirely inert substrate in order to calculate the sensitivity of the probe.

The defects that were investigated in the bulk revealed that some had quite a large influence on the limiting current in the bulk, whereas the effect of others was negligible. The next section of this chapter will investigate three of the defects further.

4.5.1 The insulation joining angle

This defect was studied in the bulk and was shown to be the most detrimental to the tip response as a small change in insulation joining angle would result in a large change in exposed electroactive area. The presence of this defect would dramatically affect the limiting current measured at the electrode and is therefore expected to significantly reduce the sensitivity of the electrode. The first case considered focussed on a probe with $R_g = 5$ and an insulation joining angle of $\alpha = 10°$ smaller than perfect. In the bulk, the current would be increased by 74% compared to the current at a perfect tip ($\alpha = 123.7°$).

The approach curves, shown in figure 4.7, reveal the extent of the influence of the defect: the normalised limiting current of the defective tip decreases much more with decreasing tip-substrate distance L. The normalised current for the defective tip reaches 1 at long times but the plateau is reached at much larger tip-substrate distance due to the increase in exposed area resulting from the defect. As the exposed area is increased, larger conducting islands will be sensed from a larger tip-substrate distance: the outer layer of the diffusion layer will occupy a much larger space and will therefore be affected by the substrate at a larger

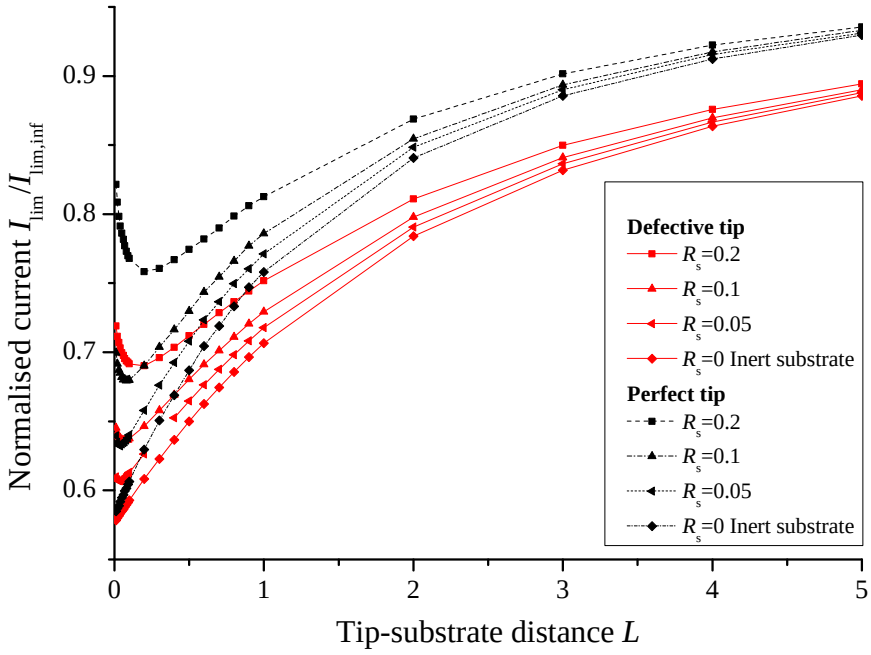

Figure 4.7: Approach curves for a perfect tip with $H = 1.5$ and $R_g = 5$ compared to a defective tip with the same dimensions but an insulation joining angle of $\alpha = 113.7°$

L value. The approach curve has a different shape as a result of the defect: the current will start decreasing from a larger distance, once again due to the larger exposed area. However the regeneration of species at the electrode will be less efficient in comparison with the size of the diffusion layer: less contrast will be observed and the probe will be less sensitive.

4.5.2 The insulation angle

The study in the bulk of this defect revealed that an insulation angle larger than perfect resulted in a smaller current, due the spreading of the diffusion layer. However with an angle smaller than perfect, there is increased back diffusion and the current is subsequently larger.

The plot of figure 4.9 reveals the influence of the different defects studied. The relative error increases much slower for the defective tip and will only rise above 5% for $L = 0.1$ as opposed to $L = 0.01$ for the perfect tip. This means that the defective electrode will have to be ten times closer to the substrate than the

perfect tip to distinguish an island of the same size. There is therefore a large loss in sensitivity associated with this defect.

Two cases were considered here: $\beta = 20°$ and $\beta = 50°$, where the perfect angle would be $\beta = 33.7°$. The approach curves for both theses cases are shown in figure 4.8 From the plots of the relative error, see figure 4.9, it is observed that there is not a big difference between the perfect tips and the defective tips; however, trends are observed. A large insulation angle will spread the diffusion layer towards the substrate which improves the sensitivity, whereas the back diffusion occurring with a small insulation angle leads to a loss in sensitivity. The trends observed are more evident for smaller insulation thickness. This study revealed that any insulation angle is acceptable and will not impact greatly on sensitivity.

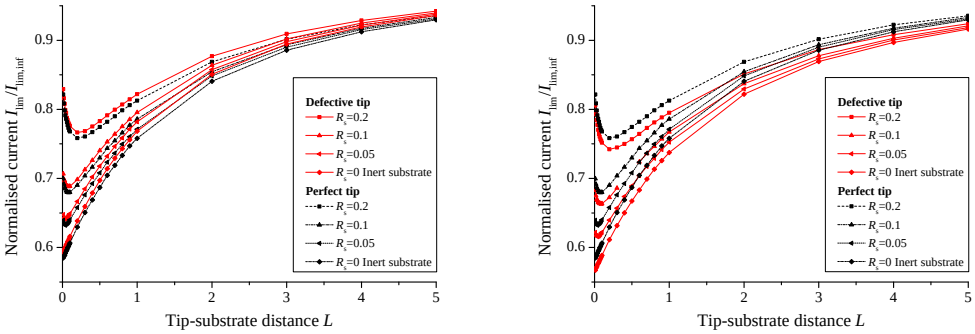

(a) Insulation Angle $\beta = 20°$ **(b)** Insulation Angle $\beta = 50°$

Figure 4.8: Approach curves for tips presenting defects in the insulation angle, whether larger or smaller than the perfect tip insulation angle above conducting islands of different sizes.

4.5.3 The off centred tip

An off centred tip was shown to have very little influence on the limiting current in the bulk: even the worst case scenario considered for an electrode with $R_g = 10$, resulted in an increased in current slightly larger than the experimental error. As observed in figure 4.9, the relative difference is much smaller for the defective tip. This means that the approach curve over the island is very close to the approach curve over the insulation. However, the increase in relative difference is the same as for the perfect tip and overall the loss in sensitivity is very small. This confirms

the findings from the study in the bulk which revealed the negligible influence of this defect.

4.5.4 Summary

The spatial resolution has been defined as the smallest island distinguishable at a given height L. The current above a conducting island was compared with the current above an insulating substrate and the relative difference between the two was computed and used to determine whether an island could be detected. The relative difference is plotted for the different defects in 4.9.

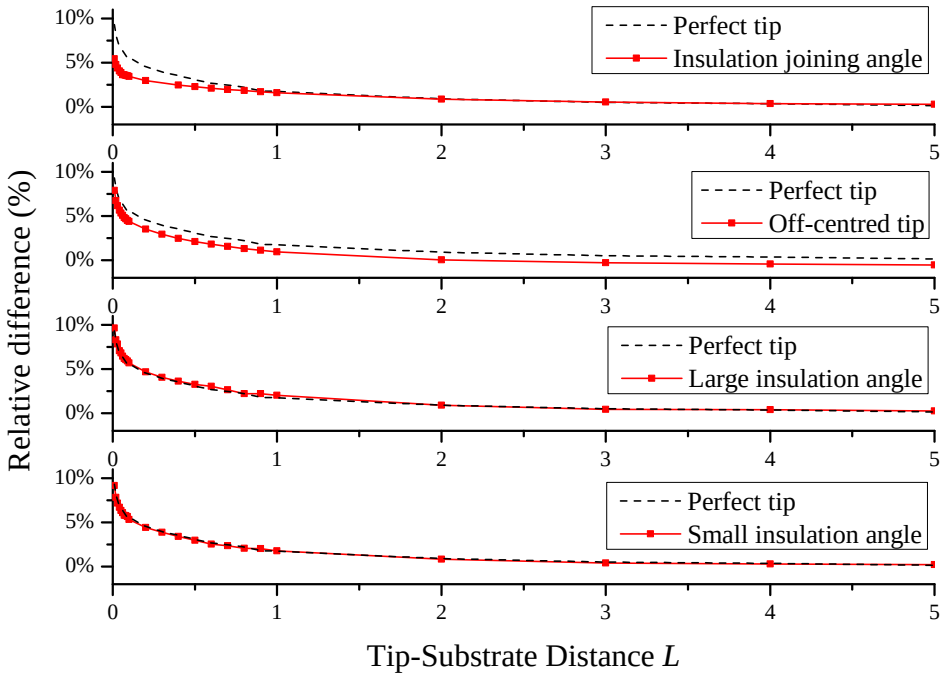

Figure 4.9: Plot of the relative difference between the approach curve over an island of radius $R_s = 0.05$ and the approach curve over an insulating substrate, as a function of the tip-substrate distance L, for the defects discussed in this section

This plot is not an approach curves, but a plot of the relative difference between the approach curve over a conducting island $R_s = 0.05$ and the negative feedback approach curves, as used to determine whether an island is detectable or not. This is plotted for the perfect tip compared to the defective tip to enable the visualisation of the loss in sensitivity.

Of the defects considered, the insulation joining angle was determined to have the largest influence, predominantly due to the increase in exposed area. The loss in sensitivity of the other defects is much less evident. In fact, for the two insulation angles considered, the difference is negligible, observed as the curves overlap.

4.6 Conclusion

A combination of 2D axisymmetric and 3D modelling has been successfully performed to determine the sensitivity of both perfect and defective tips. An extensive study of conducting islands embedded in an insulating matrix revealed the imaging capabilities of conical electrodes. In particular, the influence of the geometrical parameters were studied. Simple plots were provided for users of conical tips to refer to, enabling them to instantly know what size features could be resolved for a given (H,R_{g}) and what size conducting island will behave as though an infinitely conducting surface.

Chapter 5

Determining the lateral resolution of conical electrodes using line scans in the feedback mode

5.1 Previous work on determining the lateral resolution of SECM probes

In this chapter, the study of the electrochemical response of the conical electrodes is presented, when scanned at constant tip-substrate distance above a surface of interest. The previous chapter focused on the spatial resolution measured using an approach above the substrate. In this chapter, horizontal scans are used to determine the lateral resolution. As with spatial resolution, different methods have been used to determine the lateral resolution, with definitions varying.

Davoodi *et al.*[97] studied the lateral resolution of two probes by modelling the line scan above two active sites of varying size and separation. It was determined that with a disc electrode of radius 1 μm, two actives sites (radius 1 μm) could be distinguished for a separation of a few μm. The aim of this work was not to compare the influence of the geometrical parameters but instead to get an

idea of the capabilities of such electrodes. This is an interesting method and it is useful to know if a surface is being scanned, whether two conducting regions of close proximity will be individually resolved. However the number of factors -the height of the scan, the island sizes and the island separation- considered here makes this a difficult problem to apply to a wide range of geometries and thus draw conclusions.

Amphlett *et al.*[37] modelled a line scan over two infinitely long conducting strips, embedded in an insulating plane. Scans were run for different insulation sheath thicknesses and it was determined that the best resolution was for an insulation sheath $R_g = 2$, as although the larger insulation sheath results in a larger increase in current, the distance necessary to resolve the boundary between the two regions is greatly increased with increasing insulation sheath thickness. The conclusion of the study was that a large insulation sheath offered better sensitivity but worse lateral resolution.

Wittstock *et al.*[137] determined the resolution using a simple line scan over two areas: one insulating and one conducting. By taking into account the change in current between the two regions and the gradient of the slope, as demonstrated with recent SECM experiment,[78] the lateral resolution was determined. The number extracted is understood to describe the distance necessary to fully resolve one region from another. This example is limited as it can only be applied to the very simplest of cases. This is however the reason it is a good way of evaluating the lateral resolution of an electrode: different geometries can be investigated and the one for which this distance is the smallest will be the best geometry, i.e. have the best resolution. It is expected that the line scan with lowest distance calculated would enable the best resolution when scanning active sites. This method will therefore be preferred in this study into the imaging capabilities of AFM-SECM probes.

Fulian *et al.*[40] also calculated the resolution using a substrate with two large regions, one conducting, one insulating. Two tip-substrate separations were investigated and highlighted the importance of the scan height L in the magnitude of current observed. In a later publication,[138] 3D simulations were used to model single and multiple adjacent conducting islands embedded in an insulating ma-

trix. This was used to compare the resolution of different electrode(hemispherical, embedded disc and recessed disc).

Borgwarth *et al.*[67] use experimental results to investigate the influence of the tip-substrate distance on the resolution. Disc electrodes were used to image conducting islands of 100 μm radius and the cross section through the peaks were used to measure the diameter of the island for different tip-substrate distances. This study revealed that there was a linear relationship between the measured diameter - determined using the current plateau over the conducting region - and the scan height. The study was then extended to arrays of conducting and insulating discs ranging from 7.5 μm to 100 μm. This revealed that conducting islands of radius 50 μm could be individually resolved. However insulating islands of radius 7.5 μm cannot be resolved. Finally a single conducting band of 500 nm width was imaged at constant height and it was revealed that a peak would be obtained for a region of that size.

The key aim of this work is to determine the lateral resolution of the conical electrodes and in particular determine the influence of the geometry of the tip on the calculated resolution. The aim of the modelling in the context of the development of these electrodes is to liaise with fabrication to produce the electrode with the highest imaging capabilities. By modelling approach curves over conducting island embedded in an insulating matrix, we determined the sensitivity of these probes. The simulation of line scans over fully conducting and insulating regions enabled us to calculate the lateral resolution of such electrodes. This was repeated firstly for various cone half angles and insulation sheath thicknesses, and secondly for different defects. This will enable us to derive guidelines for the user of such tips as to what sensitivity and resolution to expect from a given tip.

5.2 Aim and simulation details

The aim of the modelling presented in this chapter is to use the expression first introduced by Wittstock to quantify the lateral resolution of electrodes and in particular monitor the influence of the geometrical parameters of the conical

electrodes such as the aspect ratio H and insulation sheath thickness R_g, with in mind to determine the ideal tip geometry, i.e. the tip which will give the highest resolution when scanning a real-life substrate.

This set of experiments was modelled in 3D, mainly as there was no symmetry to be exploited. The model is once again cast into dimensionless quantities. The geometry of the cone is itself symmetrical for the perfect tips considered, though the symmetry is broken by the horizontal scanning of the surface, as well as with the defects taken into account in the second part of this study. The geometry is described by the aspect ratio H and the insulation sheath thickness R_g as well as the position of the tip (X, Y, L), for tip-substrate distance -or scan height- L. Once again diffusion controlled currents are considered with migration and convection ignored. The initial conditions are concentration $C^b = 1$ in the entire domain for dimensionless diffusion coefficient $D = 1$. A meshing cylinder was included, surrounding the electrode tip with a subdomain of smaller size, thus enabling a more refined mesh. The maximum element size was the most important parameter and was set to 0.05 on the electrode boundaries. The element growth rate in the meshing cylinder was set to 1.2, meaning any element could only be 20% bigger than the adjacent element, growing away from the electrode. In the remainder of the domain, a much larger element growth rate was set to ensure the bulk solution was not unnecessarily finely meshed. It was not necessary to refine the substrate mesh as the refinement at the electrode combined with the proximity of the tip (tip to substrate distance during scan was smaller than $L = 0.1$) and the slow growth rate meant the required accuracy was met. The current at the electrode was once again computed by integrating the flux over the area of the electrode and this was normalised by the current in the bulk, measured for a tip-substrate distance of $L = 1000$.

A difficulty arose with this model. The boundaries are numbered by beginning in one corner and working to the opposite corner of an imaginary 3D cube, containing the simulation domain. This was not a problem with the vertical scan as the only movement was, obviously, in the z-direction. However, when scan-

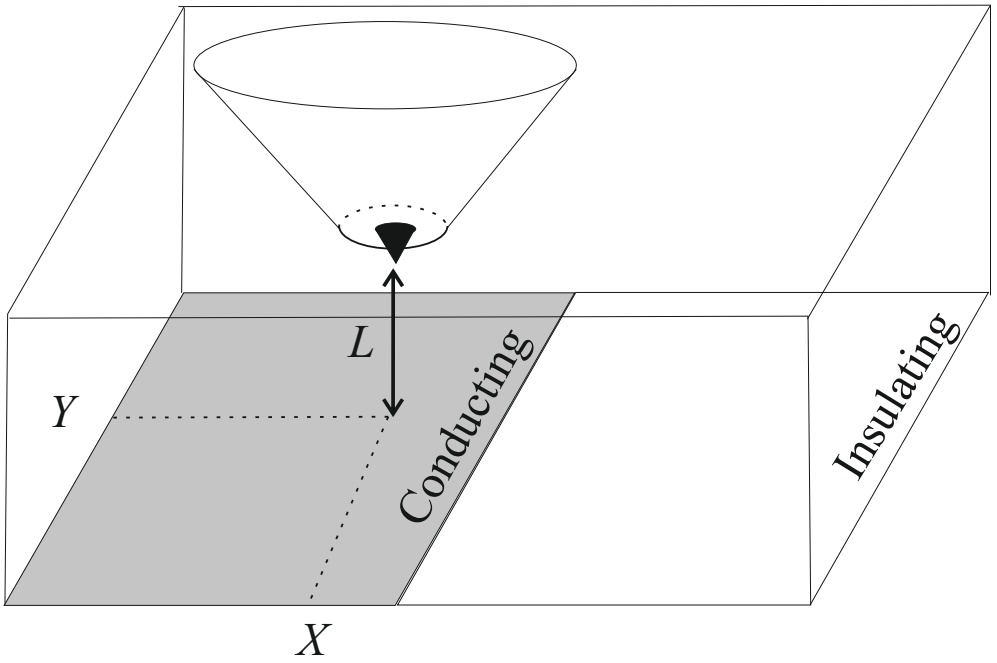

Figure 5.1: Schematic representation of the simulation model used to determine the lateral resolution, with in black the electroactive cone acting as the electrode and in grey the conducting region of the substrate, where the species consumed at the electrode is regenerated

ning horizontally, boundaries would cross and boundary conditions would then be wrongly assigned. As a result, the model would change throughout the line scan. This is due to the fact that line scans are created by solving a series of individual and unrelated simulations, one for each position of the probe.

Therefore, in one model, boundary no. 3 could be representing a boundary of the insulation sheath, but once the substrate boundary (embedded disc or line) was crossed, would then become boundary no. 7, which has been defined as a conducting boundary. An option in COMSOL was to map the boundaries, remembering the relationship between the different boundaries as they changed. The added difficulty with this model is the meshing cylinder used. As this moved with the probe, the boundary numbers as well as numbering would change, thus making the option of mapping impossible.

This was resolved by importing the substrate boundary as a map of the electron transfer rate. A mathematical function would describe for each point of the boundary the value of Λ, the dimensionless transfer rate constant. To recreate an insulating substrate, $\Lambda = 0$, which will ensure that once species have reached the substrate, they do not react. The boundary conditions at a biased substrate

are created by setting the rate constant to $\Lambda = 10000$: this is fast enough for the species to react as soon as they reach the substrate boundary. Different large values of Λ were tested and then compared against the case of a boundary with condition $C = 1$ to check for agreement, thus confirming the validity of this approach. The function used is a smoothed step function and the following nomenclature is used, where the function *flc2hs* is a smoothed Heaviside function:

- Substrate with a conducting and an insulating region; for any $x \leq x_{\min}$ the value of the function is 1:
  $\Lambda = 10000 * flc2hs(x - x_{\min}, 0.001)$

- Insulating line embedded in a conducting region:
  $\Lambda = 100000 * flc2hs(y_{\max} - y, 0.001) * flc2hs(y - y_{\min}, 0.001) * flc2hs(x - x_{\min}, 0.001) * flc2hs(x_{\max} - x, 0.001)$

- Conducting line embedded in an insulating matrix:
  $\Lambda = 100000 * (1 - flc2hs(y_{\max} - y, 0.001) * flc2hs(y - y_{\min}, 0.001) * flc2hs(x - x_{\min}, 0.001) * flc2hs(x_{\max} - x, 0.001))$

- Conducting disc embedded in an insulating matrix:
  $\Lambda = 10000 * (1 - flc2hs((x - X)^2 + (y - Y)^2 - 0.2, 0.001))$

- Two conducting discs embedded in an insulating matrix:
  $\Lambda = 10000 * (1 - flc2hs((x - X_1)^2 + (y - Y_1)^2 - 0.2, 0.001)) + 10000 * (1 - flc2hs((x - X_2)^2 + (y - Y_2)^2 - 0.2, 0.001))$

Any shape that can be described by a function or a combination of functions can thus be imaged. The number specified as part of the function clarifies the interval over which a smoothed Heaviside function with continuous second derivative is defined. The smaller this number, the better.

With the method of defining the boundary problems successfully implemented, simulations were run in 3D for a range of geometries and substrate, first varying the geometry of the perfect tip and secondly investigating defects.

5.3 The lateral resolution as a function of the perfect tip geometry

5.3.1 Calculating the lateral resolution

The lateral resolution, described as the distance necessary to fully resolve one region from another, is calculated using the line scan over the separation between a large insulating and conducting region.
The general expression to determine the gradient of a curve is given by:

$$gradient = \frac{y_2 - y_2}{x_2 - x_1} \tag{5.1}$$

By manipulating this data, the expression for the lateral resolution can be determined :

$$\Delta x = x_2 - x_1 = \frac{\Delta y}{gradient} \tag{5.2}$$

where $\Delta y = y_2 - y_1$ is the difference in current plateau over the insulating compared with the current plateau over the conducting region, as shown in figure 5.2.

The lateral resolution is therefore determined by firstly simulating the line scan above the substrate, as depicted in figure 5.2 for a tip with aspect ratio $H = 1$, insulation sheath thickness $R_g = 1.1$ at tip-substrate distance $L = 0.01$. ΔI is the difference between the current over the insulating area and the current over the conducting area. The numerical differentiation of the line scan will allow the determination of the inflection point, see figure 5.2. The lateral resolution ΔX is then calculated by dividing the difference in current plateau ΔI by the value of the derivative at the inflection point:

$$\Delta X = \frac{\Delta I}{\left(\frac{\partial I_{\text{lim}}}{\partial X}\right)_{\text{inflection}}} \tag{5.3}$$

This expression takes into account the increase in current from the insulation region to the conducting region, as well as the value of the gradient at the steepest point of the slope, and gives a numerical value to describe the resolution of an

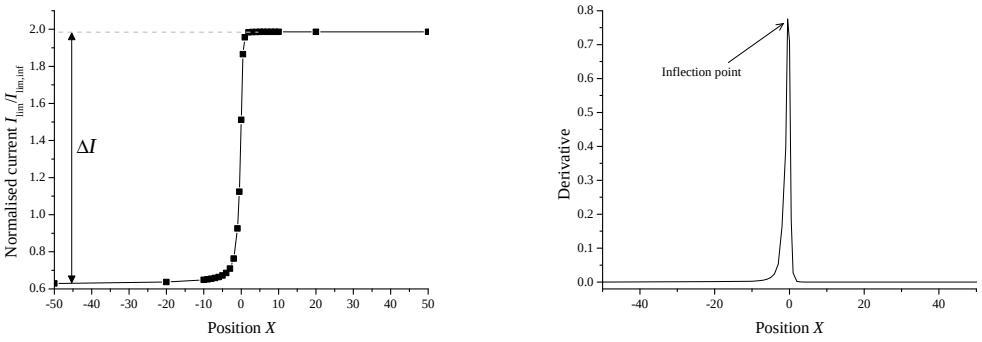

(a) Line scan for $H = 1$ and $R_g = 1.1$ at $L = 0.01$

(b) Derivative of the line scan in (a)

Figure 5.2: Line scan over the separation between an insulating region and a conducting region in (a) with its derivative in (b)

electrode, in theory to describe the distance to fully resolve an entirely conducting region. In practice, this distance seems to correspond to the distance to fully resolve within 10% of the limiting current of each region. Moreover, comparing the calculated resolution for two cases may be deceptive if the same X points are not used in both scans. Therefore care must be taken when comparing cases that the calculation parameters are the same.

5.3.2 Analysis of a line scan

A typical line scan over two adjacent region, one inert and the other conducting, is shown in figure 5.2. Over the insulating part of the substrate, negative feedback current are recorded; the diffusion layer is large and spread out. There is no increase in current until the probe is in proximity of the separation between the two regions. The normalised current then reflects the regeneration of species at the conducting region. The closer the electrode to the separation - i.e. the closer X is to 0, the faster the increase in current. This is expected as the availability of species to reduce at the electrode will improve. Once the tip is past the boundary, the current stabilises within a very short distance. This can be explained by considering the size of the diffusion layer: over the insulating regions, the diffusion layer is spread out and will cover a large region of the substrate. However as the probe approaches the conducting region, the diffusion

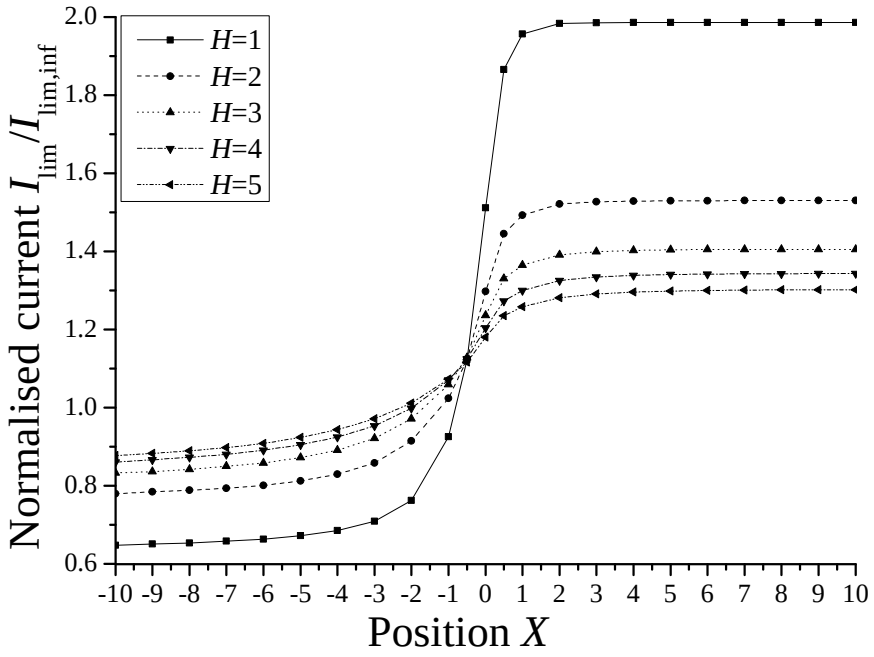

Figure 5.3: Line scans for different aspect ratios, for fixed insulation sheath thickness R_g=1.1 and at fixed height L=0.01

layer will be increasingly localised. This is will make the electrochemical radar less sensitive to its surroundings, and diffusion will thus no longer be hindered by the insulating region. This is reflected in the derivative of the line scan in figure 5.2(b) where the asymmetry of the line scan is highlighted.

5.3.3 Influence of the aspect ratio

The influence of the tip sharpness, characterised by the aspect ratio, was firstly investigated. The range of aspect ratios $H = 1$ to $H = 5$ was considered as this is the expected range of the electrode fabricated, and the range of validity of the expression derived for the limiting current in the bulk of the electrode. The results of the modelling of line scans are shown in figure 5.3. From the plots in figure 5.3, it can be observed that the gradients for $X < -3$ are the same for all aspect ratios. Only as X approaches 0 does the gradient become much steeper. The current difference between the insulating and the conducting region increases with decreasing aspect ratio, as a result of larger magnitude for less protruding electrodes. The difference between the different aspect ratios is

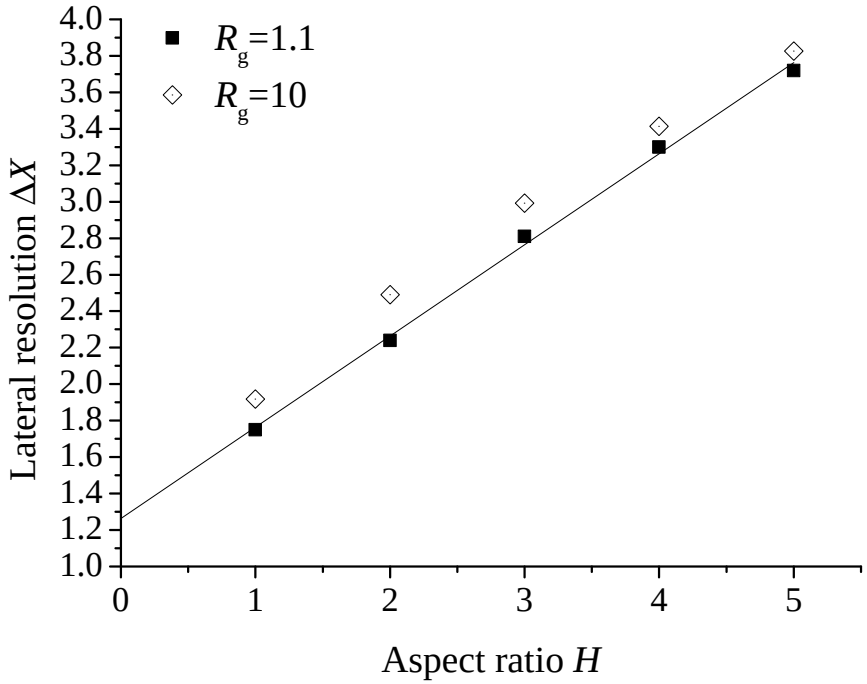

Figure 5.4: Plot of the lateral resolution ΔX, as a function of the aspect ratio H for two different insulation sheath radii at tip-substrate distance $L = 0.01$. The black line corresponds to equation 5.4

more evident over the conducting region. This can be explained by considering the concentration profiles of the probes over the different substrates. Over the conducting surface, there is a very large difference in the size of area occupied by the diffusion layer between the different aspect ratios. However, when scanning an insulating surface, there is less difference between the area occupied by the diffusion layer, as depicted in figure 5.5a. This is reflected in the line scans measured.

The resolution was calculated for each case for aspect ratio from $H = 1$ and $H = 5$. This revealed that the measured resolution distance for $H = 1$ is half the measured resolution distance for $H = 5$; the values characterising the resolution are proportional to the aspect ratio, as observed from figure 5.4.

The lateral resolution is proportional to the aspect ratio as demonstrated by the linear equation fitted to the data for $R_g = 1.1$, see equation 5.4.

$$\Delta X = 0.5H + 1.2636 \tag{5.4}$$

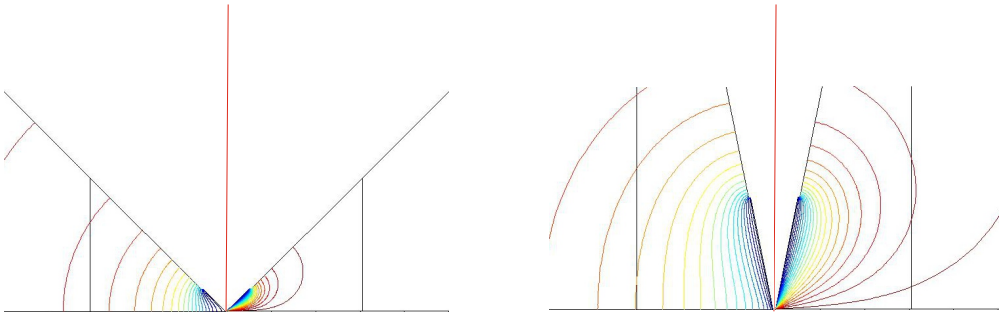

(a) $H = 1$ and $R_g = 1.1$ **(b)** $H = 5$ $R_g = 1.1$

Figure 5.5: Concentration profiles over an inert region (left) and conducting region (right) for a small aspect ratio in (a) and a large aspect ratio in (b) for which $R_g = 1.1$ and $L = 0.01$

There is a regularity in the increase in diffusion layer size with increasing aspect ratio and, due to the simplicity of the substrate studied, a regularity in the perturbation by the substrate. This is assumed to be the reason for the perfect linear relationship between the lateral resolution and the aspect ratio. The conclusions of the study confirm that a small aspect ratio would thus be more advantageous for higher resolution electrochemical scanning. the line had been extrapolated to determine the hypothetical resolution of the disc electrode, i.e. $H = 0$

The lateral resolution was also investigated for a range of aspect ratio with insulation sheath $R_g = 10$. The linearity is still observed, although the accuracy of the fitting equation such as the one derived in 5.4 is reduced. This is due to the larger insulation sheath thickness breaking the linearity of the concentration profile, thus causing the minor distortion observed in the data. The linearity should however return for very large insulation.

5.3.4 Influence of the insulation sheath thickness

The influence of the insulation sheath thickness was investigated previously, when looking at the influence of parameters on the resolution using approach curves, and it was determined that with respect to spatial resolution, the smaller aspect ratio gave better resolution than the large aspect ratio.

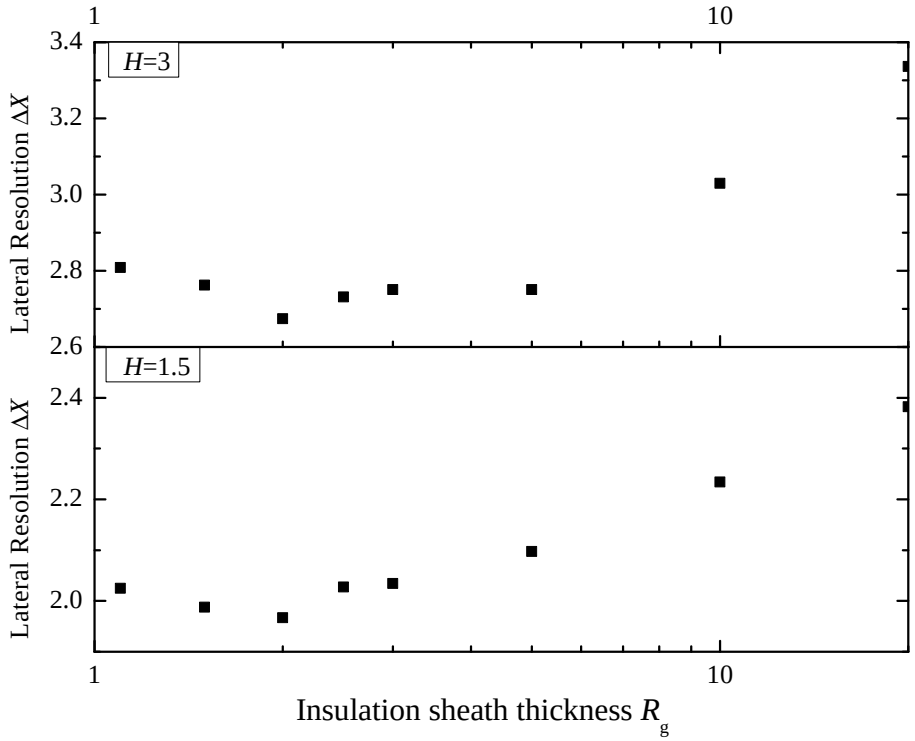

Figure 5.6: Lateral resolution as a function of the insulation sheath thickness R_g, for $H = 1.5$ and $H = 3$, at tip-substrate distance $L = 0.01$

A wider range of cases were considered for this study: (R_g = 1.1, 1.5, 2, 2.5, 3, 5, 10, 20) were modelled for different aspect ratios. Once again, line scans were generated over a substrate which was half insulating and half conducting and the resulting calculated lateral resolution can be seen in Figure 5.6, as a function of the aspect ratio.

This comprehensive study revealed that there was an optimum R_g. For very small insulation sheath thickness ($R_g < 2$), there is a large amount of back diffusion. This results in a loss of information, which is reflected in the line scan by the current difference between the current over the insulating substrate and over the conducting substrate: for an aspect ratio of $H = 1.5$, $\Delta I = 0.96$ for $R_g = 1.1$, $\Delta I = 1.01$ for $R_g = 1.5$, $\Delta I = 1.28$ for $R_g = 5$. For thick insulation ($R_g > 5$), the diffusion layer is spread out and it is observed that the current starts to increase from a further distance with large insulation. The resolution is best for an insulation thickness around twice the radius of the electrode. This is due to the insulation limiting the amount of back diffusion, whilst not significantly hindering the diffusion. Although an optimum R_g is evident, the difference

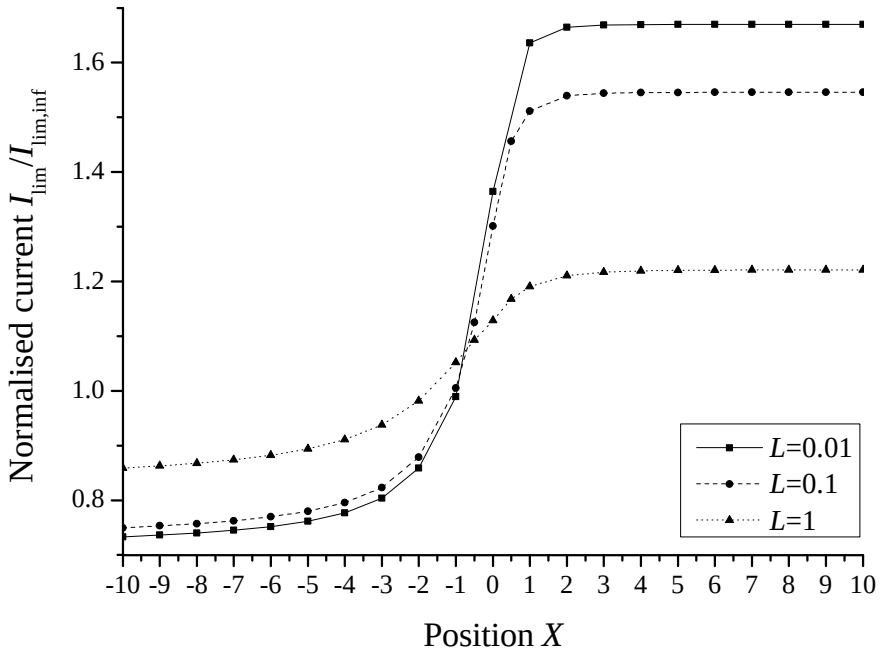

Figure 5.7: Line scans for a given tip with aspect ratio $H = 1.5$ and insulation sheath thickness $R_g = 1.1$ at different tip-substrate

between the resolution for insulation sheath thicknesses smaller than $R_g = 5$ is very small.

The regularity mentioned in the previous section as being responsible for the linear relationship between the lateral resolution and the aspect ratio is lost here: changing the thickness of insulation will have a noticeable effect on the shape of the diffusion layer and thus explains the optimum insulation sheath found. This is advantageous as it was expected that larger insulation sheath would be better for electrochemical measurement, which is in turn worse for AFM measurements. A thinner insulation layer is in fact ideal.

5.3.5 Influence of the tip-substrate distance

Line scans were generated for different tip-substrates distances, see figure 5.7, for each of which the resolution was calculated. Different heights confirmed, as expected, that the closer the probe to the surface, the better the resolution.

Plotting the resolution as a function the tip-substrate height revealed there was a linear relationship between the resolutions and the probe height. At a tip-substrate distance $L = 0.01$, the expected resolution for a tip with $H = 1.5$ and $R_g = 1.1$, is $\Delta X = 2.02$ compared to $\Delta X = 4.80$ at $L = 1$. This study also revealed that the influence of the tip-substrate distance L was more important over the conducting region, due to the size of the diffusion layer. Over an inert surface, the diffusion layer is very spread out and therefore bringing the probe closer would not affect the area occupied by the diffusion layer much. However over a conducting region, the closer to the surface the electrode is, the more localised the diffusion sphere, and this is reflected in the current measured.

5.3.6 Summary

The study of the influence of the insulation sheath thickness revealed that there is an optimum insulation sheath thickness, which will achieve the best resolution. With an insulation sheath radius $R_g = 2$, the diffusion layer of the electrode is blocked and directed towards the substrate. Back diffusion is limited. However the layer is not spread out as with large insulation sheath and as a result, an insulation sheath of approximately $R_g = 2$ will give the highest resolution. However this effect is minor and the main conclusion to extract from this is that a small insulation sheath, smaller than $R_g = 5$ will be ideal. The other two sets of simulations revealed that as expected, the closer the electrode is to the surface, the better the resolution, although quantification of the resolution showed that the resolution was not largely improve by bringing the tip-substrate distance from $L = 0.1$ to $L = 0.01$. The aspect ratio investigation confirmed that the smaller aspect ratio gave better resolution than the sharper tips. The effect of the aspect ratio is more important than the effect of the insulation sheath thickness.

5.4 The lateral resolution of defective tips

5.4.1 The blunt tip

The influence of a blunt tip was previously investigated, in the bulk. It is an unavoidable defect and currently a typical tip apex radius for a commercially available probe appears to be in the range of 7-12 nm. With this is mind, the bluntness was fixed at $a = 10$ nm radius. The study in the bulk revealed that for this size defect, tips with radii larger than 600 nm presented an error smaller than 1%. Tips for which $r_{\text{tip}} > 100$ nm will be within experimental error. However anything smaller and the current would be as much as 25% larger than the perfect tip current. Model line scans were therefore run for two tips $H = 1.5$ and $R_{\text{g}} = 1.1$ as well as $H = 4$ $R_{\text{g}} = 10$. Here the parameter of the defect, i.e. the radius of the tip apex a is fixed, and the radius of the electrode is varied from $r_{\text{tip}} = 500$, 100 and 50 nm. This was modelled using dimensionless units, thus resulting in varying dimensionless tip-curvature: $a = 0.02$ for $r_{\text{tip}} = 500$ nm, $a = 0.1$ for $r_{\text{tip}} = 100$ nm and $a = 0.2$ for $r_{\text{tip}} = 50$ nm.

As with the influence of the bulk, the smaller r_{tip} is, i.e. the smaller the electroactive area is, the larger the influence on the current of the defect. For the smallest tip, the positive feedback current is over twice the perfect tip value, as observed on figure 5.8. The line scans reveal that the influence of the defect is only noticeable over the conducting region. Indeed, over the insulating region, the relative difference between the current at the defective tips and the perfect tip is well within experimental error for $X < -0.5$. This is due to the size of the diffusion layer. If the case over the insulating region is considered, the diffusion layer is very spread out and this therefore minimizes the influence of the defect in comparison with the size of the diffusion layer. However over the conducting region, diffusion is very localized and the influence of the defect is maximized. Comparing the calculated resolution for the different defective tips, we observe that the larger the defect, the better the resolution. For $r_{\text{tip}} = 50$ nm, the calculated resolution was half the resolution of the perfect tip, meaning that half the distance is required to fully distinguish one region from the next. The

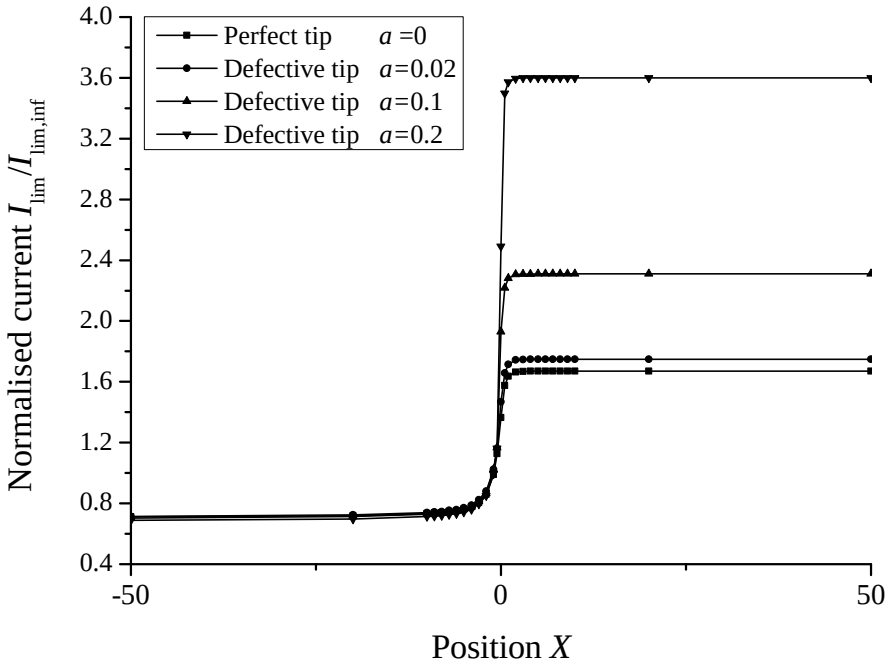

Figure 5.8: Line scans for a tip with $H = 1.5$ and $R_g = 1.1$ at L=0.01. The radius of curvature for the defective tips is set to 10 nm and the radius of the electrode is varied between 500 and 50 nm.

increase in current is also much larger which contributes to the high resolution. It can therefore be concluded that for electrochemical measurements, the bluntness of the tip is an advantage.

5.4.2 The insulation angle

The insulation angle is a defect that was shown to have little influence in the bulk, in particular its influence decreases with increasing insulation sheath thickness. Trends were however observed and it was shown that an increase in insulation angle resulted in a smaller current due to the increased hindering of diffusion, whereas a decrease in angle would result in an increase in current. Often the tip of the conical part is sharper than the rest of it, which means the insulation angle is larger than perfect. This was shown to be advantageous when studying the spatial resolution.

The calculated resolution for the perfect tip is $\Delta X = 1.78$. A defective tip with insulation angle $\beta = 20°$ is $\Delta X = 1.78$. There is therefore a negligible loss

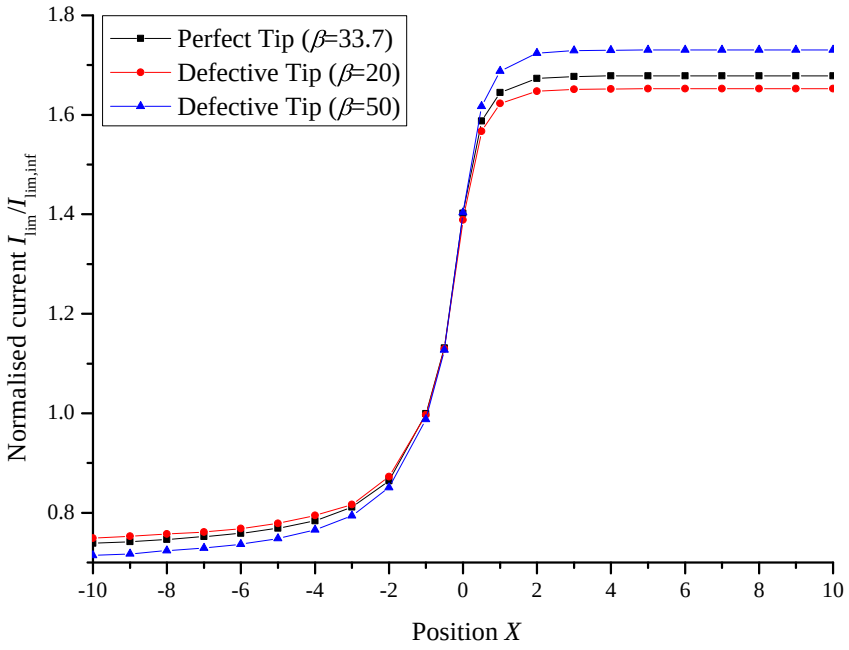

Figure 5.9: Line scans above two adjacent regions, insulating and conducting, for different insulation angle values, for a tip with aspect ratio $H = 1.5$ and $R_g = 1.1$ at $L = 0.01$.

in resolution for a decrease in angle. Moreover this is a tip with the smallest insulation angle possible and therefore this is virtually the worst case scenario. An increase in current, for e.g. $\beta = 50°$, the lateral resolution is $\Delta X = 1.90$. This is expected and mirrors the findings discussed previously. With regards to spatial resolution - or the ability to resolve a conducting region of a given size, a large insulation sheath radius was found to be advantageous. This was due to the diffusion layer being "directed" towards the substrate, resulting in larger contrast and bigger response to the conducting region. This was also the conclusion when studying the influence of the insulation angle. However, the lateral resolution does not only depend on the contrast observed but also on the gradient over the limit between the two regions and with respect to this parameter, the influence on the gradient of a more localised diffusion layer will exceed the influence of the conducting region on the current contrast. However overall, the difference is negligible. To put this into perspective: for a tip with r_{tip} and an angle of 50°, it would take an additional 12 nm to fully resolve an insulating region from a conducting region, compared to an electrode with angle 20°. The difference

between the three cases, observed in figure 5.9 is smaller over the insulating region than over the conducting region.

5.4.3 Summary

Two defects were investigated and their influence on the resolution quantified. The blunt tip was revealed to improve the resolution, thanks to the flattened plane at the end, up to doubling the resolution of the electrode for tip radii smaller than 50 nm. The insulation joining angle however was shown to have negligible influence on the lateral resolution. Other defects which should be investigated further are the case of an off centred tip and the presence of side walls. In the case of an off centred electrode, it would be interesting to investigate the influence of the position of the defects and how this influences the resolution. If the tip is positioned such that the smaller edge is at the 'front' when approaching the substrate boundary, the resolution will not be affected much. However in the opposite case, where the large insulation plane is at the 'front', the diffusion layer will be much more spread out towards the boundary and as a result, the increase in current will be less steep, resulting in a larger distance necessary to distinguish the conducting region form the insulation region, and therefore a worst resolution. In the case of side walls, when close to a surface, they may firstly collide with the surface and even if they do not, the wall will severely restrict diffusion to the tip. This is expected to be more of an issue with the inert substrate.

5.5 Simulation of a model substrate

A typical model substrate investigated with an electrode is a series on conducting lines embedded in an insulating matrix. With this is mind, simulations focussed on using line scans to once again evaluate the spatial resolution: what size is the smallest conducting line that will be distinguished? What is the narrowest insulating separation between two conducting lines for both lines to be individually resolved? How wide does a conducting line need to be for a fully conducting

current to be measured? Finally, what separation is necessary for full negative feedback to be reached? And how do geometrical parameters affect this?

5.5.1 The insulation sheath thickness

The effect of the tip-substrate distance on imaging was investigated by looking at the effect of varying this distance when modelling line scans over conducting lines of width 1, the same width as the electrode radius.

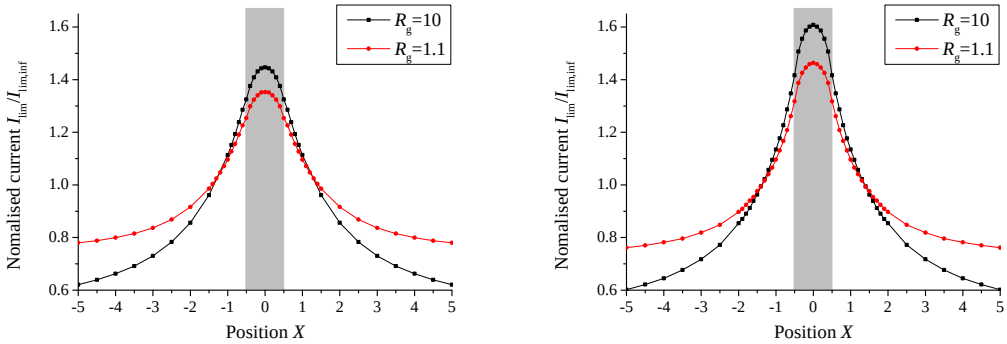

(a) $H = 1.5$ and $L = 0.1$ **(b)** $H = 1.5$ $L = 0.01$

Figure 5.10: Line scans over a conducting line of width 1, represented in grey for a cone with aspect ratio $H = 1.5$ and two different insulation sheath thickness $R_g = 10$ and $R_g = 1.1$ at a tip to substrate distance of $L = 0.1$ in (a) and $L = 0.01$ in right

When the sensitivity or spatial resolution of the electrodes was considered, it was shown that higher insulation sheath would be more favourable as back diffusion would be limited and the diffusion layer would be "pushed" towards the substrate and therefore when scanning vertically, this would be advantageous as the diffusion layer would be more heavily perturbed by the substrate. As a result, higher insulation sheath thicknesses exhibit higher contrast when approaching surfaces. However when considering the lateral resolution, previously in this chapter, an optimal sheath thickness was determined, which was around twice the radius of the electrode. This is because the lateral resolution does not simply take into account the current magnitude but also the distance necessary to resolve an insulating from a conducting region. The substrate considered here confirms this: the larger insulation sheath will have a larger increase in current over the conducting band than the smaller insulation sheath. However it is observed that

the increase begins at much smaller X than for the smaller aspect ratio, with the diffusion layer spreading further out for $R_g = 10$. This is important when scanning a surface, as if two adjacent conducting elements were to be scanned, they would not be as easily distinguished with a larger insulation sheath thickness.

5.5.2 The aspect ratio

The line scan over a conducting line of width 1 is shown for two different values of H, in figure 5.11. Until within $X = -2$ (and over $X = 2$ of the centre of the conducting line), the gradient of the curve during the scan is the same. This may be due to the linear relationship in aspect ratio, observed in section 5.3.3.

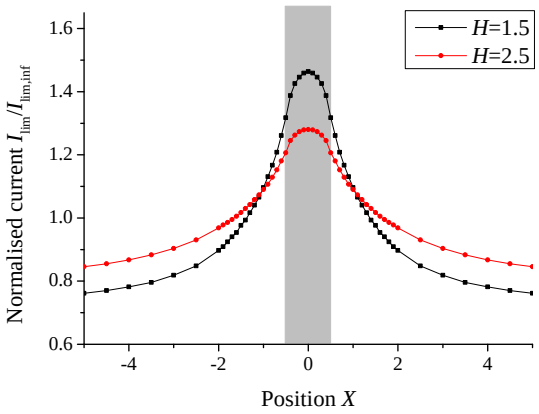

Figure 5.11: Line scans over conducting line of width 1, in grey, embedded in an insulating matrix, for varying H, a fixed insulation sheath raidus $R_g = 1.1$ at $L = 0.01$

5.5.3 The tip-substrate distance

Figure 5.12 shows two line scans for different tip-substrate distances. Over the insulating region, there is very little difference between the current at $L = 0.1$ and $L = 0.01$. The diffusion layer will not be much more spread out with the decreased distance, whereas the diffusion layer size will be decreased with decreasing L. Comparing the line scans between the two tip-substrate distances, as shown in figure 5.12, it is noticeable that the larger insulation sheath will also have a greater increase in current with decreasing tip-substrate distance than with the smaller insulation sheath.

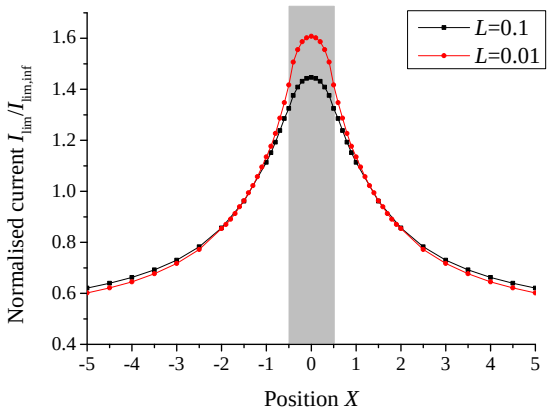

Figure 5.12: Line scans over a conducting line embedded in an insulating matrix for $H = 1.5$ and $R_g = 10$ at varying tip-substrate distances

5.5.4 The conducting line width

Simulated line scans over single conducting and insulating lines embedded in insulation and conducting matrices, respectively, were used to study the behaviour of the tips. Two tips were investigated: the first had a small aspect ratio and a small insulation sheath thickness ($H = 1.5$ and $R_g = 1.1$) which would have a good resolution, for a conical tip; the second was a low resolution tip (with respect to the electrochemical response) with $H = 4$ and $R_g = 10$. These lines are shown in figures 5.13 and 5.14.

The normalised current over an entirely inert substrate is around $I_{lim} = 0.73$ for the small aspect ratio tip at $L = 0.01$; as the tip moves along the X-axis and gets closer to the conducting line, the current begins to increase. The gradient increases with increasing proximity to the conducting line, but will never exceed the gradient of the line scan ranging from an entirely insulating to an entirely conducting region, as seen in the previous section. For the tips with small aspect ratio, the smallest line investigated had a width ten times smaller than the radius of the electrode so for example, if the tip had a radius $r_{tip} = 100$ nm, a conducting line of width 10 nm will result in a current 160% the limiting insulating current.

Note that initially, the increase in current is large and localised, whereas the larger the conducting line, the further away the increase in current is observed. As the width of the line increased, the current difference is larger although the

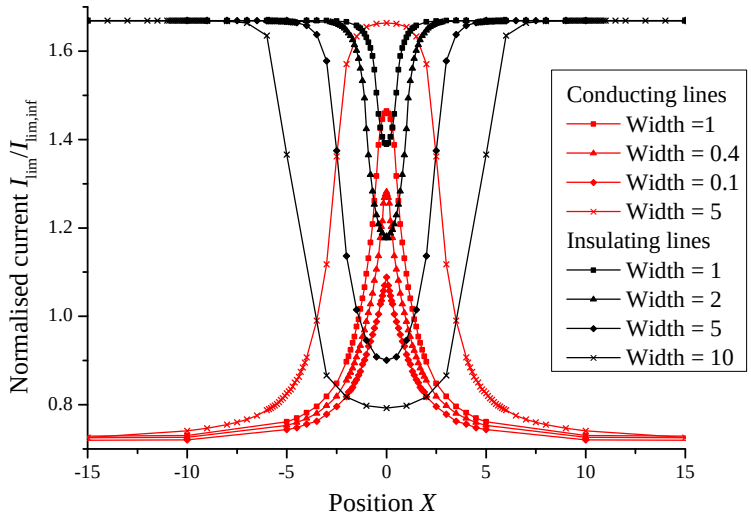

Figure 5.13: Line scans over insulating (black) and conducting (red) lines of different widths with a tip of dimensions ($H = 1.5$ and $R_g = 1.1$) at $L = 0.01$

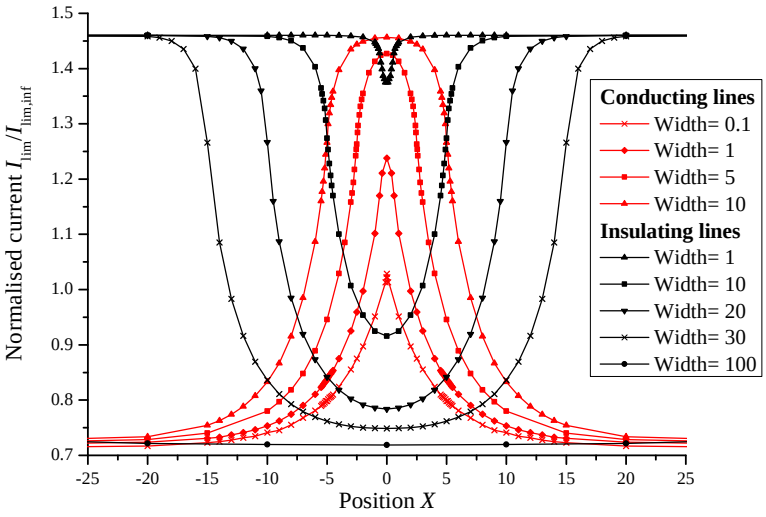

Figure 5.14: Line scans over insulating (black) and conducting (red) lines of different widths with a tip of dimensions ($H = 4$ and $R_g = 10$) at $L = 0.01$

increase in current is more spread out, due to increased availability of species to react. Lines of width five or more times the radius of the electrode will exhibit fully conducting current for small aspect ratio. For the high aspect ratio tip, only a substrate line larger than ten times the radius of the electrode will have current reaching infinite substrate current.

The case of an insulating band embedded in a conducting matrix was also considered, for both tips. The contrast is much worse in this case. Only a line larger than the tip radius will cause hindering of diffusion large enough for the relative difference to be larger than 5% and thus be considered distinguishable. Only for very large insulating lines will current be achieved as if over an entirely inert substrate. This is due to the size of the diffusion layer: over an inert substrate, the diffusion layer is very spread out and will be influenced by the conducting matrix on either side. Note that this is amplified by the use of steady state conditions, as transients would reduce the effect slightly.

The concentration profiles in figure 5.15 show the influence of a line -conducing or insulating- embedded in a matrix. For the concentration profile of a tip above the inert line, embedded in an insulating matrix, there is not a great change observed in the diffusion layer size, resulting in very little change measured in the current, compared to the full positive feedback case. Only for larger lines will be the hindering of diffusion by the inert line be significant enough for the tip to detect the insulating line. On the contrary, conducting lines will have a much larger influence on the diffusion to the electrode, hence the larger contrast. The size of the diffusion layer is greatly reduced by the source of species at the substrate.

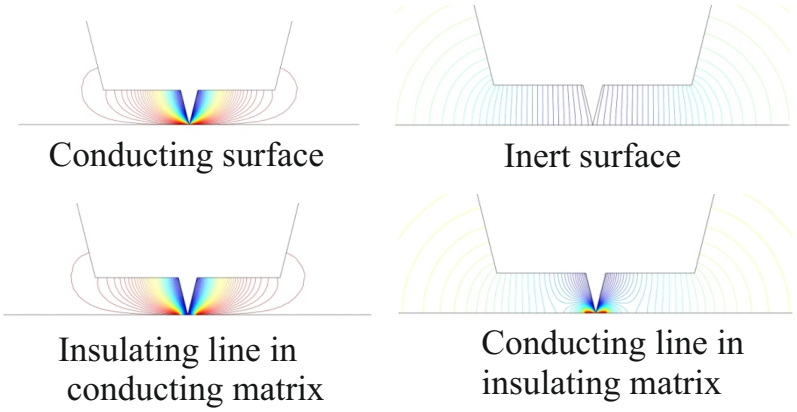

Figure 5.15: Concentration profiles for $H = 1.5$ and $R_g = 10$ over four different substrates, to investigate the influence of the substrate on the diffusion layer size

5.6 Conclusion

In order to determine the ideal tip geometry for the AFM-SECM probe fabricated, a study of lateral resolution was performed to complement the spatial resolution presented in the previous chapter. The two aspects of the geometry of the cone were investigated, as well as the tip-substrate height. It was revealed that with respect to the aspect ratio, the less protruding tips were favourable, with high aspect ratio cones ($H = 5$) requiring almost twice as long a distance to fully resolve an insulating from a conducting region. The existence of an optimal radius of insulation was determined, around twice the radius of the tip, wide enough to 'focus' the diffusion layer onto the surface but not so thick as to spread out the layer too much. The tip-substrate distance was studied and it was shown that this had more of an effect over the conducting region. In fact, there was little difference between $L = 0.01$ and $L = 0.1$ over the inert region of the substrate. Two defects were also investigated: the tip bluntness, unavoidable, was shown to work in favour of high resolution mapping, and the insulation angle, which was proven to be negligible. The simulation of a model substrate, made of conducting lines, embedded in an inert matrix was explored to look further into the influence of the geometry. The issue of spatial resolution and lateral resolution were mixed when investigating this substrate and revealed the capabilities of conical electrodes.

The method used here to calculate the resolution, first introduced by Wittstock,[137] is a good method as it enables comparison of different cases taking into

account the parameters affecting the resolution: the current different between the insulating region and the conducting region, and the gradient of the curve. However the major inconvenience of the method is that the resolution calculated depends greatly on the sample points chosen along the line scan. If very close sampling points were used, the resolution calculated would tend towards a fixed value. However with each point needing a 3D simulation, which could take up to three hours to solve, it was not possible to use a sufficient number of points. As a result, care was needed to ensure points used were the same for cases compared. As the aim of this section is to determine an optimum geometry, as in the geometry that would give the best resolution, this method was very useful. However the results obtained cannot be compared to other work. Another possible method is to calculate the increase in current and compare this to the fully insulating and conducting current. The distance to fully distinguish an inert region from a conducting one would then be estimated from the point at which the current was 5% (if this was the desired threshold) larger than the current over the inert region to within 5% of the fully conducting current. This would then also reflect the asymmetry of the line scan. Future work would use this method to analyse the line scan data available. From this analysis, attempts would be made to derive a method to determine the position of the separation between the inert and conducting region from the line scan. This would enable users of conical tips to extract the region boundary using an experimental line scan.

Chapter 6

Extracting information from SECM experiments

6.1 Introduction

In scanning electrochemical microscopy, the tip is generally used to gather information about a substrate. It is however also possible to reverse this and use approach curves to extract information about the tip electrode. Both these aspect will be investigated in this chapter. In the first section, positive and negative feedback curves will be generated for a wide range of geometries to enable the fitting of equations to the data. Guidelines will be developed for users to refer to. In the second part, approach curves are used to study substrates with finite kinetics. By studying these, we aim to derive a method for users to be able to extract kinetics from their experimental data.

In both sections of this chapter, approach curves will be generated for different geometries and different substrate rate constants, the details of the simulation are presented next.

6.2 Details of the simulation

Diffusion only conditions were assumed for mass transport in solution and the steady state equation was solved both in 2D and 3D. The geometry of the elec-

troactive probe is described by three parameters: the radius of the electroactive cone r_{tip}, the height of the electroactive cone h_{tip} and the radius of the insulation r_{g}. The problem was cast into dimensionless quantities by dividing distances by the radius of the electrode and concentrations by the bulk concentration and so on, as mentioned in chapter 3. The geometry of the electrode was thus only described by two dimensionless parameters: the aspect ratio $H = {}^{h_{\text{tip}}}/_{r_{\text{tip}}}$ and the insulation sheath radius $R_{\text{g}} = {}^{r_{\text{g}}}/_{r_{\text{tip}}}$.

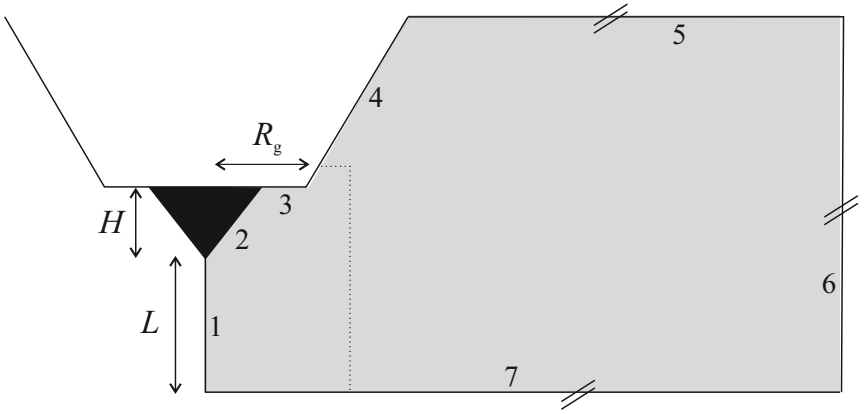

Figure 6.1: Schematic representation of the simulation domain in light grey, with the tip described by R_{g}, R_{tip} and H, at a varying tip-substrate height L

The dimensionless concentration is $C^{\text{b}} = 1$ and the dimensionless diffusion coefficient is 1 in the entire domain; the boundary conditions also remain the same as previously, for the most part: $C = 0$ at the electrode, $C = C^{\text{b}}$ at the domain boundaries and no flux at the insulation boundaries. In this model, however at the substrate, ${}^{\partial C}/_{\partial Z} = \Lambda(1 - C^{\text{b}})$, for $\Lambda = {}^{k * r_{\text{tip}}}/_{D}$ where k is the rate constant for the reaction occurring at the surface and D is the dimensional diffusion coefficient. To recreate an insulating substrate, the rate constant is set to $\Lambda = 0$, whereas setting Λ to very large value (here $\Lambda = 10000$) will recreate a fully conducting boundary condition. 2D axisymmetric approach curves were used to verify the accuracy of this method.

Two tip geometries were investigated: the first tip $H = 1.5$ and $R_{\text{g}} = 1.1$ and the second $H = 4$ $R_{\text{g}} = 10$. Approach curves were generated over an insulating and a conducting substrate using both methods, the first being defining the substrate boundary as $C = 1$ for a conducting surface and *no flux* for an inert surface

and the second method being defining the boundary using the rate of electron transfer at the surface. It was found that the approach curves were within 0.01%. With the method validated, we were able to model approach curves with a single loop code, which iteratively varied the Z-position of the substrate relative to the electrode.

The second part of the work the modelling of line scans over regions of different kinetics, in 3D was done by describing the substrate as a map of rate constant and importing this as a boundary condition, as described in chapter 5, although the rate constant Λ will be varied from $\Lambda = 0$, an inert substrate, to $\Lambda = 10000$, a fully conducting substrate.

6.3 Extracting tip geometry from SECM approach curves

6.3.1 Shape characterization in SECM

In chapter 1, the different electrode geometries (disc, cone, ring ...) were presented along with the theoretical study of their geometry, in particular the influence of the electrode shape and its different parameters on measurements both in the bulk and when scanning a surface. The knowledge of the influence of these parameters may be used to determine the ideal tip geometry. Moreover, users may be able to extract information about the tip geometry from measurements, thanks to numerical simulations. Indeed, the steady state limiting current is not sufficient to determine the geometry of even the simplest electrodes such as the disc, if no previous knowledge is assumed. For a disc, there would be two unknowns: the tip radius and the insulation sheath thickness. An 'apparent' or 'effective' tip radius can be determined from the steady state limiting current, and reveal no information about the insulation sheath. An SECM experiment, typically an approach curve, would allow the determination of the insulation sheath thickness, but this is extremely difficult due to the dependence of the x-axis on the radius of the electrode. Once this is known, the limiting current can once again be used to determine the actual electrode radius. Generally, as with the

conical electrodes, it is necessary to know the radius of the electrode to enable fitting of the approach curves. In this chapter, expressions will be derived for positive and negative feedback approach curves for conical electrodes with conical insulation, for users to extract information from. Simple steps will be given for users to refer to, which will enable them to determine the electrodes geometry.

6.3.2 The simulated positive and negative feedback approach curves

Positive and negative feedback approach curves were presented and analysed in chapter 4. The geometrical parameters of the conical electrode was varied and for each, approach curves over a conducting surface ($\Lambda = 10000$) and inert surface ($\Lambda = 0$). These curves frame the range of cases encountered for different rate constants. A selection of the approach curves can be seen in figure 6.2. It has been highlighted that there is no expression to predict these equations, like there is for disc electrodes, which is why we aimed to derive one in this work.

Approach curves were generated for aspect ratio from $H = 1$ to $H = 5$ with increments of 0.1 and a large range of different insulation sheath thicknesses from $R_g = 1.1$ to $R_g = 100$, see figure 6.2. The two cases clearly summarise the influence of the two geometrical parameters, already discussed in chapter 3. For the insulation sheath thickness: the larger the insulation sheath, the more spread out the diffusion thus increasing the magnitude of the response both for positive and negative feedback, although the difference is less noticeable over the conducting surface. Secondly, there is less contrast with the larger aspect ratio.

6.3.3 Approach curves for all tip-substrate distances

Fitting a single expression to the data, which would take into account all the parameters (aspect ratio, insulation sheath thickness and tip-substrate distance) has so far been unsuccessful due to the amount of parameters to take into account which are moreover varied over a wide range.

The large amount of data produced (thousands of individual simulations) can now be used to derive an expression for the positive and negative feedback

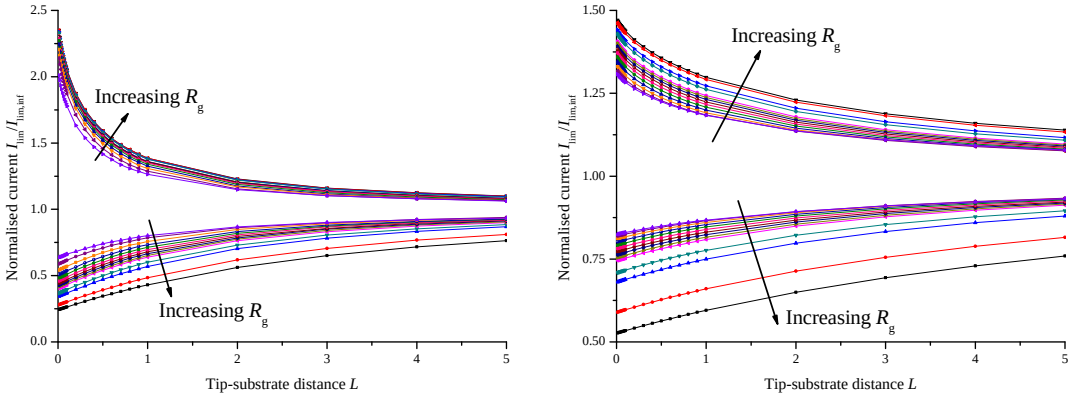

(a) $H = 1$ **(b)** $H = 5$

Figure 6.2: Positive and negative feedback curves for tips with aspect ratio $H = 1$ in (a) and $H = 5$ in (b) for insulation sheath thicknesses ranging from $R_g = 1.1$ to $R_g = 100$

approach curves as a function of the geometrical parameters of the electroactive probe, i.e. the aspect ratio H and the insulation sheath thickness R_g. The limitation of this approach is the number of parameters and the complexity of the equation fitted. As a result, equation 6.1 was derived first, valid for tip-substrate distances L=0.01 to 100, in the bulk, and for discrete combinations of geometrical parameters. This expression, in combination with table 6.1 for positive feedback and table 6.2 for negative feedback will enable users to generate approach curves, valid within 1% of the simulated results.

$$\frac{I_{\text{lim}}}{I_{\text{lim,inf}}} = a * exp^{-L/b} + c * exp^{-L/d} + f \tag{6.1}$$

where $I_{\text{lim,inf}}$ is the limiting current in the bulk.

Substituting these constants into equation 6.1 will give approach curves from very near the surface to in the bulk. However for a more accurate fit, two expressions were derived for positive and negative feedback valid over a shorter tip-substrate distance range but that takes into account both the insulation sheath and the aspect ratio of the conical tip.

Table 6.1: Constant to input into equation 6.1 to generate positive feedback approach curves for conical electrodes with conical insulation

R_g	Constant	$H = 1$	$H = 2$	$H = 3$	$H = 4$	$H = 5$
20	a	0.9951	0.9936	0.9944	0.9942	0.9937
	b	-0.1893	-0.3247	-0.2550	-0.2073	-0.1746
	c	7.6256	1.9612	2.2056	2.3965	2.5597
	d	-0.4644	-0.1722	-0.1556	-0.1461	-0.1385
	f	1.7299	8.2301	9.3392	10.2016	1.0001
10	a	0.9905	0.9937	0.9945	0.9944	0.9941
	b	-0.4293	-0.2920	-0.2178	-0.1726	-0.1418
	c	1.4374	1.6457	1.8285	1.9860	2.1224
	d	-0.1596	-0.1307	-0.1189	-0.1114	-0.1068
	f	6.7851	7.9305	9.0097	10.0121	10.8358
5	a	0.9917	0.9939	0.9945	0.9943	0.9942
	b	-0.3772	-0.1087	-0.0987	-0.1340	0.0908
	c	1.1838	7.7287	8.9401	1.6954	10.9806
	d	-0.1360	-0.2369	-0.1710	-0.0940	-0.1112
	f	6.3650	1.3556	1.5353	9.9917	1.8527
1.1	a	0.9883	0.9942	0.9938	0.9938	0.9936
	b	-0.1143	-0.1524	-0.1131	-0.0973	-0.0835
	c	6.6392	1.2614	1.4667	1.6687	11.9966
	d	-0.2386	-0.0908	-0.0867	-0.0847	-0.0851
	f	1.0006	8.7816	9.8535	11.0210	1.8496

6.3.4 An expression for approach curves towards inert surfaces

To derive the expression for negative feedback, the current was plotted as a function of tip-substrate distance for all conical geometries. An expression of the form $A - BC^L$ was found to give the best fit, of all the expressions investigated. The three constant A, B and C were then plotted against the insulation sheath thickness and expressions were once again found to fit the data. Finally, the same step was repeated for constants A_i, B_i and C_i to which polynomial functions were fitted.

The following equation has been derived to calculate the current at a conical electrode as a function of the geometry of the cone (H and R_g) as well as the tip-substrate distance L when approaching an inert surface:

$$\frac{I_{\text{lim}}}{I_{\text{lim,inf}}} = exp\left[A_1 + A_2 R_g\right] - exp\left[B_1 + \frac{B_2}{R_g + B_3}\right]\left(C_1 - C_2 C_3^{R_g}\right)^L \qquad (6.2)$$

Table 6.2: Constant to input into equation 6.1 to generate negative feedback approach curves for conical electrodes with conical insulation

R_g	Constant	$H = 1$	$H = 2$	$H = 3$	$H = 4$	$H = 5$
	a	1.0308	1.0234	1.0180	1.0148	1.0130
	b	0.7315	0.3818	0.2676	0.2323	0.2097
20	c	0.2297	0.4152	4.9450	6.1792	0.8976
	d	0.5777	0.3549	0.2962	0.2456	0.2142
	f	2.0508	3.4484	0.6182	0.7759	7.1126
	a	1.0237	1.0208	1.0181	1.0149	1.0129
	b	0.5834	0.3493	0.2695	0.2151	0.1876
10	c	1.9089	0.3759	0.5652	5.3598	6.4706
	d	0.7024	0.3662	0.2670	0.2313	0.2024
	f	0.2214	2.9774	4.1307	0.7411	0.8799
	a	1.0235	1.0200	1.0171	1.0138	1.0120
	b	0.5777	0.3373	0.2282	0.2208	0.1894
5	c	1.7426	2.7025	3.9251	0.7326	0.8592
	d	0.6743	0.3323	0.2579	0.1756	0.1540
	f	0.2145	0.3624	0.5537	5.4127	6.6672
	a	1.0201	1.0189	1.0154	1.0123	1.0111
	b	0.4194	0.2727	0.1686	0.1858	0.1323
1.1	c	1.9118	0.3730	4.8194	0.7676	7.7695
	d	0.5744	0.2425	0.2169	0.1416	0.1605
	f	0.2231	3.0680	0.5889	6.5601	0.8921

$$A_1 = -0.0573$$
$$A_2 = -0.0014$$

$$B_1 = 0.0178H^2 - 0.2181H - 0.2562$$
$$B_2 = -3.4791H + 1.1890$$
$$B_3 = 2.4107H - 0.4108$$

$$C_1 = -0.0047H^2 + 0.0585H + 0.6341$$
$$C_2 = -0.0209H + 0.2984$$
$$C_3 = -0.0009H^2 + 0.0120H + 0.9284$$

This equation is valid within 2.5% for all insulation sheath radii smaller than $R_g = 20$ and from tip-substrate distance $L = 0$ to $L = 5$. The fit to simulated results is on average 0.5%. By adding a quadratic term to the first part of equation 6.2, i.e. from $exp\left[A_1 + A_2 R_g\right]$ to $exp\left[A_1 + A_2 R_g + A_3 R_g^2\right]$, where $A_3 = 6\text{x}10^{-6}$,

the expression can be extended to insulation sheath radii of up to $R_g = 100$ to an accuracy within 5%.

A plot of the comparison between the current derived by simulation and the current calculated using the expression derived above, see equation 6.2 is shown in figure 6.3. This plot highlights the strength of the fit: the expression is more

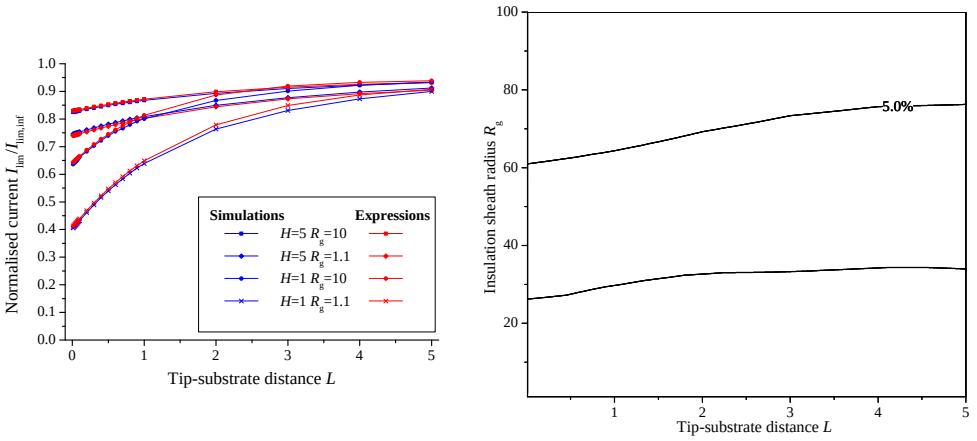

(a) Simulation vs. expression **(b)** Countour plot of the error in fit

Figure 6.3: Comparison between the simulated current and the theoretical current: in (a) for four specific cases with ranging insulation sheath thickness and for two different aspect ratios H; in (b) a contour plot of the relative difference as a function of insulation sheath thickness and tip-substrate distance, valid for $H = 2$ to $H = 5$, showing the lines for 1% and 5%

accurate for higher aspect ratios, and also more accurate for the shorter tip-substrate distances ($L < 1$). The contour plot presented in figure 6.3(b) represents the error of the expression derived, also known as the relative difference between the two currents. This has been plotted for aspect ratios from $H = 2$ to $H = 4$. This reveals that the expression is very accurate for all insulation sheaths. For the smallest aspect ratio, the accuracy is not as good for small insulation sheath thicknesses and small tip-substrate distances although it will still be well within 2.5% for $R_g < 2.5$; this is confirmed by the plot in figure 6.3 which shows that the curves are in agreement and will certainly enable an accurate comparison with experimental data.

6.3.5 An expression for approach curves towards conducting surface

An expression to describe the current above a conducting surface was derived using the same steps as for the negative feedback expression, using the thousands of simulations generated:

$$\frac{I_{\mathrm{lim}}}{I_{\mathrm{lim,inf}}} = exp\left[A_{\mathrm{a}} + \frac{A_{\mathrm{b}}}{R_{\mathrm{g}} + A_{\mathrm{c}}}\right] + \left(B_{\mathrm{a}} + \frac{B_{\mathrm{b}}}{R_{\mathrm{g}} + B_{\mathrm{c}}}\right) atan(L)^{\left(C_{\mathrm{a}} - C_{\mathrm{b}} C_{\mathrm{c}}^{R_{\mathrm{g}}}\right)} \tag{6.3}$$

$$A_{\mathrm{a}} = 0.3914 + 1.5010(0.3822^{H})$$
$$A_{\mathrm{b}} = -0.1983H + 0.0481$$
$$A_{\mathrm{c}} = 0.0797H^2 + 1.0221H - 1.1787$$

$$B_{\mathrm{a}} = -0.2413 - 3.6992(0.3014^{H})$$
$$B_{\mathrm{b}} = 0.0163H + 0.1378$$
$$B_{\mathrm{c}} = 0.0618H^2 + 0.2494H - 0.8115$$

$$C_{\mathrm{a}} = -0.0261H^2 + 0.3168H + 0.0828$$
$$C_{\mathrm{b}} = 0.1188 - 0.1740(0.3708^{H})$$
$$C_{\mathrm{c}} = -0.0095H^2 + 0.1026H + 0.6160$$

This expression is valid for aspect ratios ranging from $H = 1$ to $H = 5$, insulation sheath thicknesses from $R_{\mathrm{g}} = 1.1$ to $R_{\mathrm{g}} = 100$ and $L = 5$ to $L = 0.01$ within 3.4% and the fit is on average accurate to 0.7%. The fit will be within 2.6% for tip-substrate distances below $L = 3$. Four approach curves have been plotted both for the simulated case and the expression to show the fit, see figure 6.4. There is good agreement for all tip-substrate distances, although the smaller the distance the better the fit. Moreover, lower aspect ratios exhibit higher accuracy.

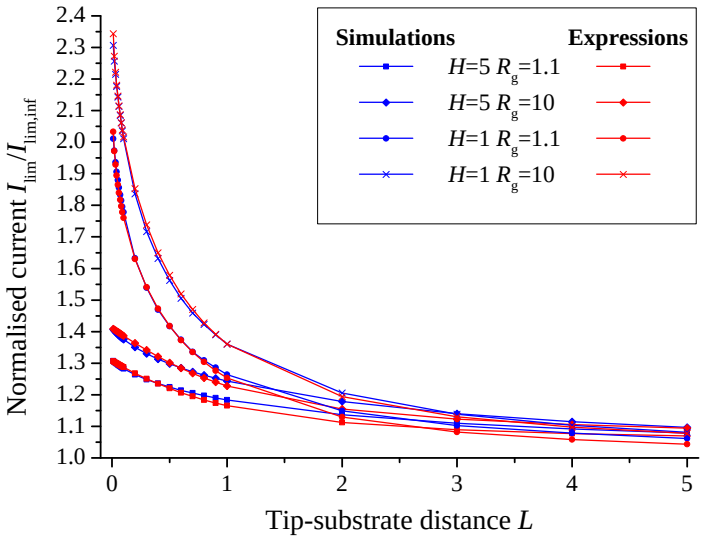

Figure 6.4: Comparison between the simulated approach curve and the approach curve for four different approach curves

6.3.6 Determining the geometry from positive and negative feedback curves

With the approach curves for positive and negative feedback generated, it is important to devise a method for users to fit these to experimental results. Consider a user having generated two experimental approach curves, one over an inert surface, the other over a conducting surface. The aim is to determine what the geometry of the conical tip is, using these two approach curves, as well as the limiting current in the bulk. The plot seen in figure 6.5 can be used to estimate the dimensions of the conical electrode.

The plot shown in figure 6.5 is not an approach curves. It presents the range of normalised currents expected between $L = 0.1$ and $L = 0.01$ for the aspect ratio specified on the x-axis, for all insulation sheath thicknesses. A current of around 2 over a conducting surface, for small L is observed for the positive feedback curve. This will give a definite indication that the aspect ratio will be close to $H = 1$ and have a small R_g. Mostly, cases will be more complicated: it is obvious on this plot that higher aspect ratios have less distinguishable current. However a combination of the both positive and negative feedback may give a clearer estimate: a current of 0.7 over an inert surface could be any aspect ratio

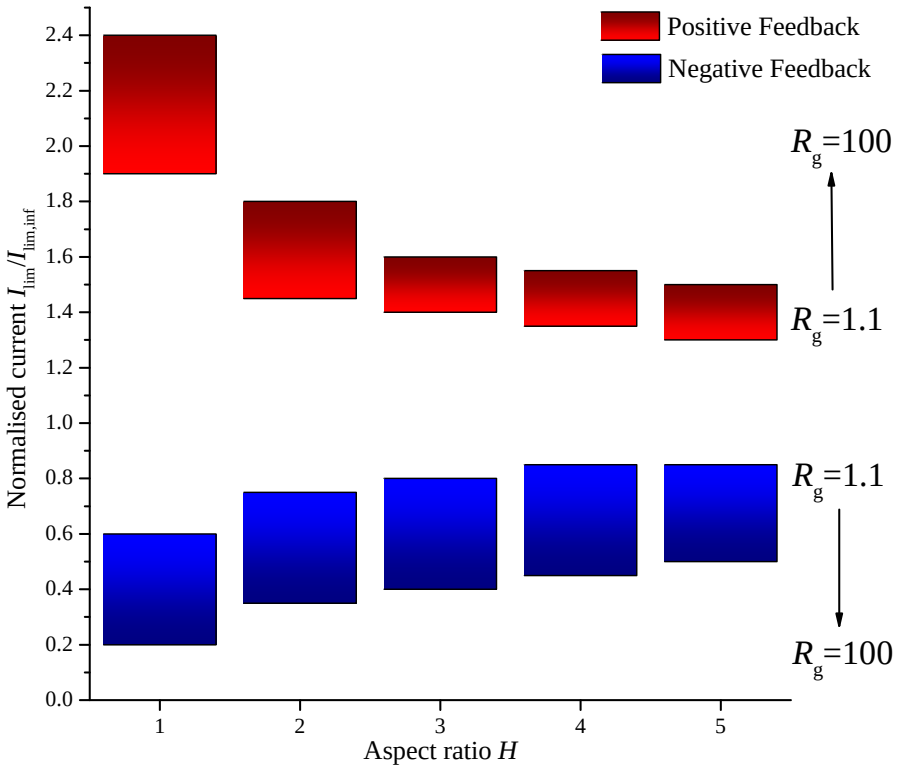

Figure 6.5: Histogram of the current range possible, as a function of the aspect ratio, for both positive (red) and negative feedback (blue) for all insulation sheath thicknesses from $R_g = 1.1$ to $R_g = 100$.The ranges shown are valid for distances from $L = 0.1$ to $L = 0.01$.

from $H = 2$ to $H = 5$ but will always be a small insulation sheath thickness. A positive feedback current of 1.6 could then be $H = 2$ to $H = 3$. However as we know the tip presents a thin insulation sheath, the aspect ratio must be $H = 2$. The advantage of this plot is that the range presented is valid for $L = 0.1$ to $L = 0.01$, so that an approximation can be made from the last few points of any experimental curve.

The aim of this is to then simplify the fitting of the expression to the experimental data: fewer cases have to be investigated if an approximate value is known for both R_g and H. When fitting, it is important to know how the geometry affects the shape of approach curves. The current at tips with smaller aspect ratios will initially decrease less than with larger aspect ratios, as the diffusion layer is smaller. However once close to the surface, the contrast is much higher for the smaller aspect ratios, and the decrease in current will be sharper. The insulation sheath thickness will not affect the gradient of the approach curve much, simply

the magnitude of the current. In particular at small tip-substrate distances, the curves for the same aspect ratio but varying insulation sheath thickness R_g appear parallel. When fitting theoretical curves to the data: if the steepness of the curve needs changing for better fit, the aspect ratio should be varied whereas if the magnitude of the current does not fit, the insulation sheath thickness should be addressed.

6.4 Extracting kinetics from SECM approach curves

Scanning electrochemical microscopy can be used to map kinetics from a surface of interest: by scanning the tip over the substrate, the reactivity will be imaged. However to extract the kinetics from this, approach curves must be used. The tip can be positioned over a specific region, preferably large enough that the surrounding matrix does not affect the tip current, and an approach curve generated. Fitting the experimental approach curve with a theoretical model will enable the user to determine what the rate constant is for the chosen (X,Y) point and therefore that region. The theory of finite kinetics is firstly presented, followed by the approach curves generated.

6.4.1 Literature of kinetic studies using microelectrodes

Scanning electrochemical microscopy has, from very early on, been used to measure the kinetics at the electrode. In 1992, Wipf *et al.* used the Fe^{3+}/Fe^{2+} couple in sulphuric acid to study irreversible reaction at the electrode.[68] Approach curves for different substrate potentials were performed and exhibited a mixture of negative and positive feedback, 'framed' by the full positive and negative feedback curves. Reaction rates from one extreme to the other were investigated and could be used for extraction of kinetics until the relevant simulations could be derived. A expression was fitted to the data a few years after,[139] and has since been reworked to provide more accurate results both for the faster electron transfer[121] as

well as for all cases, thanks to the improvement computer power.[38] Expressions were also derived for more complex systems such as enzymatic kinetics.[124]

These studies were performed for disc electrode. There has been no mention in the literature of these expressions being derived for conical electrodes, which is what will be presented in this chapter. The aim is to model approach curves for different tip-geometries (varying both H and R_g), for different substrate kinetics, and from this, derive expression for users to apply.

6.4.2 Determining rate constant using SECM approach curves

As mentioned above, approach curves were modelled for different rate constants, such as shown in figure 6.6. The cases are bounded by the two extremes of positive and negative feedback. In between, the curves are either always increasing, when Λ is large, decreasing, when Λ is small or a hybrid of both behaviours, although this is only truly observed for small H. This makes the fitting a rather difficult process. Plots such as the ones shown in figure 6.6 were generated for a wide range of tips with aspect ratios ranging between $H = 1$ and $H = 5$ and insulation sheath thicknesses between $R_g = 1.1$ and $R_g = 10$. It is worth remembering that each point of the plot shown in figure 6.6 is an individual simulation, the number totals around 18 000 for this study.

From these thousands of simulations produced, the intention was to derive an expression capable of predicting the current at the electrode during approach curves over surfaces of finite kinetics. This work is still ongoing, with the closest fit of an expression resulting in a fit with relative difference up to 10%. The difficulty here is mainly the need to take into account the tip-substrate distance, the rate of electron transfer as well as the two parameters describing the tip-geometry, H and R_g. Until a more accurate expression is derived, users will need to rely on the approach curves presented in figure 6.6.

For small aspect ratio tips, electron transfer rates larger than $\Lambda = 100$ will behave as though the system is diffusion limited. However with larger aspect ratios,

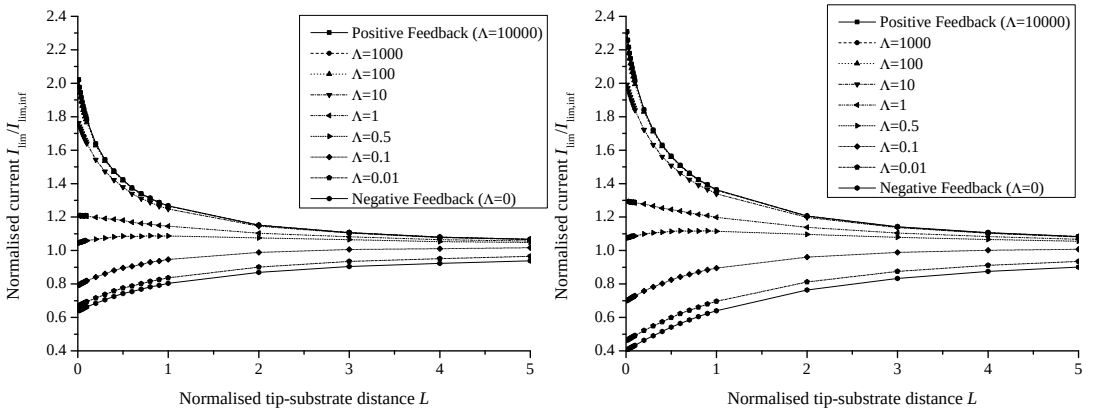

(a) $H = 1$ $R_g = 1.1$ **(b)** $H = 1$ $R_g = 10$

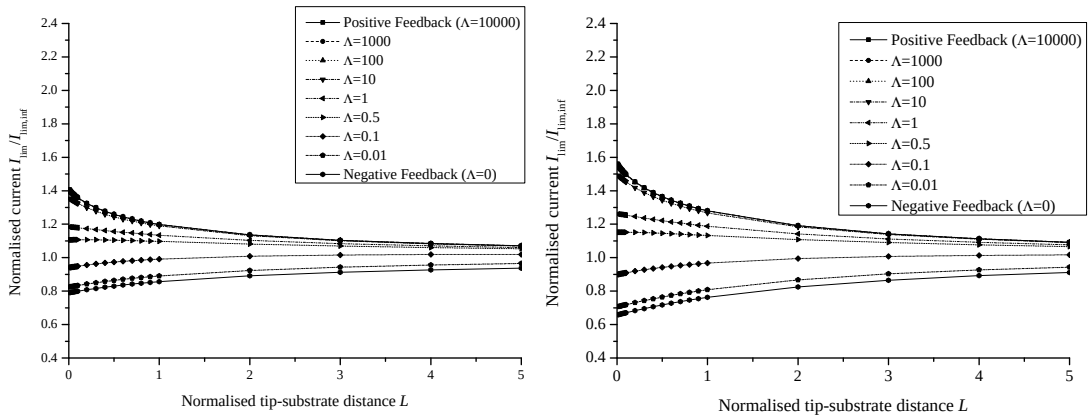

(c) $H = 3$ $R_g = 1.1$ **(d)** $H = 3$ $R_g = 10$

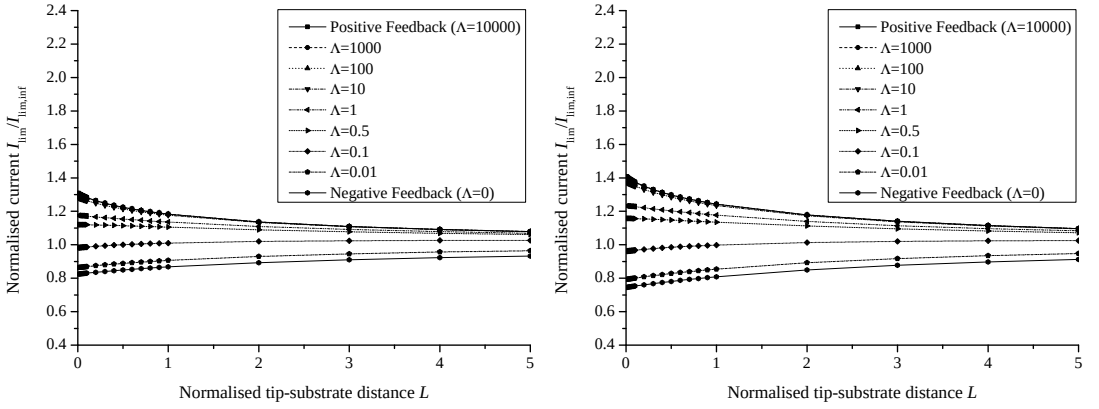

(e) $H = 5$ $R_g = 1.1$ **(f)** $H = 5$ $R_g = 10$

Figure 6.6: Approach curves for different tip geometry (H and R_g) and a range of electron transfer rate constants Λ.

the diffusion limited case will be for $\Lambda = 10$ and above. For $H = 1$, the current for $\Lambda = 10$ will be within 10% of the fully conducting current for tip-substrate distances down to $L = 0.05$ and within 15% overall.

An easy way of estimating the possible range of rate constants is to use the rate for which there is little change in the current throughout the approaching scan. For $H = 1$, the curve for $\Lambda = 0.5$ will reach current less than 10% larger than the bulk current. Any approach curve exhibiting contrast larger than this will have an electron rate constant faster than $\Lambda = 0.5$. For $H = 3$ and higher, this will be for $\Lambda = 0.1$. In fact for $H = 5$ and $R_g = 1.1$, the normalised current does not vary by more than 2.5% from the bulk normalised current.

For all tips, rates for which $\Lambda < 0.01$ will be within experimental error of the negative feedback case. These two facts mean that if a user observes a negative feedback current, the rate constant will be between $0.01 < \Lambda < 0.5$ for $H = 1$ and $0.01 < \Lambda < 0.1$ for $H = 3$ and more.

For positive feedback, the range of Λ will be between 0.5 (or 0.1 for high aspect ratios) and 10. For small insulation sheath thicknesses, the range of possible rate constants will be $1 < \Lambda < 10$ if the current increase is more than 20% compared to the bulk current. These guidelines, along with the approach curves in figure 6.6 and equations 6.2 and 6.3, should help users of conical electrodes with conical insulation to get an approximate value for the electron transfer rate constant at the substrate studied, until an equation can be derived.

6.4.3 The influence of the surroundings on the current measurement

We have so far studied the current as function of the geometrical parameters of the electrode tip and electron transfer rate constant at the substrate. When extracting kinetic information from the substrate, the regions of interest will often be finite. As a result, the surrounding matrix will affect the current measurement, as observed in chapter 4 with the approach curves and chapter 5 with the line scans. In both these chapters, the difference was between the slowest and

the fastest electron transfer rate constants. Here, the aim is to investigate the influence of the surrounding matrix on the current, when the electron transfer rate constants do not necessarily differ as much as in previous chapter. Line scans over a line of electron transfer rate Λ, embedded in a matrix for which Λ_{matrix} varies between 0 and 10000, were performed and are shown in figure 6.7.

For $\Lambda_{\text{matrix}} = 10000$, there is very fast electron transfer at the electrode and full positive feedback will be reached over this region. The relative difference when imaging a inert line of width 1 is only 17%. This is easily explained: over the width of the line, the diffusion layer will only be slightly more spread out, which will only slightly affect the current measurement. For the opposite case, a fully conducting line embedded in an insulating matrix, the current will almost double. The tip is much more responsive to conducting regions. However due to the spread of diffusion over the surrounding inert matrix, the line will be sensed from far away and the current increase will be slow, thus making the line width difficult to measure, unlike with a surrounding matrix with fast electron transfer.

These simulations confirm that rate constants above $\Lambda = 100$ will behave as though infinite. Similarly, surfaces for which $\Lambda \leq 0.1$ will behave as though an inert surface. Only for a surrounding matrix with $\Lambda_{\text{matrix}} = 0.5$ might it possible to distinguish a line of rate $\Lambda = 0.1$ from an inert surface.

Generally, the full limiting current for a given rate constant is not reached unless there is little difference between the matrix rate constant and the line rate constant. In this case, such as when imaging a line of width 1 and rate $\Lambda = 10000$ surrounded by a matrix for which $\Lambda_{\text{matrix}} = 10$, the line scan will be well defined over the line. When imaging lines of slower rate constant, the influence on the current will be smaller: for example imaging a line for $\Lambda = 0.5$ for $\Lambda_{\text{matrix}} = 1$ will cause a decrease in current smaller than 5%, which is within experimental error and will thus not be considered distinguishable. The other way round, for $\Lambda = 1$ for $\Lambda_{\text{matrix}} = 0.5$, the relative difference will be above experimental error and would therefore be expected to be detected when scanned horizontally.

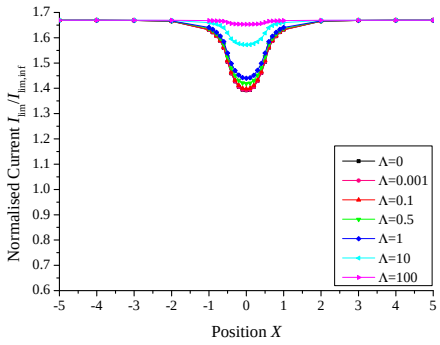

(a) $\Lambda_{\text{matrix}} = 10000$

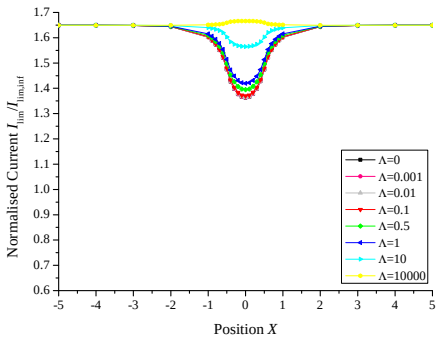

(b) $\Lambda_{\text{matrix}} = 100$

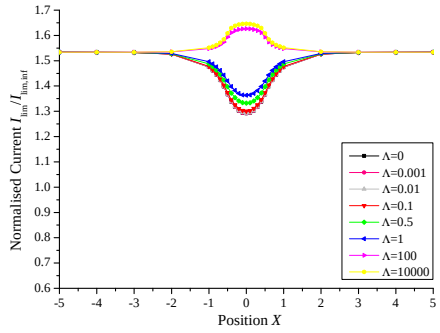

(c) $\Lambda_{\text{matrix}} = 10$

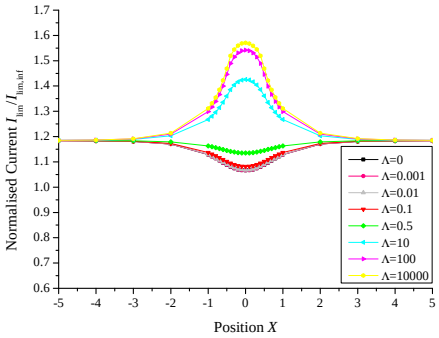

(d) $\Lambda_{\text{matrix}} = 1$

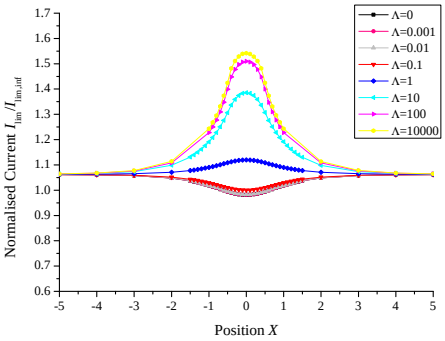

(e) $\Lambda_{\text{matrix}} = 0.5$

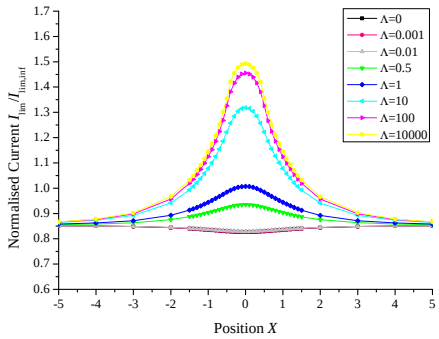

(f) $\Lambda_{\text{matrix}} = 0.1$

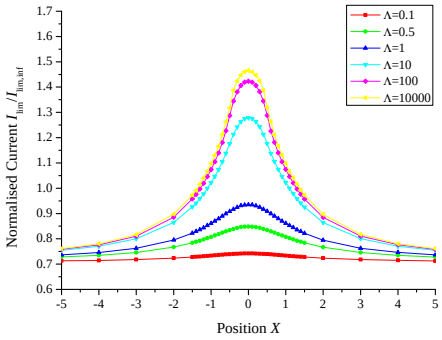

(g) $\Lambda_{\text{matrix}} = 0$

Figure 6.7: Line scans over a line of width 1, of rate constant Λ (specified in the plot legends) embedded in a matrix of rate Λ_{matrix} (given in the sub-plot legend) for a tip with $H = 1.5$ and $R_{\text{g}} = 1.1$ at $L = 0.01$

6.5 Conclusion

Over 150 approach curves were modelled, both for positive and negative feedback, with conical electrodes and conical insulation. Two expressions were fitted to this data, taking as input parameters the insulation sheath radius of the probe, the aspect ratio of the conical electrode and the tip-substrate distance. Next, the electron transfer rate at the substrate was taken into account and for a wide range of geometries, approach curves were once again generated. No equation was successfully fitted to the data, although instructions were derived for users to be able to approximate the rate from the experimental data. However work will continue on fitting the approach curves and it is expected that an expression will be found to fit the current at the tip as a function of H, R_{g}, L and K. Finally, the study of the influence of the surrounding matrix was performed recently for which 3D simulations of line scans were required and difficult boundary conditions were applied. This enabled us to quantify the influence of the environment around a line being scanned and thus determine which rates could be distinguished from others. Further work would also focus on simulating different line widths and then deriving a method to determine the width of the conducting or insulating line from a given line scan.

Study of other SECM problems

Chapter 7

Ring disc electrodes and collection efficiency

The work presented in this chapter was not part of the main aim of the project, which focussed on the conical electrodes, but a side activity. As it is novel and of interest to the SECM community, the work is presented.

7.1 Introduction

Ring-disc microelectrodes were first introduced in 1995 by Zhao et al.[140] These electrodes were fabricated by coating carbon fibres with successive insulating and conducting layers using chemical vapour deposition. Ring-disc electrodes have frequently been used, mainly as rotating ring disc systems.[5;6;141;142] Microdisc ring arrays have recently also used to study the production of nitric acid.[143]

However this electrode geometry also found its uses in scanning electrochemical microscopy. The geometry first appeared in the SECM literature in 2002.[144] The theory of SECM with ring disc electrodes was further studied by Liljeroth *et al.*[145] who looked at the response of both the generating disk and the collecting ring when approaching conducting and insulating substrate. The collection efficiency was studied as a function of the tip-substrate distance using experimental and simulated data, which were in good agreement. The influence of the thickness of the collecting ring, the insulation sheath thickness, the approach speed

and the ratio of the inner ring radius over the outer ring radius on the limiting current and collection efficiency was investigated. SECM probe have been used to study novel cathode electrocatalysts for polymer electrolyte membrane fuel cells. This was done with a disc and as a result, although electrocatalysts with high activity for oxygen reduction are successfully detected, no information about the process occurring can be extracted.[146] Using a ring disc electrode will enable the identification of suitable cathode material using the disc part of the probe, whilst monitoring the production of H_2O_2 at the substrate, by-product of the oxygen reduction reaction.[147]

The aim of the work here was to model in depth the influence of the tip-substrate distance when using a specific dimension ring-disc electrode. The thickness of the ring and the disc, as well as the insulation sheath radius are fixed with the separation between the disc and the ring being the only parameter investigated. The dimensions are provided in the following section. The collection efficiency will be monitored, using equation 7.1. The effect of the distance between the ring and the disc will thus be evaluated.

$$\text{Collection efficiency} = \frac{-I^{\text{ring}}_{\text{lim,inf}}}{I^{\text{disc}}_{\text{lim,inf}}} \tag{7.1}$$

The influence of the ring-disc separation will firstly be evaluated in the bulk. Secondly, SECM experiments will be simulated, assuming a reduction takes place at the disc and an oxidation at the ring. The probe will be approaching either a conducting surface, at which an oxidation takes place, thus making it in competition with the ring, and an inert substrate. The collection efficiency will then be monitored both as a function of the ring-disc separation, the tip-substrate distance and the substrate type.

7.2 Details of the simulation

The ring-disc problem is modelled in 2D axisymmetric geometry, as the symmetry of the ideal probe allows us this simplification. The dimensions of the probe are the disc radius $r_{\text{tip}} = 0.5$ μm, the inner ring radius $r_{\text{InnerRadius}} = 1$ μm to

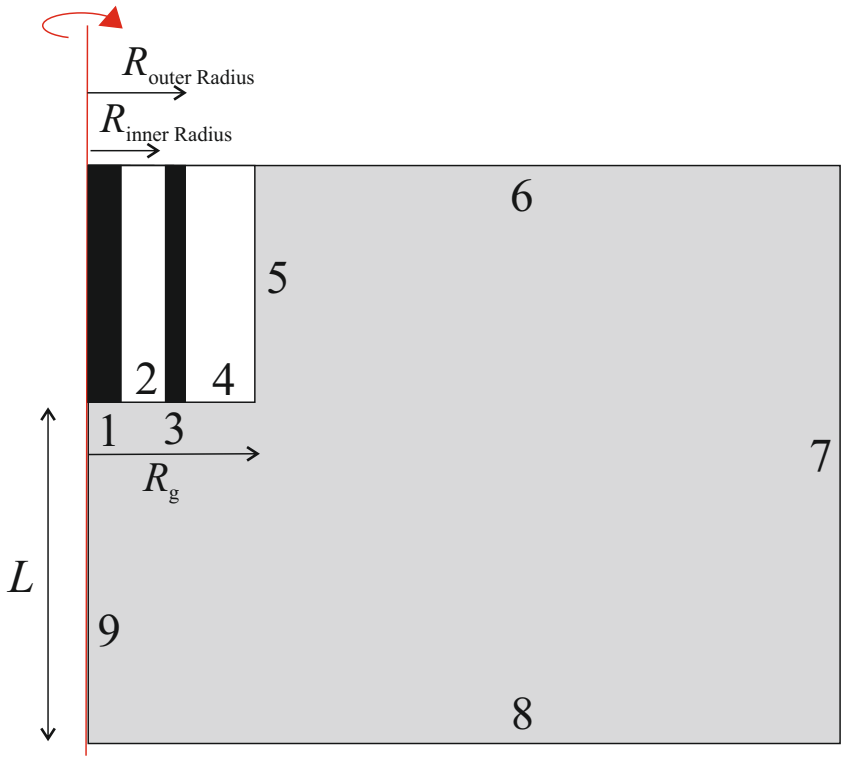

Figure 7.1: Schematic representation of the simulation domain for the SECM ring-disc experiment, in 2D axisymmetric

$r_{\mathrm{InnerRadius}} = 15\ \mu\mathrm{m}$, the outer radius $r_{\mathrm{OuterRadius}} = r_{\mathrm{InnerRadius}} + 1\ \mu\mathrm{m}$ and the insulation sheath thickness $r_{\mathrm{g}} = 30\mu\mathrm{m}$. These parameters are shown in figure 7.1; the distances are normalised by the radius of the disc to give the dimensionless quantities $R_{\mathrm{InnerRadius}}$, $R_{\mathrm{OuterRadius}}$ and R_{g}.

The tip-substrate distance l, also adimensionalised by the radius of the disc electrode r_{tip} to form the dimensionless distance $L = {}^{l}/_{r_{\mathrm{tip}}}$, was varied to create approach curves. The solution consists of a redox mediator couple; a potential is applied to the tip to reduce/oxidise the mediator under diffusion control. The oxidised and reduced forms of the mediator are assumed to have the same diffusion coefficient. As we are dealing with microelectrodes, the system is solved in the steady state. It is once again assumed that there is no convection and no migration. Initially, the solution only contains the oxidant, at uniform concentration c_{b}. As dimensionless units are used, the initial and bulk concentration will be $C_{\mathrm{b}} = 1$. The boundary conditions applied are detailed in table 7.1.

Fick's second law of diffusion was solved for these conditions. The current at the disc and at the ring were computed by integrating the flux over the area of

the disc and ring electrode respectively. Currents were normalised by the current in the bulk.

Table 7.1: Boundary conditions applied to the ring disc model

Boundary number	Boundary description	Boundary condition
1	Disc electrode	C=0
3	Ring electrode	C=1
2,4,5	Insulation sheath	No flux
8	Substrate	C=1 if conducting and no flux if inert
6,7	Bulk boundaries	C=1
9	Axis of symmetry	No flux

7.3 The effect of the the disc-ring separation

It is important when working with ring-disc electrodes to quantify the collection efficiency of the ring, by this is meant: how much of the product of the reaction at the disc electrode will reach and thus react at the ring electrode. The disc generation/ring collection is considered here. An oxidised species will therefore travel from the bulk to the electrode, where it will be reduced. The reduced species will then diffuse away and may then be re-oxidised at the ring. A series of simulations were carried out for a range of ring disc separations with the tip in the bulk of the solution. The collection efficiency is computed using equation 7.1 and this parameter is plotted as a function of the normalised radius in figure 7.2.

As expected, the closer the ring is to the disc, the higher the collection efficiency. In fact for a normalised inner ring radius of 1.1, the collection efficiency is larger than 90%. For more realistic cases, i.e. $r_{\mathrm{InnerRadius}}/r_{\mathrm{tip}}$ ranging from 10 to 30, the efficiency in the bulk is between 60% and 45% for a ring thickness of 1 μm

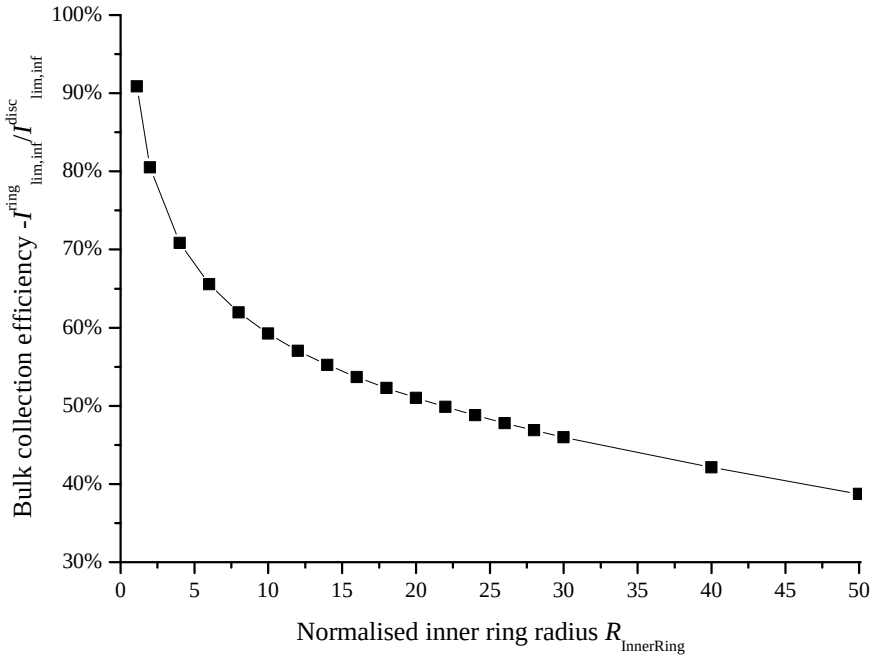

Figure 7.2: Plot of the bulk collection efficiency as a function of the disc-ring separation

7.4 Approach curves with a ring-disc probe

SECM experiments were then modelled, by varying the tip-substrate distance iteratively. In these simulations, the only parameter modified was the radius of the inner ring, varied within the range mentioned in the simulation details. The case where the ring and disc are very close ($r_{\mathrm{InnerRadius}} = 1\ \mu$m) is also presented, for the purpose of comparison. The approach curves for the disc can be seen in figure 7.3(a). These have the characteristic shapes of positive and negative feedback, however, when the ring is very near the disc (red curves) the tip needs to be very close to the substrate before observing positive feedback for a conducting surface or hindered diffusion for an inert surface (within a dimensionless distance of 2).

Approach curves recorded at the ring are shown in figure 7.3(b). When approaching the insulating substrate, the ring current goes through a maximum whose magnitude and position depends on the ring-disc gap. In this case hindrance by the substrate appears to enhance the feedback between the disc and the ring. For small $r_{\mathrm{InnerRadius}}$, the ring will have more influence due to its prox-

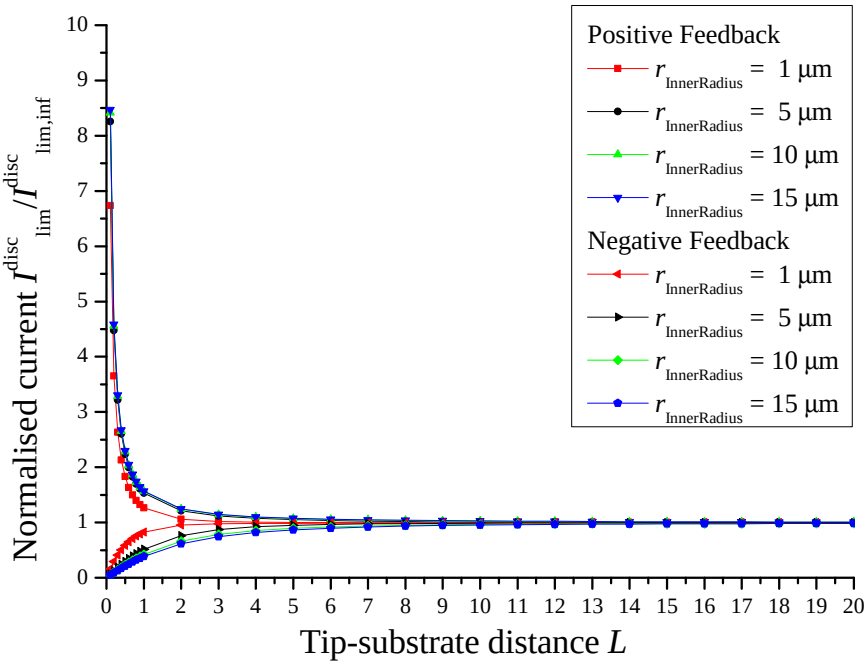

(a) The disc

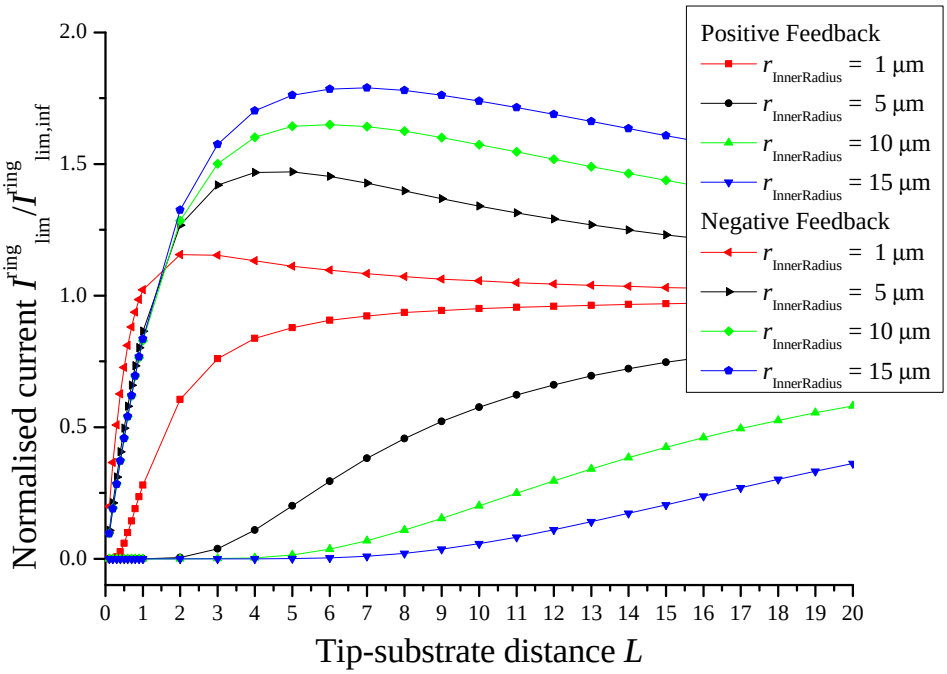

(b) The ring

Figure 7.3: Approach curves for both the disc in (a) and the ring in (b) when approaching a conducting and an inert surface for a range of $r_{\mathrm{InnerRadius}}$ for the parameters

imity hence the dampened increase compared to the case where $r_{\text{InnerRadius}} = 15$ μm. Eventually as the tip-substrate distance gets smaller, hindrance to the disc dominates and the ring current decreases.

When approaching the conducting substrate, there is competition between the substrate and the ring: positive feedback not only occurs between the disc and the substrate but also between the disc and the ring. The ring current decreases from large tip-substrate distances as a result of hindered diffusion to the disc. Interestingly the ring electrode appears to sense hindered diffusion from larger tip-substrate distances than the disc electrode. Furthermore, the larger the ring-disc gap, the sooner the ring current decays.

7.5 The collection efficiency as a function of tip-substrate distance

Figure 7.4(a) shows how the collection efficiency depends on tip-substrate distance when approaching a conducting substrate. It is only large for very small ring-disc gaps. It is null over significant tip-substrate distances for most ring-disc gaps. For the smaller inner ring radius, the collection efficiency remains high until very close to the substrate, due to the regeneration of species at the ring contributing more than the substrate. This is simply due to the very close proximity of the ring. For larger inner ring radii, it is observed that already at a tip-substrate distance of $L = 10$, over half the species reacting at the electrode will regenerate at the substrate. For $r_{\text{InnerRadius}} = 1$ μm, this drops to less than 10%. Finally, for the largest inner radius possible, this is already almost 0%. Eventually, for every inner radius possibility, the collection efficiency is negligible. This reveals how localised the diffusion layer at the microdisc will be.

Figure 7.4(b) shows how the collection efficiency depends on tip-substrate distance when approaching an inert substrate. For all ring-disc gaps, the collection efficiency rises monotonically to reach 100% at small tip-substrate distances. In the bulk, the collection efficiency is higher for an inner ring radius of 1 μm and

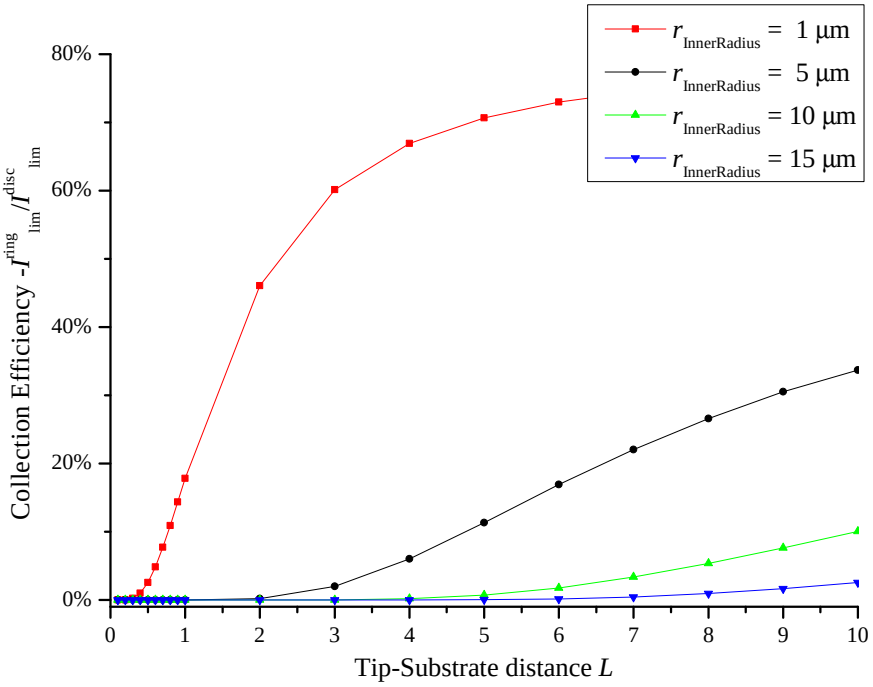

(a) Positive feedback

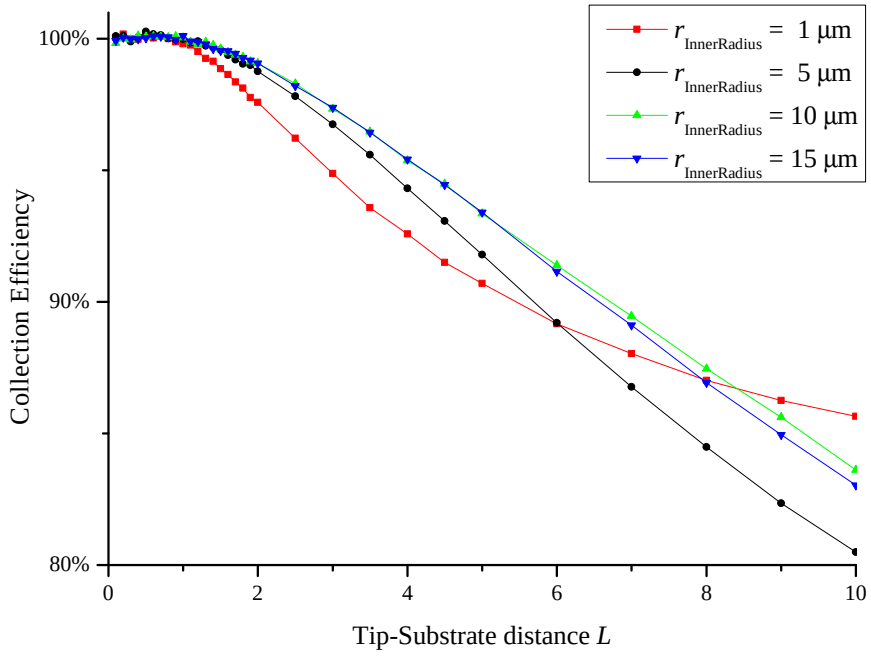

(b) Negative feedback

Figure 7.4: Collection efficiency as a function of the tip-substrate distance, for different insulation sheath thicknesses for both positive and negative feedback in (a) and (b) respectively.

decreases with increasing separation. The proximity of the ring to the disc results in a more localised diffusion layer. As a result, the increase in collection efficiency is slower than for other tips, for which the hindering of diffusion spreads the reduced species towards the ring, ready to be oxidised. Note that the two higher inner ring radii have the same collection efficiency from $L = 5$. The cross over of the collection efficiency curve for r_{Radius} reflects the cross over in the negative feedback approach curves observed in figure 7.3(b).

7.6 Conclusion

The modelling of the ring-disc electrode in the bulk has enabled us to calculate the collection efficiency as function of the normalised inner ring radius. This plot is valid only for $R_{\text{g}} = 30$, although can most likely be applied to most large insulation sheath thicknesses. However a smaller insulation sheath will make a larger difference.

The modelling of SECM experiments then allowed us to look at the influence of the tip-substrate distance on the collection efficiency over both a conducting and an insulating substrate. This study revealed that the collection efficiency decreased with decreasing tip-substrate distance over a conducting substrate. This is due to a competition between the substrate and the ring for the species generated at the tip. Eventually regeneration at the substrate, being much larger and much closer to the electrode, will overtake the ring completely and the collection efficiency drops to 0%. However over the insulating substrate, diffusion is hindered and the ring becomes the major source of reactant for the tip. The collection efficiency reaches 100% within a normalised tip-substrate distance of 2. A collection efficiency of 100% would be advantageous for the study of processes during the screening of electrocatalysts as all the products of the substrate reaction would be detected.

Conclusion

Conclusion

Scanning electrochemical microscopy is a powerful method of gathering information about the reactivity and topography of a surface of interest by scanning a microelectrode over this surface of interest. The combinations of this with atomic force microscopy has been introduced to enable higher accuracy reactivity mapping. This is achieved by scanning the substrate at constant distance, by keeping the force between the tip and the substrate constant, thus minimizing the influence of the topography on the current measurement. The main aim of the project here was to determine the optimum shape of conical electrodes with conical insulation, fabricated for AFM-SECM. The second aim was to study the influence of defects, resulting from the difficult fabrication method, in order to determine whether tips presenting defects could still be used.

In this work, 2D and 3D simulations of SECM experiments with a range of different tips were performed using a commercially available finite element solver, COMSOL Multiphysics. Firstly, the software was validated against well known models which had both been simulated and confirmed experimentally, as well as against models with analytical solutions. Approach curves were also compared to previously reported models. We were then able to confidently run simulations to study electrode geometries. This extremely powerful program has enabled us to investigate a wide range of parameters in detail, relying on thousands of individual simulations.

Chapter 2 presented a meshing procedure for novel users of COMSOL Multiphysics, or another finite element solver, to refer to, in order to simulate their

models to good accuracy.

In chapter 3, the modelling performed focussed on the electrochemical response of the electrodes in the bulk. An expression was derived as no expression previously existed for this geometry; this expression can predict the current at a conical electrode with conical insulation as a function of its geometrical parameters, the aspect ratio H and the insulation sheath thickness R_g and is valid within 1% of the simulated results. This will enables users to calculate the theoretical current at such an electrode, knowing its dimensions, which can also be used to check that the current measured experimentally is correct: there may be leaks or residue from the fabrication method on the electrode surface. Other less serious defects may occur, such as a small insulation angle, an off centred tip or a gap between the insulation sheath and the electrode. It was important to determine what influence these defects would have on the bulk limiting current and therefore eight defects were investigated. Some were shown to have a very big influence on the limiting current such as the crack in insulation. Others, like the presence of side walls, remnant of the etching step, had little effect. Mostly, the defects which had a big influence were the ones that resulted in a large increase or decrease in exposed electroactive area, for e.g. the insulation joining angle defect. As these electrodes were to be found at the end of AFM cantilever, the influence of this cantilever were investigated and shown not to perturb diffusion to the electrode tip.

In chapter 4, a study of the spatial resolution was performed. This was defined as the ability of the electrode to detect a conducting region of a given size, embedded in an insulating matrix, when scanning vertically above the surface of interest. The aspect ratio was shown to be the most important geometrical parameter for the spatial resolution, with larger aspect ratios much less sensitive than small aspect ratio tips. Tips with $H = 1$ will have a current increase larger than 5% when scanning islands twenty times smaller than the electrode radius, whereas with $H = 5$, only an island a fifth of the size of the electrode radius will be picked up by the probe. The larger insulation sheath thickness were shown to

be an advantage here as the diffusion layer would be spread towards the substrate, and thus leading to a larger distortion by the substrate. Spatial resolution also includes knowing how large an island has to be for it to behave as though infinite, for both positive and negative feedback. Zone diagrams were devised for users to refer to, for each aspect ratio and insulation sheath thickness. This revealed that tips with smaller aspect ratios would be less capable of distinguishing larger sized islands from an infinite substrate. The insulation sheath thickness was not found to have a large influence over this factor, although a small difference can be observed when considering the negative feedback case. Once again the influence of defects were investigated. Three were chosen, for which approach curves were generated and compared to the perfect case. Defects which did not affect the bulk current much were shown not to have a larger influence on spatial resolution. Others such as the insulation joining were, as for the current in the bulk, very detrimental to the spatial resolution.

Chapter 5 focussed on the lateral resolution of the probes. This is an index to calculate the theoretical distance necessary for the probe to fully distinguish a conducting region from an insulating region when scanning above the boundary between two regions. This is a useful indicator when comparing two or more cases, but should be used with caution: if the same parameters are not used, such as the points at which the current is sampled, the results could be misleading. A smaller aspect ratio was once again shown to be favourable. This is not a novel finding as previous reports did mention that less protruding electrodes have better resolution. However, this study has enabled us to determine the geometry resulting in the best resolution, with high aspect ratio tips needing almost twice the distance to resolve a conducting region form an insulating region, compared to a low aspect ratio cone. The study into the insulation sheath thickness revealed that the optimum value for R_g was 2. For this thickness, back diffusion is limited but the diffusion layer is not spread out. Scanning the electrode at $L = 0.01$ would improve by more than twice the resolution compared to scanning at a tip radius distance from the electrode. The influence of defects was considered when using line scans and it was revealed that a blunt tip would enhance the resolution

of the AFM-SECM probe, whereas the insulation angle would have no effect. A model substrate was simulated and line scans over conducting and insulating lines were studied. These combined the idea of spatial and lateral resolution and we were able to determine how wide a conducting or insulating line had to be for it to reach the maximum current. The full positive feedback current would be more easily reached for conducting lines: lines as narrow as five times the radius of the electrode would behave as though infinite when the tip was above the line. However at insulating lines, full hindered diffusion current was not easily reached, due to the spread of the diffusion layer.

Chapter 6 focussed on using SECM experiments to extract information firstly about the probe, secondly about the processes of the surface scanned. Expressions for positive and negative feedback approach curves were derived. Using these carefully would allow users to determine the dimensions H and R_{g} of the electrode, which, combined with a steady state limiting current and the expression for the current at a conical electrode in the bulk, would allow for an accurate calculation of the tip radius. Secondly, approach curves and line scans were used to study finite kinetics at the surface. Short of an expression able to calculate the current as a function of tip geometry (H and R_{g}), tip-substrate distance and rate of electron transfer, approach curves were shown for users to compare experimental curves with. Line scans were used to investigate the influence of the electron transfer rate kinetics in the surrounding matrix on the current at line of different finite kinetics. This is useful for users to determine what range of rates can be detected in a larger region of different kinetics.

This thesis therefore presents an extensive study on the electrochemical behaviour of conical tips in a diffusion-only systems. Several new expressions have been produced. The first will enable users to determine the limiting current in the bulk at their electrode. This may reveal defects of different severity. A detailed quantitative analysis of the effect of defects on SECM measurements is then provided. Users can determine how small a region can de detected by their probe. If an SEM micrograph of the tip cannot be obtained, simple approach curves can

be used to determine the dimensions of the cone, using novel expressions derived and presented in this thesis.

Another geometry that was investigated was the ring disc electrode, for applications in scanning electrochemical microscopy. This is the focus of chapter 7. The collection efficiency is monitored both in the bulk and when scanning a simple conducting or insulating surface to determine the influence of the normalised inner ring radius on this parameter and therefore its suitability for screening of electrocatalysts.

Future work on the conical tips would focus on getting a better fit for the expression to extract kinetics. Research into a better method of calculating the lateral resolution would also be continued. Further study would also include research into determining the location of the boundaries of the substrate scanned, using line scans. It would then be interesting to use the conical electrodes to study more specific and applied cases.

References

[1] A. J. Bard, F. R. F. Fan, J. Kwak, and O. Lev. Scanning electrochemical microscopy - introduction and principles. *Analytical Chemistry*, 61(2):132–138, 1989.

[2] J. Kwak and A. J. Bard. Scanning electrochemical microscopy - theory of the feedback mode. *Analytical Chemistry*, 61(11):1221–1227, 1989.

[3] Derek Pletcher. *A First Course in Electrode Processes*. RSC Publishing, Cambridge, 2nd edition edition, 2009.

[4] Allen J. Bard and Larry F. Faulkner. *Electrochemical methods: Fundamentals and Applications*. John Wiley & Sons, Inc., New York, 2nd edition edition, 2001.

[5] F. R. Shu and G. S. Wilson. Rotating-ring-disk enzyme electrode for surface catalysis studies. *Analytical Chemistry*, 48(12):1679–1686, 1976.

[6] R. A. Kamin and G. S. Wilson. Rotating-ring-disk enzyme electrode for biocatalysis kinetic-studies and characterization of the immobilized enzyme layer. *Analytical Chemistry*, 52(8):1198–1205, 1980.

[7] H.A. Laitinen and I.M. Kolthoff. A study of diffusion processes by electrolysis with microelectrodes. *Journal of the American Chemical Society*, 61:1939, 1939.

[8] K. Stulik, C. Amatore, K. Holub, V. Marecek, and W. Kutner. Microelectrodes. definitions, characterization, and applications (technical report). *Pure and Applied Chemistry*, 72(8):1483–1492, 2000.

[9] R. B. Morris, D. J. Franta, and H. S. White. Electrochemistry at pt band electrodes of width approaching molecular dimensions - breakdown of transport-equations at very small electrodes. *Journal of Physical Chem-*

istry, 91(13):3559–3564, 1987.

[10] S. L. Caston and R. L. McCarley. Characteristics of nanoscopic au band electrodes. *Journal of Electroanalytical Chemistry*, 529(2):124–134, 2002.

[11] J. D. Norton, H. S. White, and S. W. Feldberg. Effect of the electrical double-layer on voltammetry at microelectrodes. *Journal of Physical Chemistry*, 94(17):6772–6780, 1990.

[12] S. L. Chen and A. Kucernak. The voltammetric response of nanometer-sized carbon electrodes. *Journal of Physical Chemistry B*, 106(36):9396–9404, 2002.

[13] Allen J. Bard and Michael V. Mirkin. *Scanning Electrochemical Microscopy*. Marcel Dekker, Inc., New York, 2001.

[14] D. Shoup and A. Szabo. Chronoamperometric current at finite disk electrodes. *Journal of Electroanalytical Chemistry*, 140(2):237–245, 1982.

[15] P. J. Mahon and K. B. Oldham. The transient current at the disk electrode under diffusion control: a new determination by the Cope-Tallman method. *Electrochimica Acta*, 49(28):5041–5048, 2004.

[16] P. J. Mahon and K. B. Oldham. Diffusion-controlled chronoamperometry at a disk electrode. *Analytical Chemistry*, 77(18):6100–6101, 2005.

[17] R. C. Engstrom, M. Weber, D. J. Wunder, R. Burgess, and S. Winquist. Measurements within the diffusion layer using a microelectrode probe. *Analytical Chemistry*, 58(4):844–848, 1986.

[18] C. J. Slevin, J. V. Macpherson, and P. R. Unwin. Measurement of local reactivity at liquid/solid, liquid/liquid, and liquid/gas interfaces with the scanning electrochemical microscope: Principles, theory, and applications of the double potential step chronoamperometric mode. *Journal of Physical Chemistry B*, 101(50):10851–10859, 1997.

[19] N. Baltes, L. Thouin, C. Amatore, and J. Heinze. Imaging concentration profiles of redox-active species with nanometric amperometric probes: Effect of natural convection on transport at microdisk electrodes. *Angewandte Chemie-International Edition*, 43(11):1431–1435, 2004.

[20] E. R. Scott, H. S. White, and J. B. Phipps. Iontophoretic transport through porous membranes using scanning electrochemical microscopy - applica-

tion to invitro studies of ion fluxes through skin. *Analytical Chemistry*, 65(11):1537–1545, 1993.

[21] C. M. Sanchez-Sanchez, J. Rodiriguez-Lopez, and A. J. Bard. Scanning electrochemical microscopy. 60. quantitative calibration of the secm substrate generation/tip collection mode and its use for the study of the oxygen reduction mechanism. *Analytical Chemistry*, 80(9):3254–3260, 2008.

[22] R. D. Martin and P. R. Unwin. Scanning electrochemical microscopy - kinetics of chemical reactions following electron-transfer measured with the substrate-generation-tip-collection mode. *Journal of the Chemical Society-Faraday Transactions*, 94(6):753–759, 1998.

[23] R. D. Martin and P. R. Unwin. Theory and experiment for the substrate generation tip collection mode of the scanning electrochemical microscope: Application as an approach for measuring the diffusion coefficient ratio of a redox couple. *Analytical Chemistry*, 70(2):276–284, 1998.

[24] J. L. Fernandez and A. J. Bard. Scanning electrochemical microscopy 50. kinetic study of electrode reactions by the tip generation-substrate collection mode. *Analytical Chemistry*, 76(8):2281–2289, 2004.

[25] O. Sklyar, M. Trauble, C. A. Zhao, and G. Wittstock. Modeling steady-state experiments with a scanning electrochemical microscope involving several independent diffusing species using the boundary element method. *Journal of Physical Chemistry B*, 110(32):15869–15877, 2006.

[26] F. M. Zhou, P. R. Unwin, and A. J. Bard. Scanning electrochemical microscopy .16. study of 2nd-order homogeneous chemical-reactions via the feedback and generation collection modes. *Journal of Physical Chemistry*, 96(12):4917–4924, 1992.

[27] G. J. Lu, J. S. Cooper, and P. J. McGinn. Secm imaging of electrocatalytic activity for oxygen reduction reaction on thin film materials. *Electrochimica Acta*, 52(16):5172–5181, 2007.

[28] O. Sklyar, J. Ufheil, J. Heinze, and G. Wittstock. Application of the boundary element method numerical simulations for characterization of heptode ultramicroelectrodes in secm experiments. *Electrochimica Acta*, 49(1):117–128, 2003.

[29] K. Karnicka, K. Eckhard, D. A. Guschin, L. Stoica, P. J. Kulesza, and W. Schuhmann. Visualisation of the local bio-electrocatalytic activity in biofuel cell cathodes by means of redox competition scanning electrochemical microscopy (rc-secm). *Electrochemistry Communications*, 9(8):1998–2002, 2007.

[30] G. Lindsey, S. Abercrombie, G. Denuault, S. Daniele, and E. De Faveri. Scanning electrochemical microscopy: Approach curves for sphere-cap scanning electrochemical microscopy tips. *Analytical Chemistry*, 79(7):2952–2956, 2007.

[31] Y. Selzer and D. Mandler. Scanning electrochemical microscopy. theory of the feedback mode for hemispherical ultramicroelectrodes: Steady-state and transient behavior. *Analytical Chemistry*, 72(11):2383–2390, 2000.

[32] Y. Lee, S. Amemiya, and A. J. Bard. Scanning electrochemical microscopy. 41. theory and characterization of ring electrodes. *Analytical Chemistry*, 73(10):2261–2267, 2001.

[33] M. V. Mirkin, F. R. F. Fan, and A. J. Bard. Scanning electrochemical microscopy .13. evaluation of the tip shapes of nanometer size microelectrodes. *Journal of Electroanalytical Chemistry*, 328(1-2):47–62, 1992.

[34] A. J. Bard, M. V. Mirkin, and C. G. Zoski. Steady-state currents to conical and spherical segment electrodes. *Abstracts of Papers of the American Chemical Society*, 206:121–ANYL, 1993.

[35] C. G. Zoski. Ultramicroelectrodes: Design, fabrication, and characterization. *Electroanalysis*, 14(15-16):1041–1051, 2002.

[36] C. Lefrou and R. Cornut. Analytical expressions for quantitative scanning electrochemical microscopy (secm). *Chemphyschem*, 11(3):547–556, 2010.

[37] J. L. Amphlett and G. Denuault. Scanning electrochemical microscopy (secm): An investigation of the effects of tip geometry on amperometric tip response. *Journal of Physical Chemistry B*, 102(49):9946–9951, 1998.

[38] R. Cornut and C. Lefrou. A unified new analytical approximation for negative feedback currents with a microdisk secm tip. *Journal of Electroanalytical Chemistry*, 608:59–66, 2007.

[39] R. Cornut and C. Lefrou. New analytical approximations for negative feedback currents with a microdisk secm tip. *Journal of Electroanalytical Chemistry*, 604(2):91–100, 2007.

[40] Q. Fulian, A. C. Fisher, and G. Denuault. Applications of the boundary element method in electrochemistry: Scanning electrochemical microscopy. *Journal of Physical Chemistry B*, 103(21):4387–4392, 1999.

[41] R. Cornut, A. Bhasin, S. Lhenry, M. Etienne, and C. Lefrou. Accurate and simplified consideration of the probe geometrical defaults in scanning electrochemical microscopy: Theoretical and experimental investigations. *Analytical Chemistry*, 83(24):9669–9675, 2011.

[42] R. Cornut, S. Poirier, and Janine Mauzeroll. Forced convection during feedback approach curve measurements in scanning electrochemical microscopy: Maximal displacement velocity with a microdisk. *Analytical chemistry*, 84(8):3531–7, 2012.

[43] K. Aoki, O. Y. Chun, C. Jingyuan, and T. Nishiumi. Diffusion-controlled current at elliptically deformed microelectrodes. *Journal of Solid State Electrochemistry*, 15(11-12):2305–2309, 2011.

[44] P. Sun, F. O. Laforge, and M. V. Mirkin. Scanning electrochemical microscopy in the 21st century. *Physical Chemistry Chemical Physics*, 9(7):802–823, 2007.

[45] K. B. Oldham. A hole can serve as a microelectrode. *Analytical Chemistry*, 64(6):646–651, 1992.

[46] P. N. Bartlett and S. L. Taylor. An accurate microdisc simulation model for recessed microdisc electrodes. *Journal of Electroanalytical Chemistry*, 453(1-2):49–60, 1998.

[47] F. I. M. Thomas, S. A. McCarthy, J. Bower, S. Krothapalli, M. J. Atkinson, and P. Flament. Response characteristics of 2 oxygen sensors for oceanic ctds. *Journal of Atmospheric and Oceanic Technology*, 12(3):687–690, 1995.

[48] V. J. Cunnane, D. J. Schiffrin, and D. E. Williams. Micro-cavity electrode - a new-type of liquid-liquid microelectrode. *Electrochimica Acta*, 40(18):2943–2946, 1995.

[49] O. Sklyar, A. Kueng, C. Kranz, B. Mizaikoff, A. Lugstein, E. Bertagnolli, and G. Wittstock. Numerical simulation of scanning electrochemical microscopy experiments with frame-shaped integrated atomic force microscopy-secm probes using the boundary element method. *Analytical Chemistry*, 77(3):764–771, 2005.

[50] G. Nagy and G. Denuault. Three-dimensional random walk simulation of diffusion controlled electrode processes .2. arrays of growing hemispheres. *Journal of Electroanalytical Chemistry*, 433(1-2):175–180, 1997.

[51] G. Nagy, Y. Sugimoto, and G. Denuault. Three-dimensional random walk simulations of diffusion controlled electrode processes .1. a hemisphere, disc and growing hemisphere. *Journal of Electroanalytical Chemistry*, 433(1-2):167–173, 1997.

[52] C. Kranz, G. Friedbacher, and B. Mizaikoff. Integrating an ultramicroelectrode in an afm cantilever: Combined technology for enhanced information. *Analytical Chemistry*, 73(11):2491–2500, 2001.

[53] A. Lugstein, E. Bertagnolli, C. Kranz, and B. Mizaikoff. Fabrication of a ring nanoelectrode in an afm tip: novel approach towards simultaneous electrochemical and topographical imaging. *Surface and Interface Analysis*, 33(2):146–150, 2002.

[54] P. A. Kottke and A. G. Fedorov. Advective and transient effects in combined AFM/SECM operation. *Journal of Electroanalytical Chemistry*, 583(2):221–231, 2005.

[55] Renaud Cornut, Sophie Griveau, and Christine Lefrou. Accuracy study on fitting procedure of kinetics secm feedback experiments. *Journal of Electroanalytical Chemistry*, 650(1):55–61, 2010.

[56] D. Britz, S. Chandra, J. Strutwolf, and D. K. Y. Wong. Diffusion-limited chronoamperometry at conical-tip microelectrodes. *Electrochimica Acta*, 55(3):1272–1277, 2010.

[57] C. Combellas, A. Fuchs, and F. Kanoufi. Scanning electrochemical microscopy with a band microelectrode: theory and application. *Analytical Chemistry*, 76(13):3612–3618, 2004.

[58] S. Daniele, E. De Faveri, I. Kleps, and A. Angelescu. Voltammetric characterization of micro- and submicrometer-electrode arrays of conical shape for electroanalytical use. *Electroanalysis*, 18(18):1749–1756, 2006.

[59] F. Deiss, C. Combellas, C. Fretigny, N. Sojic, and F. Kanoufi. Lithography by scanning electrochemical microscopy with a multiscaled electrode. *Analytical Chemistry*, 82(12):5169–5175, 2010.

[60] R. M. Souto, Y. Gonalez-Garcia, and S. Gonzalez. In situ monitoring of electroactive species by using the scanning electrochemical microscope. application to the investigation of degradation processes at defective coated metals. *Corrosion Science*, 47(12):3312–3323, 2005.

[61] A. C. Bastos, A. M. Simoes, S. Gonzalez, Y. Gonzalez-Garcia, and R. M. Souto. Application of the scanning electrochemical microscope to the examination of organic coatings on metallic substrates. *Progress in Organic Coatings*, 53(3):177–182, 2005.

[62] B. D. Bath, H. S. White, and E. R. Scott. Visualization and analysis of electroosmotic flow in hairless mouse skin. *Pharmaceutical Research*, 17(4):471–475, 2000.

[63] S. Nugues and G. Denuault. Scanning electrochemical microscopy: Amperometric probing of diffusional ion fluxes through porous membranes and human dentine. *Journal of Electroanalytical Chemistry*, 408(1-2):125–140, 1996.

[64] S. B. Basame and H. S. White. Scanning electrochemical microscopy of metal/metal oxide electrodes. analysis of spatially localized electron-transfer reactions during oxide growth. *Analytical Chemistry*, 71(15):3166–3170, 1999.

[65] S. B. Basame and H. S. White. Scanning electrochemical microscopy: Measurement of the current density at microscopic redox-active sites on titanium. *Journal of Physical Chemistry B*, 102(49):9812–9819, 1998.

[66] Piotr Michal Diakowski and Heinz-Bernhard Kraatz. Detection of single-nucleotide mismatches using scanning electrochemical microscopy. *Chemical Communications*, (10):1189–1191, 2009.

[67] K. Borgwarth, C. Ricken, D. G. Ebling, and J. Heinze. Surface analysis by scanning electrochemical microscopy: Resolution studies and applications to polymer samples. *Fresenius Journal of Analytical Chemistry*, 356(3-4):288–294, 1996.

[68] A. J. Bard, M. V. Mirkin, P. R. Unwin, and D. O. Wipf. Scanning electrochemical microscopy .12. theory and experiment of the feedback mode with finite heterogeneous electron-transfer kinetics and arbitrary substrate size. *Journal of Physical Chemistry*, 96(4):1861–1868, 1992.

[69] M. V. Mirkin, T. C. Richards, and A. J. Bard. Scanning electrochemical microscopy .20. steady-state measurements of the fast heterogeneous kinetics in the ferrocene/acetonitrile system. *Journal of Physical Chemistry*, 97(29):7672–7677, 1993.

[70] M. V. Mirkin, L. O. S. Bulhoes, and A. J. Bard. Determination of the kinetic-parameters for the electroreduction of c-60 by scanning electrochemical microscopy and fast scan cyclic voltammetry. *Journal of the American Chemical Society*, 115(1):201–204, 1993.

[71] Y. Selzer, I. Turyan, and D. Mandler. Studying heterogeneous catalysis by the scanning electrochemical microscope (secm): The reduction of protons by methyl viologen catalyzed by a platinum surface. *Journal of Physical Chemistry B*, 103(9):1509–1517, 1999.

[72] J. F. Zhou, Y. B. Zu, and A. J. Bard. Scanning electrochemical microscopy part 39. the proton/hydrogen mediator system and its application to the study of the electrocatalysis of hydrogen oxidation. *Journal of Electroanalytical Chemistry*, 491(1-2):22–29, 2000.

[73] B. Liu and A. J. Bard. Scanning electrochemical microscopy. 45. study of the kinetics of oxygen reduction on platinum with potential programming of the tip. *Journal of Physical Chemistry B*, 106(49):12801–12806, 2002.

[74] D. Mandler and A. J. Bard. Scanning electrochemical microscopy - the application of the feedback mode for high-resolution copper etching. *Journal of the Electrochemical Society*, 136(10):3143–3144, 1989.

[75] A. J. Bard, G. Denuault, C. Lee, D. Mandler, and D. O. Wipf. Scanning electrochemical microscopy - a new technique for the characterization and

modification of surfaces. *Accounts of Chemical Research*, 23(11):357–363, 1990.

[76] P. I. James, L. F. Garfias-Mesias, P. J. Moyer, and W. H. Smyrl. Scanning electrochemical microscopy with simultaneous independent topography. *Journal of the Electrochemical Society*, 145(4):L64–L66, 1998.

[77] M. Etienne, E. C. Anderson, S. R. Evans, W. Schuhmann, and I. Fritsch. Feedback-independent pt nanoelectrodes for shear force-based constant-distance mode scanning electrochemical microscopy. *Analytical Chemistry*, 78(20):7317–7324, 2006.

[78] Fernando Cortes-Salazar, Markus Traeuble, Fei Li, Jean-Marc Busnel, Anne-Laure Gassner, Mohamad Hojeij, Gunther Wittstock, and Hubert H. Girault. Soft stylus probes for scanning electrochemical microscopy. *Analytical Chemistry*, 81(16):6889–6896, 2009.

[79] G. Binnig, C. F. Quate, and C. Gerber. Atomic force microscope. *Physical Review Letters*, 56(9):930–933, 1986.

[80] G. Binnig and H. Rohrer. Scanning tunneling microscopy. *Surface Science*, 152(APR):17–26, 1985.

[81] G. Binnig, C. Gerber, E. Stoll, T. R. Albrecht, and C. F. Quate. Atomic resolution with atomic force microscope. *Surface Science*, 189:1–6, 1987.

[82] J. V. Macpherson, P. R. Unwin, A. C. Hillier, and A. J. Bard. In-situ imaging of ionic crystal dissolution using an integrated electrochemical/afm probe. *Journal of the American Chemical Society*, 118(27):6445–6452, 1996.

[83] J. V. Macpherson, C. E. Jones, and P. R. Unwin. Simultaneous topographical and amperometric imaging of surfaces in air and under solution. *Localized in-Situ Methods for Investigating Electrochemical Interfaces*, 99(28):147–165, 2000.

[84] M. N. Holder, C. E. Gardner, J. V. Macpherson, and P. R. Unwin. Combined scanning electrochemical-atomic force microscopy (secm-afm): Simulation and experiment for flux-generation at un-insulated metal-coated probes. *Journal of Electroanalytical Chemistry*, 585(1):8–18, 2005.

[85] J. V. Macpherson and P. R. Unwin. Noncontact electrochemical imaging with combined scanning electrochemical atomic force microscopy. *Analytical*

Chemistry, 73(3):550–557, 2001.

[86] J. V. Macpherson, J. P. G. de Mussy, and J. L. Delplancke. High-resolution electrochemical, electrical, and structural characterization of a dimensionally stable ti/tio2/pt electrode. *Journal of the Electrochemical Society*, 149(7):B306–B313, 2002.

[87] C. E. Gardner, P. R. Unwin, and J. V. Macpherson. Correlation of membrane structure and transport activity using combined scanning electrochemical-atomic force microscopy. *Electrochemistry Communications*, 7(6):612–618, 2005.

[88] C. E. Jones, P. R. Unwin, and J. V. Macpherson. In situ observation of the surface processes involved in dissolution from the cleavage surface of calcite in aqueous solution using combined scanning electrochemical-atomic force microscopy (secm-afm). *Chemphyschem*, 4(2):139–146, 2003.

[89] A. Lugstein, E. Bertagnolli, C. Kranz, A. Kueng, and B. Mizaikoff. Integrating micro- and nanoelectrodes into atomic force microscopy cantilevers using focused ion beam techniques. *Applied Physics Letters*, 81(2):349–351, 2002.

[90] A. Kueng, C. Kranz, and B. Mizaikoff. Scanning probe microscopy with integrated biosensors. *Sensor Letters*, 1(1):2–15, 2003.

[91] A. Kueng, C. Kranz, B. Mizaikoff, A. Lugstein, and E. Bertagnolli. Combined scanning electrochemical atomic force microscopy for tapping mode imaging. *Applied Physics Letters*, 82(10):1592–1594, 2003.

[92] C. Kranz, K. Eckhard, H. Shin, B. Mizaikoff, and W. Schuhmann. Alternating current (ac) impedance imaging with combined atomic force scanning electrochemical microscopy (afm-secm). *Electrochemistry Communications*, pages 1311–15, 2007.

[93] J. Abbou, C. Demaille, M. Druet, and J. Moiroux. Fabrication of submicrometer-sized gold electrodes of controlled geometry for scanning electrochemical-atomic force microscopy. *Analytical Chemistry*, 74(24):6355–6363, 2002.

[94] J. Abbou, A. Anne, and C. Demaille. Probing the structure and dynamics of end-grafted flexible polymer chain layers by combined atomic

force-electrochemical microscopy. cyclic voltammetry within nanometer-thick macromolecular poly(ethylene glycol) layers. *Journal of the American Chemical Society*, 126(32):10095–10108, 2004.

[95] Kang Wang, Cedric Goyer, Agnes Anne, and Christophe Demaille. Exploring the motional dynamics of end-grafted dna oligonucleotides by in situ electrochemical atomic force microscopy. *Journal of Physical Chemistry B*, 111(21):6051–6058, 2007.

[96] P. S. Dobson, J. M. R. Weaver, M. N. Holder, P. R. Unwin, and J. V. Macpherson. Characterization of batch-microfabricated scanning electrochemical-atomic force microscopy probes. *Analytical Chemistry*, 77(2):424–434, 2005.

[97] A. Davoodi, A. Farzadi, J. Pan, C. Leygraf, and Y. Zhu. Developing an afm-based secm system; instrumental setup, secm simulation, characterization, and calibration. *Journal of the Electrochemical Society*, 155(8):C474–C485, 2008.

[98] M. R. Gullo, Pltm Frederix, T. Akiyama, A. Engel, N. F. deRooij, and U. Staufer. Characterization of microfabricated probes for combined atomic force and high-resolution scanning electrochemical microscopy. *Analytical Chemistry*, 78(15):5436–5442, 2006.

[99] A. J. Wain, D. Cox, S. Q. Zhou, and A. Turnbull. High-aspect ratio needle probes for combined scanning electrochemical microscopy-atomic force microscopy. *Electrochemistry Communications*, 13(1):78–81, 2011.

[100] K. Eckhard, C. Kranz, H. Shin, B. Mizaikoff, and W. Schuhmann. Frequency dependence of the electrochemical activity contrast in ac-scanning electrochemical microscopy and atomic force microscopy-ac-scanning electrochemical microscopy imaging. *Analytical Chemistry*, 79(14):5435–5438, 2007.

[101] A. Avdic, A. Lugstein, M. Wu, B. Gollas, I. Pobelov, T. Wandlowski, K. Leonhardt, G. Denuault, and E. Bertagnolli. Fabrication of cone-shaped boron doped diamond and gold nanoelectrodes for afm-secm. *Nanotechnology*, 22(14), 2011.

[102] S. W. Feldberg. *Electroanal. Chem. Vol. 3.* Marcel Dekker, Inc., New York, 1969.

[103] T.A. Joslin. *The study and control of diffusion processes in electrochemistry.* PhD thesis, University of Southampton, 1973.

[104] D. Britz. *Digital simulation in electrochemistry.* Springer-Verlag Berlin Heidelberg New York, 1981.

[105] D. Britz. *Digital simulation in electrochemistry.* Springer-Verlag, Darmstadt, second, revised and extended edition edition, 1988.

[106] http://www.basinc.com/products/ec/digisim/.

[107] S. C. B. Abercrombie and G. Denuault. Steady state simulation of electrode processes with a new error bounded adaptive finite element algorithm. *Electrochemistry Communications*, 5(8):647–656, 2003.

[108] O. Sklyar and G. Wittstock. Numerical simulations of complex nonsymmetrical 3d systems for scanning electrochemical microscopy using the boundary element method. *Journal of Physical Chemistry B*, 106(30):7499–7508, 2002.

[109] J. N. Angus. *Numerical simulation of complex microelectrode geometries.* PhD thesis, Univeristy of Southampton, 2002.

[110] E. J. F. Dickinson, I. Streeter, and R. G. Compton. Chronoamperometry and cyclic voltammetry at conical electrodes, microelectrodes, and electrode arrays: Theory. *Journal of Physical Chemistry B*, 112(13):4059–4066, 2008.

[111] G. Wittstock, O. Sklyar, T. H. Treutler, and N. Vlachopoulos. The geometry of nanometer-sized electrodes and its influence on electrolytic currents and metal deposition processes in scanning tunneling and scanning electrochemical microscopy. *Surface Science*, 597(1-3):181–95, 2005.

[112] J. Galceran, S. L. Taylor, and P. N. Bartlett. Steady-state currents at inlaid and recessed microdisc electrodes for first-order EC' reactions. *Journal of Electroanalytical Chemistry*, 476(2):132–147, 1999.

[113] K. Harriman, D. J. Gavaghan, P. Houston, and E. Suli. Adaptive finite element simulation of currents at microelectrodes to a guaranteed accuracy. theory. *Electrochemistry Communications*, 2(3):157–162, 2000.

[114] K. Harriman, D. J. Gavaghan, P. Houston, and E. Suli. Adaptive finite element simulation of currents at microelectrodes to a guaranteed accuracy. an E reaction at a channel microband electrode. *Electrochemistry Communications*, 2(8):567–575, 2000.

[115] K. Harriman, D. J. Gavaghan, P. Houston, and E. Suli. Adaptative finite element simulation of currents at microelectrodes to a guaranteed accuracy. first-order EC' mechanism at inlaid and recessed discs. *Electrochemistry Communications*, 2(3):163–170, 2000.

[116] K. Harriman, D. J. Gavaghan, P. Houston, and E. Suli. Adaptative finite element simulation of currents at microelectrodes to a guaranteed accuracy. application to a simple model problem. *Electrochemistry Communications*, 2(3):150–156, 2000.

[117] K. Harriman, D. J. Gavaghan, P. Houston, D. Kay, and E. Suli. Adaptive finite element simulation of currents at microelectrodes to a guaranteed accuracy. ECEand EC2E mechanisms at channel microband electrodes. *Electrochemistry Communications*, 2(8):576–585, 2000.

[118] J. Galceran, S. L. Taylor, and P. N. Bartlett. Modelling the steady-state current at the inlaid disc microelectrode for homogeneous mediated enzyme catalysed reactions. *Journal of Electroanalytical Chemistry*, 506(2):65–81, 2001.

[119] T. Nann and Y. Heinze. Simulation in electrochemistry using the finite element method part 2: scanning electrochemical microscopy. *Electrochimica Acta*, 48(27):3975–3980, 2003.

[120] C. G. Zoski, B. Liu, and A. J. Bard. Scanning electrochemical microscopy: Theory and characterization of electrodes of finite conical geometry. *Analytical Chemistry*, 76(13):3646–3654, 2004.

[121] C. Lefrou. A unified new analytical-approximation for positive feedback currents with a microdisk secm tip. *Journal of Electroanalytical Chemistry*, 592(1):103–112, 2006.

[122] C. Lefrou. Very easy kinetics determination for feedback curves with a microdisk secm tip and rather rapid substrate reaction. *Journal of Electroanalytical Chemistry*, 601(1-2):94–100, 2007.

[123] C. Lefrou and R. Cornut. New analytical approximations for negative feedback currents with a microdisk secm tip. *Journal of Electroanalytical Chemistry*, pages 91–100, 2007.

[124] R. Cornut and C. Lefrou. New analytical approximation of feedback approach curves with a microdisk secm tip and irreversible kinetic reaction at the substrate. *Journal of Electroanalytical Chemistry*, 621(2):178–184, 2008.

[125] R. Cornut, P. Hapiot, and C. Lefrou. Enzyme-mediator kinetics studies with secm: Numerical results and procedures to determine kinetics constants. *Journal of Electroanalytical Chemistry*, 633(1):221–227, 2009.

[126] http://www.cise.ufl.edu/research/sparse/umfpack/.

[127] I. J. Cutress, E. J. F. Dickinson, and R. G. Compton. Analysis of commercial general engineering finite element software in electrochemical simulations. *Journal of Electroanalytical Chemistry*, 638(1):76–83, 2010.

[128] Stuart Abercrombie. *Numerical Simulation of Diffusion Controlled Reactions*. PhD thesis, 2003.

[129] Y. Saito. Theoretical study on the diffusion current at the stationary electrodes of circular and narrow band types. *Review of Polarography*, 15:177–187, 1968.

[130] L. C. R. Alfred and K. B. Oldham. The steady state at a pair of hemispherical microelectrodes. *Journal of Electroanalytical Chemistry*, 396(1-2):257–263, 1995.

[131] R. M. Penner, M. J. Heben, and N. S. Lewis. Preparation and electrochemical characterization of conical and hemispherical ultramicroelectrodes. *Analytical Chemistry*, 61(15):1630–1636, 1989.

[132] A. V. Sokirko and K. B. Oldham. The voltammetric response of a conical electrode. *Journal of Electroanalytical Chemistry*, 430(1-2):15–24, 1997.

[133] Y. H. Shao, M. V. Mirkin, G. Fish, S. Kokotov, D. Palanker, and A. Lewis. Nanometer-sized electrochemical sensors. *Analytical Chemistry*, 69(8):1627–1634, 1997.

[134] R. D. Martin and P. R. Unwin. Scanning electrochemical microscopy: theory and experiment for the positive feedback mode with unequal diffusion

coefficients of the redox mediator couple. *Journal of Electroanalytical Chemistry*, 439(1):123–136, 1997.

[135] R. Cornut. *Developpement et optimisation de techniques analytiques à l'aide de simulations numeriques, pour le microscope electrochimique*. PhD thesis, Institut polytechnique de Grenoble, 2009.

[136] E. N. Ervin, H. S. White, and L. A. Baker. Alternating current impedance imaging of membrane pores using scanning electrochemical microscopy. *Analytical Chemistry*, 77(17):5564–5569, 2005.

[137] G. Wittstock, H. Emons, T. H. Ridgway, E. A. Blubaugh, and W. R. Heineman. Development and experimental evaluation of a simple system for scanning electrochemical microscopy. *Analytica Chimica Acta*, 298(3):285–302, 1994.

[138] Q. Fulian, A. C. Fisher, and G. Denuault. Applications of the boundary element method in electrochemistry: Scanning electrochemical microscopy, part 2. *Journal of Physical Chemistry B*, 103(21):4393–4398, 1999.

[139] C. Wei, A. J. Bard, G. Nagy, and K. Toth. Scanning electrochemical microscopy. 28. ion-selective neutral carrier-based microelectrode potentiometry. *Analytical Chemistry*, 67(8):1346–1356, 1995.

[140] G. Zhao, D. M. Giolando, and J. R. Kirchhoff. Carbon ring disk ultramicroelectrodes. *Analytical Chemistry*, 67(8):1491–1495, 1995.

[141] K. Hirano and A. J. Bard. Semiconductor electrodes .28. rotating-ring-disk electrode studies of photo-oxidation of acetate and iodide at n-tio2. *Journal of the Electrochemical Society*, 127(5):1056–1059, 1980.

[142] K. L. Hsueh, D. T. Chin, and S. Srinivasan. Electrode-kinetics of oxygen reduction - a theoretical and experimental-analysis of the rotating ring-disc electrode method. *Journal of Electroanalytical Chemistry*, 153(1-2):79–95, 1983.

[143] T. T. K. Loan, A. Girard, L. Griscom, F. Razan, S. Griveau, and F. Bedioui. Micro-ring disc ultramicroelectrodes array for direct detection of no-release from s-nitrosoglutathione. *Electrochemistry Communications*, 13(7):681–684, 2011.

[144] P. Liljeroth, C. Johans, C. J. Slevin, B. M. Quinn, and K. Kontturi. Micro ring-disk electrode probes for scanning electrochemical microscopy. *Electrochemistry Communications*, 4(1):67–71, 2002.

[145] P. Liljeroth, C. Johans, C. J. Slevin, B. M. Quinn, and K. Kontturi. Disk-generation/ring-collection scanning electrochemical microscopy: Theory and application. *Analytical Chemistry*, 74(9):1972–1978, 2002.

[146] D. A. Walsh, J. L. Fernandez, and A. J. Bard. Rapid screening of bimetallic electrocatalysts for oxygen reduction in acidic media by scanning electrochemical microscopy. *Journal of the Electrochemical Society*, 153(6):E99–E103, 2006.

[147] L. Johnson R. Walker D. A. Walsh. Screening of fuel cell electrocatalysts: activity and H_2O_2 detection during O_2 electroreduction. In *ISE 62nd Meeting*, 2011.

Appendix A

The loop

Loop to calculate the diffusion controlled limiting current at an electrode described by the aspect ratio of the cone and the insulation sheath thickness, written in the MATLAB script language

Clear the temporary memory

clear all

Define a vector with the aspect ratio of the conical electrode

Hrange = [1.1 5 10]';

Size of the vector

N = size(Hrange);

Define the insulation sheath thickness

RGrange = [1 3 5]';

Size of the vector

M = size(RGrange);

Define the radius of the electroactive cone (CGSA units)

rtip=1;

Preallocate ouput matrix for speed

AllAppCurve=zeros(N+1, M+1);

NIinf=zeros(M,1);

Loop 1: Varies the aspect ratio iteratively

for i=1:N;

H = Hrange(i)

Calculate the height and radius of the conical probe, function of aspect ratio (Dimensional)

hcone = 500*rtip;

rcone = hcone/H;

Calculate the height of the electrode

htip = H*rtip;

Loop 2: Varies the insulation sheath radius

for j=1:M;

RG = RGrange(j)

Calculate the thickness of the insulation layer

inslayer = (RG*rtip)-rtip;

Normalise the distances by dividing by the radius of the electrode

Rtip= rtip/rtip; Radius of the electrode

Htip=htip/rtip; Height of the electrode

Inslayer=inslayer/rtip; Thickness of the insulation

Rcone= rcone/rtip; Radius of the conical probe

Hcone= hcone/rtip; Height of the conical probe

L = 1000; Tip-substrate distance

Wdomain = 1000; Width of the simulation domain

Hdomain = L + Hcone; Height of the simulation domain

Call the function which creates the model, meshes, solves it and outputs Current, the limiting current at an electrode for the defined H and R_g, taking as input the geometry of the domain.

[Current] = MyPerfectModel(H, Wdomain, Hdomain, L, Rtip, Htip, Inslayer, Rcone, Hcone);

Input data in vector

Create vector for loop 2

RGCurrent(j,1)= RGrange(j);

RGCurrent(j,2)= Current;

Create matrix for loop 1 and 2

AllCurrent(1,1)= H;

AllCurrent(1,i+1)= Hrange(i);

AllCurrent(j+1,1)= RGCurrent(j,1);

AllCurrent(j+1,i+1)= RGCurrent(j,2);

End loop 2

end

End loop 1

end

Write on file

csvwrite('Date-Filename', AllCurrent)

Appendix B

The model function

Begin the function taking as input the geometrical parameters of the model

function[Current] = MyPerfectModel(H, Wdomain, Hdomain, L, Rtip, Htip, Inslayer, Rcone, Hcone)

Clear the model memory

flclear fem

COMSOL version

clear vrsn

vrsn.name = 'COMSOL 3.5';

vrsn.ext = 'a';

vrsn.major = 0;

vrsn.build = 603;

vrsn.rcs = '*Name* **:';**

vrsn.date = '*Date* **: 2008/12/0317 : 02 : 19';**

fem.version = vrsn;

Draw the Geometry

Draw the domain, a rectangle with corner at (0,0)

Domain = rect2(Wdomain, Hdomain, 'pos', [0,0]);

Draw the conical tip

conb = curve2([0 Rtip], [L L+Htip]);

conc = curve2([Rtip Rtip+Inslayer], [L+Htip L+Htip]);

cond = curve2([Rtip+Inslayer Rcone+Inslayer], [L+Htip L+Hcone]);

cone = curve2([Rcone+Inslayer 0], [L+Hcone L+Hcone]);

conf = curve2([0 0], [L+Hcone L]);

ConicalTip = geomcoerce('solid', conb, conc, cond, cone, conf);

Add geometries to create model

ModelGeometry=Domain-ConicalTip;

Set as simulation domain

fem.geom=ModelGeometry;

Definite constants, the dimensionless diffusion coefficient D and the dimensionless initial and bulk concentration c0

fem.const = 'D','1', 'c0','1';

Calculate *elementnumber*, which determines how many elements to constrain along the electrode boundary $PythHyp = sqrt(Rtip^2 + Htip^2) * 100$

$elementnumber = int16(PythHyp)$

Initialize mesh, hnumedge constrains elementnumber elements on boundary 3, hgrad defines the element growth rate, hauto defines elements over the entirety of the domain, which are overridden by the previous commands, however remains the maximum element size, which will be large to ensure that very coarse elements are used in the bulk solution. methodsub is used to specify the mesh generation method as in advancing front or Delaunay

fem.mesh=meshinit(fem, 'hnumedg',[3, elementnumber], 'hgrad', 1.1, 'hauto', 8, 'methodsub','tri');

Plot the mesh

figure, meshplot(fem)

Define the solver

Application mode 1

clear appl Clear the memory

appl.mode.class = 'Diffusion'; Diffusion mode

appl.mode.type = 'axi'; Axisymmetric mode

appl.sdim = 'x','z','y'; Dimensions of the model

appl.module = 'CHEM'; Chemical engineering module

appl.sshape = 2; Geometry shape order, here quadratic shape functions for the global space coordinates

appl.assignsuffix = 'chdi'; Application mode suffix **clear prop** Clear application mode properties

prop.analysis='static'; Define type of analysis, here steady state

appl.prop = prop; Assign properties to application mode

clear bnd Clear boundary conditions

bnd.c0 = 0,0,1,0; Define boundary concentration

bnd.type = 'N0','ax','C','C'; Define boundary type: 'NO' is flux, 'ax' axial symmetry and 'C' concentration

bnd.ind = [2,3,4,1,1,1,3]; Assign a boundary type to each boundary

appl.bnd = bnd; Assign boundary conditions to application mode

clear eq Clear equation memory

equ.D = 'D'; Define diffusion coefficient

equ.init = 'c0'; Define inital condition, here initial concentration in the simulation domain

equ.ind = [1]; Define subdomain groups, here there is just one

appl.equ = equ; Assign equations to application mode

fem.appl1 = appl; Store the application mode in the FEM structure

fem.border = 1; Interior boundary settings

fem.outform = 'general'; Defines form of the application mode, more im-

portant in Multiphsyics

Combine application modes, more important in Muliphysics

fem=multiphysics(fem);

Extend mesh to the desired elements type

fem.xmesh=meshextend(fem);

Solve problem. 'solcomp' determines which variable to solve for and 'outcomp' which variable to output. The property Blocksize determines the number of mesh elements that are assembled together in a vectorized manner. A low value gives a lower memory consumption, while a high value might give a better performance. **fem.sol=femstatic(fem, 'solcomp','c', 'outcomp','c', 'blocksize','auto');**

Integrate the flux over the electrode boundary, i.e. boundary 3

Current=postint(fem,'$2 * pi * x * ndflux_{\mathrm{chdi}}$**', 'unit', '', 'recover','off', 'dl', [3], 'edim',1);**

end